

LASER RANGING AND DATA COMMUNICATION FOR
THE LASER INTERFEROMETER SPACE ANTENNA

Departamento de Teoría de la Señal, Telemática y Comunicaciones
Escuela Técnica Superior de Ingenierías Informática y de Telecomunicación
Universidad de Granada

and

Der Fakultät für Mathematik und Physik der
Gottfried Wilhelm Leibniz Universität Hannover

Presented as a thesis for the degree of Ph.D.

M.Sc. Juan José Esteban Delgado

January 2012

Editor: Editorial de la Universidad de Granada
Autor: Juan José Esteban Delgado
D.L.: GR 1709-2012
ISBN: 978-84-9028-051-5

Prof. Dr Antonio M. Peinado Herreros: Full Professor of Signal Processing and Communications in the dept. of Teoría de la Señal, Telemática y Comunicaciones de la Universidad de Granada (Spain), and advisor of the Ph.D. Thesis of Mr. Juan José Esteban Delgado along with

Prof. Dr. Karsten Danzmann: Full Professor at the University of Hannover and Director of the Max Planck Institute for Gravitational Physics (Albert Einstein Institute) in Hannover (Germany).

INFORM: that **Mr. Juan José Esteban Delgado** has developed the research proposed in this thesis titled 'Laser ranging and data communications for the Laser Interferometer Space Antenna', fulfilling the requirements for the degree of doctor in Telecommunication Engineering.

Advisor: **Prof. Dr Antonio M. Peinado Herreros:**

Granada, a

Signature:

Advisor: **Prof. Dr. Karsten Danzmann:**

Hannover, den

Signature:

M.Sc. Juan José Esteban Delgado

Laser ranging and data communication for the Laser Interferometer Space Antenna

Referent: Prof. Dr. Karsten Danzmann

Referent: Prof. Dr. Antonio M. Peinado Herreros

Dedicado a mi mujer, familia y amigos
en quienes siempre he encontrado apoyo.

— Esteban

ABSTRACT

Interferometric gravitational wave detectors with an unequal and time-varying arm length configuration like the LISA (Laser Interferometer Space Antenna) mission rely on time-delay interferometry (TDI) for laser frequency noise subtraction. However, the TDI algorithm requires an inter-satellite laser ranging scheme with meter accuracy over a five million kilometer arm length. At the end of each arm only about 100 pW of light power will be detected for the gravitational wave measurements and only 1% of this available power can be used for laser ranging in order to avoid degradation in the phase stability of the science measurements. The research work conducted during this doctoral thesis is focused on laser ranging and data communication for LISA. We have experimentally demonstrated a novel on-board laser ranging architecture at 1 pW power levels using a Direct Sequence Spread Spectrum (DS/SS) modulation scheme. This type of modulation also enables optical communication by encoding data with ranging signals and provides significant reduction against spurious interfering signals for bidirectional ranging. Experimental results shown ranging measurements with 42 cm rms noise at 3 Hz of updating rate and the viability of highly reliable data transfer at several kilobits per second.

The proposed laser ranging and data communication scheme is integrated as an auxiliary function of a precise inter-satellite interferometry system. The scientific task for the interferometer is the monitoring of optical pathlength changes at picometer accuracy induced by gravitational waves. In order to provide picometer accuracy at ultra-long distances, the laser metrology system requires the development of two key technologies; firstly, an offset-phase locking method to generate a heterodyne beat signal between the transmitted and received lasers; secondly, a precise phase measurement system to provide interferometric readout at microcycle accuracy of the resulting beat note (in the shortwave frequency band) over time scales of 1000s of seconds. In order to achieve the required phase sensitivity in LISA, the inter-satellite interferometry system implements an optical clock noise transfer scheme. It reduces the effect of the phase noise coupled into the science measurements due to jittering and unsynchronized reference clocks on remote satellites. To this end, each on-board clock is transmitted and accurately measured on the remote satellites. We also investigated the viability of this technique to achieve an equivalent timing stability of $50 \text{ fs}/\sqrt{\text{Hz}}$.

Keywords: LISA, gravitational waves, space interferometry, laser metrology, spread-spectrum modulation, digital control loops, phase measurement systems, clock noise transfer, laser transponders, laser ranging, optical communications.

RESUMEN

Los detectores de ondas gravitacionales interferométricos con longitudes del brazo desiguales y variantes en tiempo como LISA (Laser Interferometer Space Antenna) pueden emplear la técnica de *time-delay interferometry* (TDI) para la substracción del ruido de frecuencia del láser. Sin embargo, este algoritmo requiere la medida de la distancia absoluta *-ranging-* de cada brazo interferométrico con precisión de metros sobre una distancia entre satélites de cinco millones de kilómetros. Al final de cada brazo, sólo 100 pW de potencia óptica es detectada para medir ondas gravitacionales, y tan sólo el 1% de dicha potencia óptica es usada para estimar la distancia entre satélites con el fin de evitar una degradación en la estabilidad de fase de las medidas científicas. La investigación llevada a cabo en esta tesis se centra en la medida de la distancia y en la comunicación de datos entre satélites de LISA. Aquí, presentamos la primera demostración experimental de una novedosa arquitectura basada en una modulación en espectro expandido a un nivel de potencia de 1 pW. Este tipo de modulación también permite la comunicación óptica codificando datos en la señal transmitida y conlleva gran robustez frente a la interferencia espúrea resultante de un esquema de transmisión bidireccional. Los resultados experimentales muestran medidas de la distancia absoluta con un ruido rms de 42 cm a una tasa de refresco de 3 Hz y la viabilidad de una transferencia de datos altamente fiable a varios kilobits por segundo.

El esquema propuesto para la estimación de la distancia absoluta y comunicación de datos se ha integrado como una función auxiliar de un sistema de interferometría entre satélites. El objetivo científico del interferómetro es la monitorización de cambios en el camino óptico con exactitud de picómetros, los cuales están inducidos por ondas gravitacionales. Para obtener exactitud de picómetros sobre distancias de millones de kilómetros, el sistema de metrología láser requiere el desarrollo de dos tecnologías clave. Primero, un lazo de seguimiento en fase para generar la señal de batido heterodina entre el láser transmitido y recibido. Segundo, un sistema de medición en fase para la lectura interferométrica con una exactitud de microciclos a escalas de tiempo de 1000 segundos. Para conseguir la sensibilidad en fase requerida para la misión, el sistema de interferometría entre satélites implementa un esquema de transmisión óptico del ruido entre relojes. Este esquema reduce el efecto del ruido de fase acoplado en las medidas científicas debido al jitter y la desincronización de relojes entre satélites remotos. Para este fin, cada reloj de abordo es transmitido y medido interferométricamente con gran precisión en el satélite remoto. También investigamos en la viabilidad de esta técnica para obtener una estabilidad en tiempo equivalente a $50 \text{ fs}/\sqrt{\text{Hz}}$.

CONTENTS

ABSTRACT	vii
RESUMEN	viii
CONTENTS	ix
LIST OF FIGURES	xii
LIST OF TABLES	xix
ACRONYMS	xix
1 INTRODUCTION	1
1.1 Background and current techniques	1
1.1.1 Space-based laser metrology systems	1
1.2 The way toward LISA: Laser Interferometer Space Antenna	4
1.2.1 LISA Pathfinder	4
1.2.2 GRACE follow-on mission	8
1.3 The LISA mission	10
1.4 Contributions of the thesis	12
1.5 Outline of the thesis	13
I LISA METROLOGY SYSTEM	15
2 LISA INTERFEROMETRY OVERVIEW	17
2.1 LISA electro-optical payload overview	17
2.2 Optical bench interferometry	20
2.3 LISA metrology system	22
3 LISA METROLOGY SYSTEM: SIGNAL MODEL AND NOISE SOURCES OVERVIEW	25
3.1 Opto-electronics front-end	26
3.2 Shot noise limit	28
3.3 Electrical noise budget	29
3.4 Optical noise budget	29
3.4.1 Laser intensity noise	30
3.4.2 Laser frequency noise	35
3.4.3 Beam misalignment	38
3.4.4 Beat note acquisition	40
3.5 ADC noise	41
3.6 Low-depth phase modulations for advanced laser link capabilities	43
3.6.1 High-frequency tone modulation for clock noise transfer	43
3.6.2 Spread spectrum modulation for ranging and data transfer	44
3.7 Doppler shift	47
3.8 Optical measurement of gravitational wave effect	48

3.9	Summary	48
II LASER RANGING AND DATA COMMUNICATIONS 51		
4	RANGING AND DATA COMMUNICATIONS	53
4.1	Statement of the problem: Unequal arm length interferometer	54
4.2	System description overview	55
4.3	Spread spectrum modulation	58
4.4	Code-correlation properties	59
4.5	Signal structure	61
4.6	Receiver architecture	66
4.6.1	Phase measurement system: phase-locked loop	69
4.6.2	Ranging system: delay-locked loop	76
4.6.3	Ranging design parameters	78
4.6.4	Data bit synchronization and bit error corrections	79
4.6.5	Delay loop analysis: linear model	81
4.6.6	Delay measurements readout and estimation of the ranging accuracy	82
4.6.7	Theoretical ranging accuracy limit	84
4.7	FPGA-based custom-designed breadboard	86
4.8	Electrical testing	87
4.8.1	Phasemeter performance with PRN modulation	88
4.8.2	Clock noise performance	90
4.8.3	Time-varying code tracking	91
4.8.4	Ranging accuracy and bit data errors	92
4.9	Summary	94
5	OPTICAL DEMONSTRATION OF LASER RANGING AND DATA TRANSFER	95
5.1	Experimental setup	96
5.1.1	Low-depth phase modulation	98
5.1.2	Weak-light conditions	98
5.2	Optical measurements in weak-light conditions	101
5.2.1	Ranging accuracy: Experimental results	103
5.3	Clock sideband performance with PRN modulation	106
5.4	Future test plan: Bonded hexagonal interferometer	106
5.5	Summary	109
6	ONGOING INVESTIGATIONS AND CONCLUSIONS	111
6.1	Conclusion of the thesis	111
III APPENDIX 115		
A	APPENDIX A	117
A.1	Optical heterodyne detection at low-light power level	117
B	APPENDIX B	121

B.1	Conversion of photocurrent noise into phase noise in the phaseme- ter	121
C	APPENDIX C	125
C.1	Electronics noise and its contributions	125
D	APPENDIX D	129
D.1	Quantification noise	129
E	APPENDIX E	131
E.1	Electronics	131
F	APPENDIX F	137
F.1	FPGA programming using Matlab®	137
F.2	Required software	138
F.3	High-level program description	138
F.3.1	<i>Matlab/Simulink/Synplify DSP</i>	138
F.3.2	<i>Synplify PRO</i>	142
F.4	Low-level program description	142
F.5	Code testing	147
	BIBLIOGRAPHY	149
	ACKNOWLEDGMENTS	159
	CURRICULUM VITÆ	161
	PUBLICATIONS	163
	CONFERENCES	165

LIST OF FIGURES

- Figure 1 (Left side) illustration of the LISA Technology Package (LTP), two test masses are housed in separated vacuum enclosure. The test masses serve as end-mirror of a precise laser interferometer and as inertial references for the satellite drag-free control system. (Right side) photograph of the LTP assembled in the LISA Pathfinder science module structure. Credits in this section provided by ESA. 5
- Figure 2 Inertial sensor system (ISS) unit. From the top left (clockwise). Gold-Platinum test mass, electrode housing, UV lamp unit, front-end electronic, titanium vacuum chamber, caging mechanism. 6
- Figure 3 Flight models of the optical metrology system (OMS). From the top left (clockwise): reference laser unit, laser modulator unit, optical bench interferometer and phase measurement unit. 7
- Figure 4 From left to right, photograph of NASA colloidal thruster flight unit delivered to ESA. European cluster of four Field Emission Electronic Propulsion (FEEP) thruster. Thruster assembled to the LPF science module. 7
- Figure 5 (Left side) Spacecraft structure at IABG test facilities in Munich. (Right side) Propulsion module structure at ESA ESTEC facilities in Netherlands. 8
- Figure 6 Illustration (left side) of the flight formation and photograph (right side) of the two satellites of the Gravity Recovery and Climate Experiment (GRACE) mission. 9
- Figure 7 The LISA constellation's heliocentric orbit. The plane of the near-equilateral triangle formation with a side length of 5×10^6 km is inclined at 60 degrees to the ecliptic, and the constellation trails Earth by about 20 degrees (50×10^6 km distance). 10
- Figure 8 Illustration of the LISA constellation. Three satellites separated by 5 mill km are linked by three bidirectional laser links. Pairs of test-mass from different satellites act as a end-mirror of the interferometer. The interferometry system monitors optical pathlength fluctuations induced by gravitational waves. 11

- Figure 9 Each spacecraft is equipped with two laser systems, two free-floating test masses identical to LISA Pathfinder mission, and two telescope (40 cm-aperture) pointed to the other two satellites at an angle of 60 degrees. Each laser is transmitted to a remote spacecraft with a power of 2 W and detected at the remote photoreceiver at about 100 pW. The laser links are used for monitoring optical pathlength fluctuations between test-masses from different satellites. Besides, the laser links are phase modulated to perform advanced metrology capabilities, including clock noise transfer, absolute laser ranging and data communication. 18
- Figure 10 Artist's impression of a LISA spacecraft (S/C). A support structure holds two optical assemblies with an angle 60°. A mechanism to vary that angle by up to $\pm 1.5^\circ$ with a few nrad/ $\sqrt{\text{Hz}}$ resolution maintains a stable triangle formation compensating orbital dynamics through an optical assembly tracking mechanisms. 19
- Figure 11 Illustration of the LISA optical assembly. The optical telescope receives and transmits the incoming and outgoing beams, respectively. The optical bench is placed orthogonal to the telescope axis. The gravity reference sensor is assembled at the backside of the optical bench. 19
- Figure 12 Breakdown of the split interferometry for a LISA arm. 20
- Figure 13 LISA optical bench reference layout. 21
- Figure 14 Block diagram at the system level of the LISA metrology system (LMS). 22
- Figure 15 Block diagram of the opto-electronics front-end. The signal detector chain is based on optical heterodyne detection with four independent phase readouts for tilt measurements through differential wavefront sensing (DWS). Each segment comprises a transimpedance amplifier (TIA), an anti-aliasing filter (AAF), and a variable gain controller (VGC). The analog signal is digitized by an analog-to-digital converter (ADC), and processed in a field-programmable gate array (FPGA) unit for science measurements. 27
- Figure 16 Left side: Measured relative intensity noise of a non-planar ring oscillator laser. Right side: induced phase noise due to laser intensity fluctuations and shot noise floor reference. 31
- Figure 17 Equivalent displacement noise for the science interferometer readout with a signal light power of 200 pW. 32
- Figure 18 Equivalent displacement noise for the test-mass interferometer readout with a signal light power of 90 μW . 32

- Figure 19 Topology and noise model of the opto-electronic front-end in terms of a single QPD segment. It sketches laser intensity noise, shot noise and electronic noise. The different photocurrent noise contributions are converted to phase noise via $1/\sqrt{C/N_0}$. 33
- Figure 20 Linear model of the control loop for the laser transponder scheme. 36
- Figure 21 Expected laser frequency noise spectra in accordance to statement of work (SOW) of the ESA project: *LISA Metrology System*. 38
- Figure 22 Principle of Differential Wavefront Sensing. Relative wavefront tilts can be inferred from separated phase readouts from different segments. 38
- Figure 23 Heterodyne efficiency and electrical power budget in presence of absolute beam tilt errors. 40
- Figure 24 Relative optical powers versus modulation indices for clock noise transfer. The square of the Bessel function $J_0^2(m_{sb})$ denotes the optical power of the main carrier, $J_1^2(m_{sb})$ denotes the optical power of the first pair of sidebands, and $J_2^2(m_{sb})$ the power in the second pairs of sideband. For small modulation indices $m_{sb} < 1$, the optical power given by $J_2^2(m_{sb})$ can be assumed negligible. The modulation index that corresponds to 10% of the optical power can be computed from the fraction of the total power invested in the first pair of sidebands, which is given by $1 - J_0^2(m_{sb})$. 45
- Figure 25 Modulation index for ranging and related ranging power. 46
- Figure 26 Simplified diagram of the optical metrology system for an interferometric arm in LISA. The metrology system with data communication capability provides measurements of the relative path length displacements between two free-floating test masses, inter-satellite clock jitter and the absolute arm length distance. On each satellite, the on board clock and pseudo-random noise (PRN) sequences encoded with data information are phase modulated onto a laser using an electro-optic modulator (EOM). Both lasers, labeled as master and slave, are exchanged between satellites and offset phase locked to generate the heterodyne beat signals. Each satellite measures the phase of their resulting beat signals in the phase measurement system (PMS), which is also used for PRN demodulation to perform ranging and data transfer. 56
- Figure 27 Auto-correlation (left) and cross-correlation (right) between a family of six different PRN combinations designed for LISA. 60

- Figure 28 Left side: comparison of the auto-correlation function between a Gold pseudo-code used in GPS systems and a pseudo-code used in laser ranging for LISA. Right side: it shows a zoom in the auto-correlation background noise. 61
- Figure 29 (Left side) Auto-correlation function after incoming and outgoing code interference given by the laser transponder configuration. (Right side) Time series of the two code sequences and its resulting interference. 62
- Figure 30 (Left side) Auto-correlation functions under different data rates. The designed code shows a peak of correlation up to 300 kbps. The LISA mission requires lower data rates (≈ 15 kbps). A raw data rate of 24 kbps has been implemented and tested in this thesis. (Right side) illustrates the resulting time series of a data-encoded PRN sequence at 24 kbps. 62
- Figure 31 (Left side) Auto-correlation function in presence of LISA-like shot noise. (Right side) Time series of a PRN code within noise spectral density of $60\mu\text{rad}/\sqrt{\text{Hz}}$ over a photoreceiver bandwidth of 20 MHz. 62
- Figure 32 Expected photoreceiver power spectrum of a low-depth DS/SS modulation scheme with clock tone sidebands. The PRN sequences are encoded with a non-returning zero (NRZ) scheme, where its code power spectrum is maximum at the carrier frequency. 64
- Figure 33 (Left side) Auto-correlation function of a Manchester encoding pulse shape. Manchester encoding doubles the code bandwidth, but ensures a bit transition every code chip. This technique aims to reduce the PRN distortion given by the phase response at the output of the phasemeter architecture. (Right side) Time series after applying Manchester encoding. 65
- Figure 34 Spectrum model for the expected signal at the output of the science photodetector with Manchester encoding for binary streams at $[-1 \ 1]$. The code power spectrum is zero at the carrier frequency. 65
- Figure 35 General architecture and interfaces of the digital control loops implemented for phase readout, ranging and data transfer. 67

- Figure 36 Digital block diagram of the phase-locked loop (PLL) core architecture for a single phasemeter channel. The control loop operates at the sampling frequency (50 MHz). For amplitude, frequency (PIR) and phase readout (PA), a down-sampling scheme based on CIC filters provides: the in-phase (I), the quadrature (Q) and the feedback signals (either PA or PIR) to a computer at Hz rates. 69
- Figure 37 Linear model for the phase-locked loop and description of the main transfer functions. 72
- Figure 38 Open-loop transfer function of the phasemeter feedback control used for ranging and data communication. 73
- Figure 39 Comparison between the modeled and the measured system transfer function of a LISA-like phasemeter. 74
- Figure 40 Error transfer function of the phasemeter feedback control. 75
- Figure 41 (Left side) PRN distortion due to the phasemeter pulse response. This effect can be reduced by encoding the ranging signal with a Manchester scheme. 75
- Figure 42 Expected group delay given by the phasemeter phase response. 76
- Figure 43 General block diagram of the control loop implemented for ranging and data communication. A data-encoded PRN signal coming from the phasemeter is correlated with three versions of the same pseudocode to perform data readout and delay measurements. An on-time version “punctual”, an early (shifted by $+T_c/2$) and a late (shifted by $-T_c/2$). 78
- Figure 44 Design parameters of the ranging system. Code length of 1024 chips running at 1.5 Mbps encoded with a data rate at 24.4 kbps and sampled at 50 MHz. The design parameters enable a ranging system with an ambiguity range of 200 km, a distance resolution of 6 m, and a measurement rate of 1.5 kHz. 79
- Figure 45 Linear model of the delay tracking loop. 81
- Figure 46 Frequency response for the DLL open loop transfer function. 83
- Figure 47 Frequency response diagram for the system transfer function. 83
- Figure 48 Theoretical ranging rms noise for two different shot noise levels. 85
- Figure 49 Photograph of a custom-designed breadboard currently used for performance investigation on phasemeter and ranging architectures. It provides four analog-to-digital (ADC) input channels, two digital-to-analog (DAC) output channels, and space-compatible FPGA processors. 86

- Figure 50 Photograph of a recent digital breadboard that incorporates micro-processor capabilities and enhanced interface communication based on a universal Serial Bus (USB). 88
- Figure 51 Block diagram of the measurement set-up for testing the PRN impact on the phasemeter performance. 89
- Figure 52 (Left side) Electrical spectrum of the phasemeter input signal at different modulation depths. (Right side) Noise power spectral density comparing the impact of different PRN modulation depths in the phasemeter performance. The measurements modulate two PRN sequences (local and remote pseudo-codes) encoded with data streams at 24.4 kbps. 89
- Figure 53 Block diagram of the measurement set-up for testing clock side-band performance. 90
- Figure 54 (Left side) Electrical spectrum of the phasemeter input signal with three different tone signals. (Right side) Noise power spectral density comparing the phasemeter noise performance for both the upper and lower clock tone sidebands. 91
- Figure 55 Delay-locked loop (DLL) tracking capabilities of fast time delay variation with an equivalent inter-satellite velocity of several thousand of meter per second. 92
- Figure 56 Delay-locked loop (DLL) tracking capabilities of slowly varying code delays with equivalent inter-satellite velocities of ± 25 m/s. 92
- Figure 57 (Left side) Electrical spectral of the generated input signal under different Additive white Gaussian noise (AWGN) environments. (Right side) measured ranging accuracies. The ranging errors included AWGN noise, code interference, encoded data and delay variations with equivalent satellite motion at ± 25 m/s. 93
- Figure 58 General schematic of the experimental setup built to test ranging and data communications performance. 97
- Figure 59 Spectrum comparison between the modeled signal spectrum at the output of the photoreceiver and the measured spectrum in weak-light conditions. 101
- Figure 60 Measured noise contribution of the spectrum analyzer, photoreceiver and laser intensity noise in the relevant beat note frequency (MHz) range. The linear spectral density of the laser intensity noise without Noise Eater pre-stabilization activated is shown for comparison, since throughout the realization of this experiment the Noise Eater was activated. 102
- Figure 61 Left side: normalized auto-correlation function measured for different delay resolutions in the code-acquisition mode. Right side: it shows a zoom around the acquisition peak. 102

- Figure 62 Auto-correlation peak amplitude for different acquisition times. 103
- Figure 63 Normalized discriminator function measured for different delay resolution in code tracking mode. 104
- Figure 64 Measured ranging rms noise for different data rates and in the presence of LISA-like noise sources, including interference with a second PRN and signal dynamics with an equivalent interspacecraft larger than the expected 20 m/s. 105
- Figure 65 Top: Setup for measuring the phase fidelity of a single EOM sideband. Center: Sideband picture of the beatnotes as detected by the photodiode. Bottom: Measured phase noise of one single sideband for the EOM under test. 107
- Figure 66 Left side: design of a hexagonal interferometer for optical testing in the mHz band of phasemeter performance, and TDI method using ranging and clock sidebands. Right side: photograph of current design bonded on a Zerodur baseplate. 108
- Figure 67 Heterodyne receiver of two interfering laser beams with slightly different wavefronts angles. 118
- Figure 68 Schematics of the photocurrent noise model for a single segment in a quadrant photodetector. 123
- Figure 69 Noise model of the photoreceiver. 126
- Figure 70 Estimated input current noise for a typical LISA-like photoreceiver using an LMH6624 op-amp in a standard circuit. 126
- Figure 71 Photodetector circuit. 132
- Figure 72 Circuit to drive the PRN modulation. 133
- Figure 73 Analog offset phaselock part 1. 134
- Figure 74 Analog offset phaselock part 2. 135
- Figure 75 Flow diagram for programming the digital breadboard. 139
- Figure 76 Simulink model with a sampling rate of 1 MHz. It simulates a low-pass FIR filter of 51 coefficient, cutoff frequency at 50 kHz, filter roll-off at 80 dB and a sinusoidal input composed for two sines at different frequencies (25 kHz and 475 kHz). 141
- Figure 77 Parameters for the designed filter with minimum order and equiripple method. The magnitude response is normalized at $1 = f_s/2 = 500 \text{ kHz}$ 141
- Figure 78 Synplify DSP converter from Simulink model to RTL code. 142
- Figure 79 Transfer function of the filter designed. 146

LIST OF TABLES

Table 1	Noise contributions in the opto-electronics front end for shot noise (sn), electronic noise (en) and relative intensity noise (RIN). For comparison, four cases were considered; a single-element photodiode (SE), a single segment (Seg), the averaging of N segments of a QPD (NSeg), and the case of hot redundancy, the averaging of two times N segments (2NSeg). 34
Table 2	Optical and electrical power budget per segment for the metrology breadboard. Optical powers according to the ESA project: <i>Optical bench development for LISA</i> . 39
Table 3	Design parameters taken into account in this analysis 66
Table 4	Ranging accuracies and bit error rates for different AWGN noise levels. 93
Table 5	Ranging accuracies for different data rates and different optical power conditions. 105

ACRONYMS

AAF	: Anti-Aliasing Filter
ADC	: Analog-to-Digital Converter
AEI	: Albert Einstein Institute in Hannover
AGC	: Automatic Gain Control
BER	: Bit Error Rate
BPSK	: Binary Phase Shift Keying
CIC	: Cascaded Integrator Comb (filter)
C/N	: Carrier-to-Noise density ratio
DAC	: Digital-to-Analog Converter
DFACS	: Drag-Free and Attitude Control System

DLL : Delay-Locked Loop
PLL : Phase-Locked Loop
DSP : Digital Signal Processor
DSN : Deep Space Network
DSS : Digital Signal Simulator
DTU : Technical University of Denmark
DWS : Differential Wavefront Sensing
EGSE : Electrical Ground Support Equipment
EOM : Electro-Optical Modulator
ESA : European Space Agency
FFT : Fast Fourier Transform
FIR : Finite Impulse Response (filter)
FPGA : Field Programmable Gate Array
FPU : Floating Point Unit
GW : Gravitational Wave
HW : Hardware
LED : Light Emitting Diode
LFSR : Linear Feedback Shift Register
LISA : Laser Interferometer Space Antenna
LMS : LISA Metrology System
LO : Local Oscillator
LPF : Low-pass filter
LPSD : Linear Power Spectral Density
LSB : Lower Sideband / Least Significant Bit
LUT : Look-Up Table
NCO : Numerically Controlled Oscillator

OB : Optical Bench

OpAmp : Operational Amplifier

PA : Phase Accumulator

PAAM : Point-Ahead Actuator Mechanism

PD : Photodiode

PI : Proportional-Integral (controller)

PIR : Phase Increment Register

PMS : Phase Measurement System

PND : Power-to-Noise Density

PRN : Pseudo-Random Noise

QPD : Quadrant Photodiode

rms : Root Mean Square

RF : Radio-frequency

S/C : Spacecraft

SNR : Signal-to-Noise Ratio

SW : Software

TBD : To Be Determined

TDI : Time Delay Interferometry

USB : Upper Sideband / Universal Serial Bus

USO : Ultra Stable Oscillator

XOR : Exclusive-or logic function

INTRODUCTION

The invention of the laser in the 1960's set a milestone for the advance in broad fields of science [1] such as astrophysics, chemistry, and medicine. Nowadays, lasers are being used as measurement tool due to their highly stable wavelengths, being the basis of the development of precision metrology [2, 3]. In the most ambitious metrology developments, such as gravitational wave detectors [4, 5, 6, 7], continuous-wave (c.w) interferometers are capable of measuring a change in length between the two interferometer arms to a precision of one part in $\approx 10^{22}$, corresponding to relative range changes of a few picometers. On the other hand, lasers are providing unprecedented advances in the field of telecommunications. In a similar way to standard radio-frequency (RF) communications, optical links can be modulated. This allows the development of optical-based metrology systems with auxiliary link capabilities such as data transmission. In this thesis, we demonstrate the combination of interferometric approaches as used in gravitational wave detectors, where its ambiguity range is typically limited by the laser wavelength ($\approx 1\mu\text{m}$), with the advantages of optical modulation techniques in order to include absolute distance measurements -ranging- and data transfer. The proposed scheme, a ranging system based on a spread-spectrum modulation as used in Global Positioning Systems (GPS), is unavailable in existing gravitational waves detectors. It overcomes a limiting factor in the design of c.w laser interferometers, the ambiguity range, making possible both picometer-level interferometry and the determination of absolute distances in a single metrology system.

1.1 BACKGROUND AND CURRENT TECHNIQUES

1.1.1 *Space-based laser metrology systems*

As the demand for precise metrology systems and high-bandwidth communication grows, optical systems are becoming the most cost effective alternative compared to RF systems, being an attractive technology for future use in industry and in particular for high demanding space-based applications. In contrast to radio links, a laser link focuses its power into a very narrow beam. It allows the propagation of the laser over large distances with a much lower spreading of the beam. Its high-power concentration also enables the use of lower power sources while increasing data transmission rates, being more secure against beam interception. In addition, optical systems fulfill important requirements for almost all space-borne applications, such as reduction in the power consumption and lower power dissipation. Moreover, optical systems reduce

complexity and weight in flight hardware integration, since the antenna gain is higher than that of radio waves due to the shorter wavelengths of lasers.

The European Space Agency (ESA), the National Aeronautics and Space Administration (NASA) and other space agencies have embarked on ambitious projects to take advantage of those laser links. One of the most prominent projects that have shown the viability of ultra-long optical links in space is the lunar laser ranging (LLR) experiment [8]. Between 1969-1973 five retroreflector ¹ arrays were placed on different locations of the lunar surface, three by Apollo missions and two by the Soviet Luna missions. Nowadays, most of the current lunar data comes from the retroreflector array placed by Apollo 15 astronauts. It provides the highest response and consists of 300 fused silica cubes, each of 3.8 cm sidelength. From the first lunar range measurements with an accuracy of about 20 cm, to the latest data with millimeter-level range accuracy ², LLR has contributed to a wide range of astrophysics experiments for a much better understanding of our solar system. In the field of relativistic gravity [9, 10], LLR measurements provided the most precise experimental tests of the equivalence principle and Newton's gravitational constant. In the field of solar system orbital dynamics, LLR has provided insight into the planetary perturbation of the lunar center of mass as well as providing strong evidence for the internal liquid core of the Moon. Next generation ranging systems are expected to achieve sub-millimeter accuracy to the Moon and will help to progress on the exploration of Mars and beyond.

Similar to LLR, satellite laser ranging (SLR) employs high-power pulsed lasers to measure the round trip travel time from ground stations to retroreflectors placed on artificial satellites. Thus, optical systems are being used for precise navigation of interplanetary spacecraft and exact determination of satellite orbits. To this end, onground ranging stations are located around the world and are actively working together in a global effort under the framework of the International Laser Ranging Service (ILRS). The ILRS is a network of observation stations that also support programs in geodetic, geophysical, and planetary research activities. Advanced SLR stations like NASA SLR2000 are capable of conducting laser ranging to planetary mission spacecraft, e.g., the Lunar Reconnaissance Orbiter (LRO). LRO is the first mission of the Robotic Lunar Exploration Program (RLEP) and relies on ground-satellite range measurements down to 10 cm at 1 Hz. For this mission, one-way laser ranging is used for the determination of a more accurate orbit than it is possible with RF links.

¹ Retroreflectors are passive devices that reflect the light back to its source.

² Approximately 1 mm (Apache Point Observatory Lunar Laser-ranging Operation, APOLLO operative since 2005).

Laser ranging to retroreflectors is mainly limited by the size of the retroreflectors, and its size is usually determined by a compromise between the number of collected photons and the range resolution capability of the system. However, significant advances in ultra-long distance ranging are given by the use of optical transponders. A transponder is an active device that receives an incoming laser beam and transmits a second beam with similar characteristics. They are currently being developed for satellite laser ranging due to the important link advantages over retroreflectors. Based on the unidirectional single-beam propagation, laser transponders only have $1/r^2$ signal loss compared to $1/r^4$ for passive ranging (transmission and reflection). Therefore, this reduces the required optical power for transmission and enables measurements over larger distances. Laser transponders have been successfully tested in space-based applications. Two recent examples are the Mercury Laser Altimeter (MLA) instrument on-board the Messenger spacecraft and the Mars Orbiter Laser Altimeter (MOLA) on-board the Mars Global Surveyor (MGS) spacecraft. The MLA instrument has demonstrated the viability of the retrieval of the clock offset, range and laser communication over 24 million km [11], while the MOLA experiments have set a distance record for a successful laser link over 80 million km.

Moreover, a laser transponder has the additional benefit of dual operability as a transmitter and a receiver for data communications. In this way, an inter-satellite laser link between TerraSAR-X and NFire has recently demonstrated the use of optical communications for broadband link applications [12]. Based on a homodyne detection scheme [13], the successful link covered more than 5×10^3 km at a data rate of 5.6 Gbps with a Binary Phase-Shift Keying (BPSK) modulation scheme.

In the field of optical metrology systems, laser interferometry is a robust space-borne technology. In contrast to pulsed ranging systems, laser interferometers employ continuous wave (c.w.) light sources to monitor changes in the target position at sub-nanometer accuracy. A c.w. interferometer is able to provide shot noise limited performance even when the received beam is sensed at ultra-low light power, being a promising technology for measuring relative displacements of a received optical signal. To this end, laser interferometers monitor relative pathlength fluctuations of light beams through phase measurements of the interfering signals. An interferometer typically combines a number of beams that travel different optical paths to determine factors as lengths, surface irregularities or index of refraction in materials. Thus, the ultra-high sensitivity achieved by these systems are providing unprecedented advances in many different fields of applications including astrophysics and Earth observation. Increasing efforts towards the use of optical interferometry in space-based applications have been undertaken in the past few years. Laser interferometers with sub-wavelength resolution are being developed for the SIM Lite Astrometric Observatory for searching Earth-like planets. Inter-satellite interferometers have been proposed for GRACE follow-on missions in

order to map more accurately the Earth's gravity field and are being developed for the future space-based gravitational wave observatory LISA (Laser Interferometer Space Antenna). Thus, laser interferometry is expected to be used with increased precision over previous missions. The first laser interferometer in space at picometer accuracy will fly on-board LISA Pathfinder, the LISA precursor mission.

1.2 THE WAY TOWARD LISA: LASER INTERFEROMETER SPACE ANTENNA

1.2.1 *LISA Pathfinder*

The LISA Pathfinder (LPF) is a proof of concept for key technologies of a major mission, the space-borne gravitational wave detector LISA. LPF was proposed to ESA in 1998 in order to verify the first in-flight test of gravitational-wave detection technology. The mission was finally approved as part of the Cosmic Vision Scientific Programme in May 2002. LPF has a nominal satellite lifetime in science operation of 180 days, and currently, it is scheduled for launch in 2013 on-board a VEGA vehicle. Its main technological challenge is to maintain two enclosed test-masses (TM) in a nearly perfect gravitational free-fall. To this end, the TM motion is continuously monitored and controlled with unprecedented accuracy by using three main technologies: a highly-stable drag-free attitude control, picometer interferometry and micro-newton thrusters. However, LPF will not only verify these novel technologies, it will also provide unprecedented general relativity tests through, e.g., experimental data of the gravity forces that involves a nearly ideal free-floating mass falling under a geodesic motion in space-time.

The LPF satellite will carry two payloads; the European LISA Technology Package (LTP), and the NASA provided Disturbance Reduction System (DRS), as part of NASA's New Millennium Program. The DRS consists of a set of eight colloidal micro-thrusters and an on-board computer with an alternative software for drag-free control. The LTP (photographs in figure 1) forms the instrument payload, and requires the verification of:

- Gravitational free-fall motion of a TM with a residual acceleration noise less than $3 \times 10^{-14} \text{ ms}^{-2}/\sqrt{\text{Hz}}$, relaxing at frequencies below 3 mHz.
- High-precision laser interferometry using free-floating mirrors (LTP test-mass) with a displacement noise requirement in the sensitive axis of $6.3 \text{ pm}/\sqrt{\text{Hz}}$ between 3-30 mHz, as well as TM angle measurements with a resolution better than $20 \text{ nrad}/\sqrt{\text{Hz}}$.
- Satellite position correction for drag-free orbital flight via micro-thruster, thus shielding the TM from external disturbances to keep it in gravitational free-fall.
- Assess performance, reliability and lifetime of micro-thrusters, laser and optics under space environments.

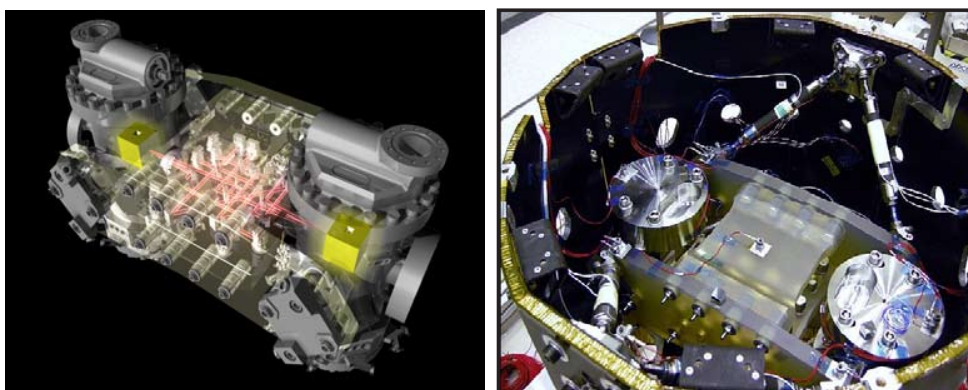


Figure 1: (Left side) illustration of the LISA Technology Package (LTP), two test masses are housed in separated vacuum enclosure. The test masses serve as end-mirror of a precise laser interferometer and as inertial references for the satellite drag-free control system. (Right side) photograph of the LTP assembled in the LISA Pathfinder science module structure. Credits in this section provided by ESA.

The key elements of the LTP payload comprise two main systems; the Inertial Sensor System (ISS) and the Optical Metrology System (OMS). The ISS forms the gravitational reference sensor (figure 2), and basically consists of:

- Two test masses, 46 mm gold-platinum alloy cubes with low magnetic susceptibility, that serve both as end-mirrors of the laser interferometer and as inertial references for the satellite drag-free attitude control.
- The electrode housing to allow capacitive sensing on all axes and electronic actuation of the test mass motion.
- A caging mechanism to hold the test mass during launch as well as smoothly release the mass when on orbit.
- A non-magnetic titanium vacuum enclosure to shield the test-masses from electromagnetic signals and external disturbances.
- The charge management system. Each TM carries a non-contact ultraviolet (UV) discharge system that consists of six Mercury vapor lamps, a set of ultra-low noise capacitive sensing, and actuation electronics to discharge optical fibers and the TM, e.g., from cosmic rays.

The OMS (figure 3) performs TM optical sensing using heterodyne laser interferometry, and comprises four main units:

- A reference laser unit based on a Nd:YAG non-planar ring oscillator (NPRO) laser with an emitting light power of 35 mW. This type of lasers operate at the

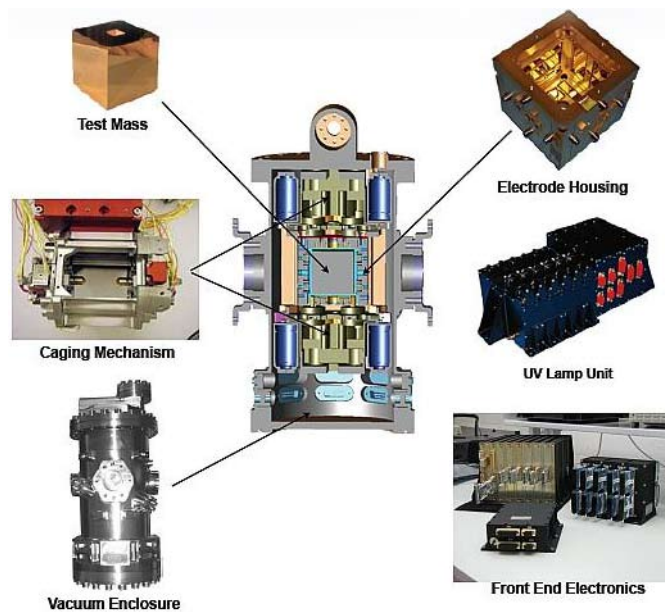


Figure 2: Inertial sensor system (ISS) unit. From the top left (clockwise). Gold-Platinum test mass, electrode housing, UV lamp unit, front-end electronic, titanium vacuum chamber, caging mechanism.

wavelength of 1064 nm and are widely used in precise metrology systems due to their high stability and reliability. The laser was delivered by Tesat. Similar units are flying in satellites like NFire and TerraSAR.

- A laser modulator unit containing two acoustic-optical modulators to generate a frequency offset between two laser beams, thus providing the heterodyne signal at the photodiode output at the designed frequency difference of 1-2 kHz.
- The optical bench (OB) developed by the Albert Einstein Institute (AEI) and the University of Glasgow performs optical readout of the TM longitudinal and angular motion using a heterodyne Mach-Zehnder interferometry concept. The OB was built using a novel technique based on hydroxide catalysis bonding. It is a patented method from the University of Stanford also used for GAIA and Gravity Probe-B due to its mechanical and thermal stability.
- Phase measurement unit (PMU) developed by AEI and delivered by the University of Birmingham mainly processes the phase of the heterodyne signal and additionally provides housekeeping data for monitoring of key parameters such as temperature.

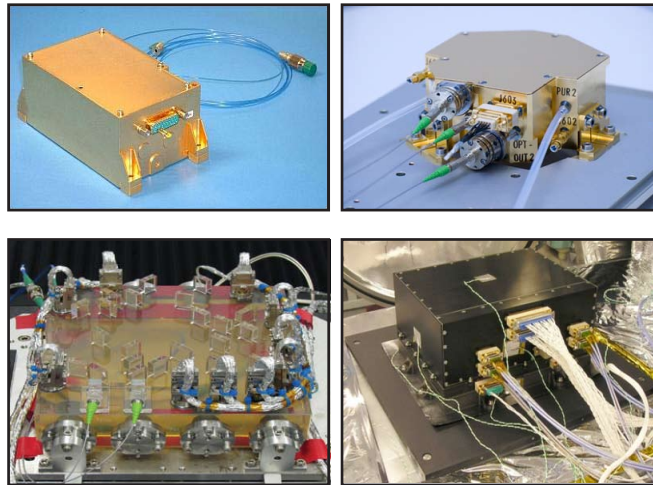


Figure 3: Flight models of the optical metrology system (OMS). From the top left (clock-wise): reference laser unit, laser modulator unit, optical bench interferometer and phase measurement unit.

Through a drag-free attitude control system, the interferometric readouts provide the required information for the stabilization of the different degrees of freedom of the satellite and the test-masses. This way, a drag-free control loop operates both the electrode housing around the test-masses for capacitive actuation/sensing and a set of micro-newton thrusters for precise satellite positioning control. Thus, another of the technical challenges for LPF was the development of micro-Newton thrusters, delivering a propulsion force between $5 \mu\text{N}$ and $30 \mu\text{N}$ with very low acceleration noise. They precisely control the entire spacecraft position around the free-floating test-masses, thus creating a drag-free orbit. LPF will test two thruster architectures: Field emission electronic propulsion (FEEP) thruster (being manufactured in Europe) and Colloidal Micro-Newton thruster being delivered by NASA as part of the DRS (see photographs in figure 4).

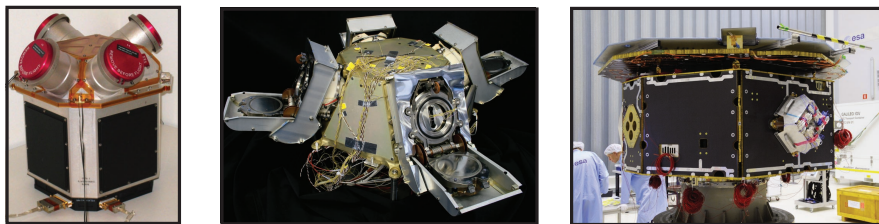


Figure 4: From left to right, photograph of NASA colloidal thruster flight unit delivered to ESA. European cluster of four Field Emission Electronic Propulsion (FEEP) thruster. Thruster assembled to the LPF science module.



Figure 5: (Left side) Spacecraft structure at IABG test facilities in Munich. (Right side) Propulsion module structure at ESA ESTEC facilities in Netherlands.

Procurement and manufacture of the LTP payload involves ESA and a consortium of different European's space agencies with special focus on Germany, Italy, France, Spain, United Kingdom, Netherlands and Switzerland as well as industry partners such as Thales Alenia Space, EADS Astrium, Tesat, Kaiser Threde GmbH and CGS.

Whereas the LISA Pathfinder's optical metrology system resembles a LISA arm in a single satellite, the first inter-satellite interferometry system will fly on-board the GRACE follow-on mission for a precise mapping of the Earth's gravity field. Thus, these two missions will provide the first experimental on-orbit demonstration of essential technologies needed for LISA.

1.2.2 *GRACE follow-on mission*

The Gravity Recovery and Climate Experiment (GRACE) was launched in March 17th, 2002 as a joint venture between NASA and the Deutsches Zentrum für Luft und Raumfahrt (DLR) for mapping time variable gravity field anomalies [14]. GRACE consists of two identical satellites separated about 220 km in near-polar orbits with an altitude up to 500 kilometers (see figure 6). In order to determine the exact spacecraft altitudes and distances at micrometer accuracy as required for gravity data recovery, the satellite motion is continually monitored through several scientific instruments: a microwave K-band ranging system, a satellite laser ranging (SLR) retroreflector, a Global Positioning System (GPS) receiver, a star tracker and an accelerometer.

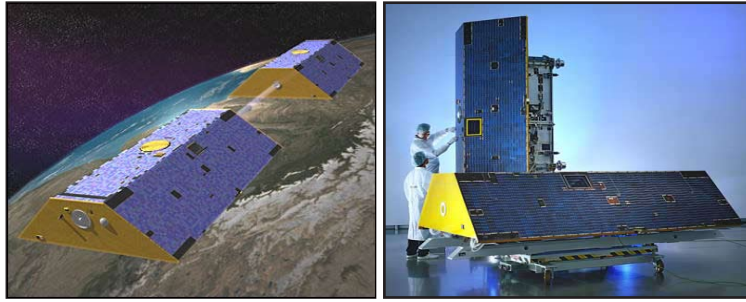


Figure 6: Illustration (left side) of the flight formation and photograph (right side) of the two satellites of the Gravity Recovery and Climate Experiment (GRACE) mission.

The GPS sensors provide geo-location and precise timing, transmitting information about the spacecraft position to a few centimeters. The use of GPS sensor on-board avoids signal propagation through the Earth's lower atmosphere so that it achieves better accuracy than the meter level provided from ground stations. For micrometer range determination, SLR measurements provide a coarse estimation, being then improved by the inter-satellite microwave ranging. The influences of non-gravitational forces, such as atmospheric drag and solar radiation pressure are measured by an on-board accelerometer and subtracted onground by data post-processing. Science data gathered by GRACE are being used to generate a three-dimensional map of the Earth's geoid. The geoid is an equipotential surface of the gravity field of the Earth in the absence of ocean tides, currents, ice-dynamics or weather conditions. It is an important reference extensively used to study variation in the mass distribution. For several years, GRACE data has supported investigations in variations of water and ice mass e.g., polar motion variations, ocean tides and modeling of tectonic plate drift, providing new insight into the global climate.

GRACE was initially planned for a 5-year lifetime. However, the mission has been extended until the end of the satellite lifetime, operating likely for up to 10 years. Due to the huge contribution of GRACE, a follow-on mission has been planned as part of the Decadal Survey in the Earth Sciences to be launched in 2016. For this mission, a laser interferometer has been proposed as an experiment add-on instrument in parallel to the micrometer ranging instrument in order to monitor the inter-satellite distance with more accuracy than it is possible with RF links, designed for a performance goal of $50 \text{ nm}/\sqrt{\text{Hz}}$ in the mHz band.

The AEI is leading the design of the inter-satellite laser interferometer for a GRACE follow-on mission, working with Jet Propulsion Laboratory (JPL), Australian National University (ANU) and industrial partners. Technologies in GRACE follow-on are closely related to the LISA mission. Thus both missions overlap technologies performed in this thesis including heterodyne laser interferometry, laser frequency stabilization tech-

niques, on-board phase measurement systems, and the development of laser transponder with offset-phase locking schemes.

In summary, GRACE follow-on mission and LISA Pathfinder can be considered as precursors of a major mission, LISA, since they use the same underlying measurement principle and similar flight hardware. Thus, LISA Pathfinder will prove the first experimental demonstration of the drag-free technology and pm-level interferometry concept envisaged for LISA, while GRACE follow-on will provide the first demonstration of an inter-satellite interferometry system.

1.3 THE LISA MISSION

Gravitational waves (GWs) were predicted by Albert Einstein on the basis of his general theory of relativity, and today GW are one of the most exciting areas of research in modern physics. Although GWs have not been directly observed yet, indirect evidence for them was enough to earn a Nobel Prize in Physics 1993 (Russell A. Hulse and Joseph H. Taylor). The most promising technique for their detection is based on laser interferometry. Onground GW detectors such as GEO600 (Germany/UK), LIGO/adLIGO (USA), VIRGO (Italy/France), TAMA300 and LCGT (Japan) will likely achieve soon the first direct measurements, thus opening a new window for observing the universe [15, 16]. Terrestrial noise, e.g., seismic and gravity-gradient noise, dominates the sub-Hz regime. Therefore, astrophysical sources of gravitational waves emitting in the low-frequency (mHz) band can be only detected through a space-borne GW detector.

The Laser Interferometer Space Antenna (LISA) is an ESA L-class mission for the Cosmic Vision 2015-2025 programme [4, 17, 18] to observe GW sources in frequency range between 0.1 mHz to 100 mHz. As shown in figure 7, LISA consists of a three spacecraft constellation orbiting around the Sun at 50×10^6 km behind the Earth in a near-equilateral triangle formation with a side length of 5×10^6 km. Three bidirectional laser links are established between satellites, enabling the formation to act as a huge distributed interferometer for monitoring the relative changes in the optical path length induced by gravitational waves. In order to achieve its strain sensitivity goal of $10^{-22}/\sqrt{\text{Hz}}$, the LISA constellation (fig-

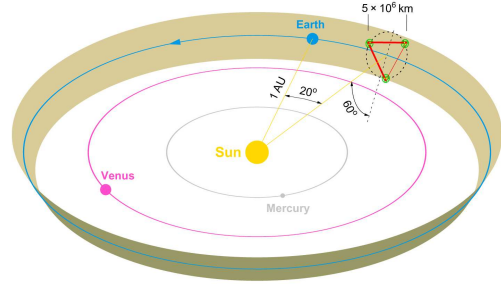


Figure 7: The LISA constellation's heliocentric orbit. The plane of the near-equilateral triangle formation with a side length of 5×10^6 km is inclined at 60 degrees to the ecliptic, and the constellation trails Earth by about 20 degrees (50×10^6 km distance).

ure 8) uses heterodyne interferometry to measure the displacement fluctuations between six free floating test masses enclosed in the three satellites with a sensitivity of $\approx 10 \text{ pm}/\sqrt{\text{Hz}}$ in the mHz band. The received laser beams at $\lambda = 1064 \text{ nm}$ are interfered with a local laser. The phase of the resulting carrier-to-carrier beat note in the MHz range is then measured with an allocated noise budget of $1 \times 10^{-6} \text{ cycles}/\sqrt{\text{Hz}}$.

Starting in the summer of 2011 [19], ESA undertook a reformulation exercise to reduce the cost of LISA after NASA had announced that it cannot commit to its planned contribution in LISA. Options studied in the reformulation include reduction of the arm-length from 5 million km to 1 million km and the number of laser links from six to four. The remainder of this thesis will, however, consider the previous LISA design. The results are applicable to possible modified designs as well, with only small changes of some parameters.

The orbits of the LISA formation are designed to keep the arm lengths as stable as possible in the solar system environment with the resulting arm length variations during one year of about $\pm 1\% \approx 5 \times 10^4 \text{ km}$ and with line-of-sight velocities below 20 m/s . For precision interferometers, this is, however, still an enormous arm length imbalance. Additionally, the beat notes have frequencies of up to 20 MHz due to the Doppler shifts and necessary frequency offsets in the phase locks.

As a consequence, the LISA sensitivity would be limited by two main noise sources: the first one is given by the phase noise of the spacecraft clocks. A timing stability of $50 \text{ fs}/\sqrt{\text{Hz}}$ would be needed to achieve the required phase sensitivity for a beat note at 20 MHz , and such stability is not achievable for any space-qualified clock. The second noise source enters due to the unequal arm length configuration. The laser frequency noise, somewhere between 30 and $1000 \text{ Hz}/\sqrt{\text{Hz}}$ after laser pre-stabilization, directly couples into the phase measurement. One can remove both noise sources using a post-processing technique on the ground called time-delay interferometry [20, 21] (TDI). However, this technique requires additional measurements: the clock phase noise, the absolute distance between the spacecraft to about 1 m , and the clock offset between spacecraft to a few nanosec-

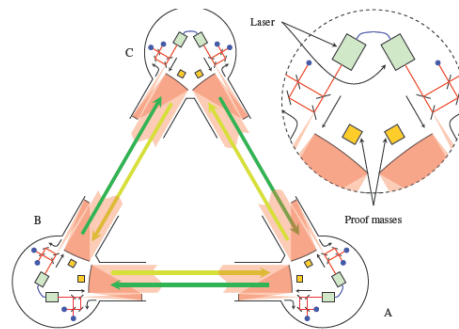


Figure 8: Illustration of the LISA constellation. Three satellites separated by 5 mill km are linked by three bidirectional laser links. Pairs of test-mass from different satellites act as a end-mirror of the interferometer. The interferometry system monitors optical pathlength fluctuations induced by gravitational waves.

onds [22]. These measurements are performed by applying two different phase modulations to the laser link. In order to measure the clock noise, the phase noise of each of the three spacecraft master clocks is multiplied by an integer factor and modulated as high-frequency (GHz) phase modulation sidebands onto each laser link using 10% of the light power. After interference between local and incoming lasers, the phase measurement of the resulting sideband-to-sideband beat note contains the amplified clock noise information necessary to remove the clock noise by TDI. Absolute inter-spacecraft distances are determined with a pseudo-random noise (PRN) phase modulation on each laser carrier using 1% of the optical power [23, 24]. The distance is measured via correlation of the demodulated carrier phase with a local copy of the original PRN code. An important benefit of such a modulation is the possibility of additional data encoding on top of the PRN codes to enable inter-spacecraft communication. A direct measurement of the clock offsets between the three spacecraft to a few nanoseconds is an automatic by-product of this technique, when the measurements are processed onground.

1.4 CONTRIBUTIONS OF THE THESIS

The LISA metrology system has entered an experimental phase, where essential technologies have to be developed and tested. The main contribution of the research presented in this thesis is the development of a novel concept for inter-satellite laser positioning and data communications [23]. The thesis provides a detailed description of the first experimental demonstration of a PRN phase modulation scheme for centimeter distance resolution at ultra-low light power (1 pW) levels applied to precise gravitational wave interferometers. This scheme uses an optical transponder configuration, enabling ranging measurements and data communications at ultra-long transmission distances (5 million kilometers). In addition, this ranging scheme is based on an optical coherent detection system, which improves the receiver sensitivity and frequency selectivity compared with direct-detection receivers [13]. Benefits of the proposed scheme over present technologies [2, 3] include a c.w laser ranging system using a small portion of the total laser power (1% of the optical carrier power). In standard telecommunication systems, the carrier does not contain information. Therefore, a ranging systems can be implemented using 100% of the carrier power. However, in the LISA metrology system, the carrier contains the main scientific information, i.e., optical pathlength fluctuations due to gravitational waves, and therefore the proposed ranging system needs to be designed such that the impact on the laser interferometry is minimal and does not yield limiting factors to the interferometer sensitivity. In addition, the proposed ranging system has been designed such that it can be integrated with additional laser link functionalities such as clock noise transfer and bidirectional data communication capabilities. The on-board clocks are phase modulated as sidebands onto the laser link to provide an extremely high timing stability ($50 \text{ fs}/\sqrt{\text{Hz}}$ over time scales of 1000s of

seconds). Thus, on-board measurements of the clock noise can be conducted using the interferometer itself. This technique is also investigated throughout this doctoral thesis [22], showing the viability of an advanced metrology system that combines absolute distance measurements, data communications, picometer resolution interferometry and clock noise transfer in a single platform based on field programmable gate array (FPGA).

1.5 OUTLINE OF THE THESIS

The proposed metrology scheme is described in details following these four chapters:

- Chapter 2 presents the integration of the ranging scheme into the the LISA interferometry system. In this way, the electro-optical payload is briefly described with special focus on the optical bench interferometry and the metrology architecture for interferometric readout. Here, it is shown that the ranging system is assembled into the science interferometer and processed in or very close to the main interferometric readout.
- Chapter 3 presents the signal characteristics and relevant noise contributions of the LISA metrology system, which impact in either the design of the ranging system or its achievable performance. To this end, a LISA-like signal is modeled and the dominant noise sources are analyzed in terms of their linear spectral noise densities.
- Chapter 4 details the design of ranging system and the digital control loop required to develop the proposed scheme. Besides, it describes a hardware implementation of the proposed metrology architecture as well as the most relevant electrical tests performed to validate the measurement concept.
- Chapter 5 presents the optical experiment built to test the performance of the designed architecture under representative signals of the LISA interferometry system. Here, it is shown the feasibility of this technique for centimeter distance resolution and highly reliable data transfer at several kilobits per second operating within environments of ultra-low light power (1 pW) conditions.

Part I

LISA METROLOGY SYSTEM

LISA INTERFEROMETRY OVERVIEW

The concept of a space-borne gravitational wave observatory has been widely studied during several decades through coordinated studies of a broad science community [25] and industrial partners [26]. Throughout these years, the formulation of the mission baseline design has been published in the form of assessment report and captured in [17, 27, 28, 29]. Currently, a mission formulation study is underway and reported in [30] within the ESA Cosmic Vision 2015-2025 programme.

The use of a Direct-Sequence Spread Spectrum (DS/SS) modulation applied to space-based gravitational wave detectors for laser ranging and data communication was initially suggested in 2002 [31], and the feasibility of this technique has recently been verified and published in [22, 23, 24]. The proposed DS/SS scheme is currently part of the LISA baseline design. This chapter gives an overview of the LISA electro-optical payload that accommodates the laser ranging and data communication scheme into the LISA metrology system.

2.1 LISA ELECTRO-OPTICAL PAYLOAD OVERVIEW

The triangle configuration of the LISA constellation is illustrated in figure 9. The three spacecraft (S/C) are linked by three bidirectional laser links with a nominal length of 5 million km and are operated as laser transponders due to the huge inter-satellite distance. The end-mirrors of each interferometer arm are defined by two free-floating test-masses in different satellites, where their optical pathlength changes are continuously monitored by precise heterodyne interferometry. Each S/C (figure 10) contains two identical optical assemblies (figure 11). Each optical assembly [17] basically consists of:

- A laser system operated at 1064 nm with a frequency pre-stabilization of about $300 \text{ Hz}/\sqrt{\text{Hz}}$ and a fractional power stability of $10^{-3}/\sqrt{\text{Hz}}$ [17]. The laser beam is amplified by a double-clad fiber amplifier to 2 W output power [17, 32] and modulated by a fiber-coupled electro-optical modulator [33] (EOM) for auxiliary functions of the laser link [22] such as clock noise transfer, laser ranging and data communication.
- A 40 cm aperture telescope that receives and transmits the incoming and outgoing laser beams respectively.

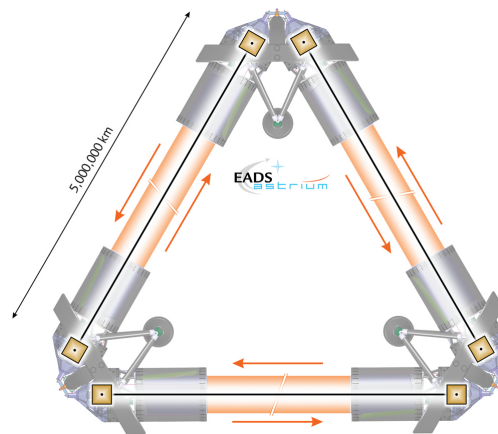


Figure 9: Each spacecraft is equipped with two laser systems, two free-floating test masses identical to LISA Pathfinder mission, and two telescope (40 cm-aperture) pointed to the other two satellites at an angle of 60 degrees. Each laser is transmitted to a remote spacecraft with a power of 2 W and detected at the remote photoreceiver at about 100 pW. The laser links are used for monitoring optical pathlength fluctuations between test-masses from different satellites. Besides, the laser links are phase modulated to perform advanced metrology capabilities, including clock noise transfer, absolute laser ranging and data communication.

- An interferometric measurement system (IMS) that monitors optical pathlength changes between two proof masses on each respective S/C with an accuracy in the range of $10 \text{ pm}/\sqrt{\text{Hz}}$. The IMS operates under weak-light conditions with about 100 pW of incident optical power at the photoreceiver. The IMS includes a FPGA-based metrology system to perform the interferometric readout.
- A gravity reference sensor (GRS) similar to the specified in LISA Pathfinder (section 1.2.1). This way, the GRS carries the test-mass that acts as an end-mirror of the interferometer and as inertial references for the satellite drag-free attitude control.

As represented in figure 12, the baseline design for a single LISA arm splits the interferometry in three parts

- Local proof mass to local optical bench measurement
- Local optical bench to remote optical bench measurement
- Remote optical bench to remote proof mass measurement

This way, two technical challenges are separated: an inter-satellite interferometer at long distances and optical readout of test-mass positioning, a so-called science interferometer and test mass interferometer, respectively. Both are integrated on the optical bench interferometry.

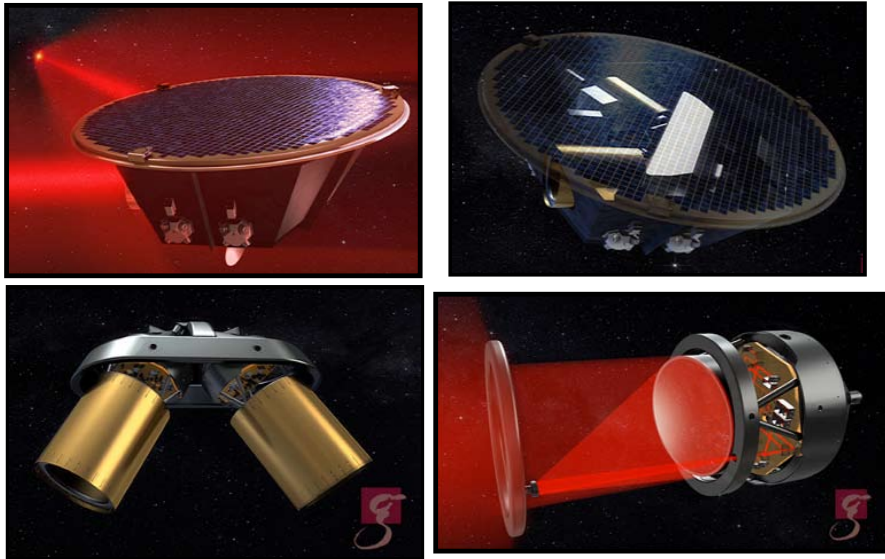


Figure 10: Artist's impression of a LISA spacecraft (S/C). A support structure holds two optical assemblies with an angle 60° . A mechanism to vary that angle by up to $\pm 1.5^\circ$ with a few $\text{nrad}/\sqrt{\text{Hz}}$ resolution maintains a stable triangle formation compensating orbital dynamics through an optical assembly tracking mechanisms.

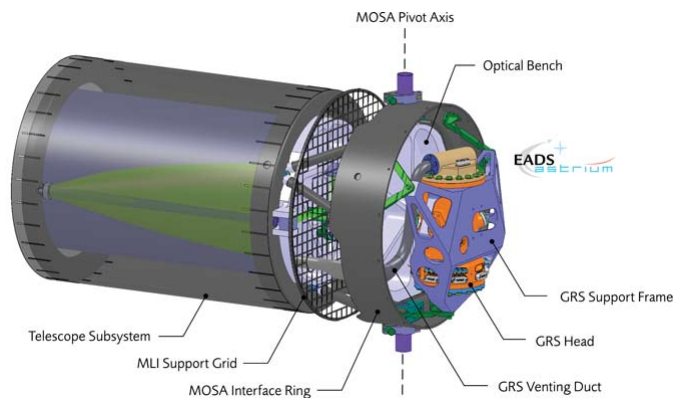


Figure 11: Illustration of the LISA optical assembly. The optical telescope receives and transmits the incoming and outgoing beams, respectively. The optical bench is placed orthogonal to the telescope axis. The gravity reference sensor is assembled at the backside of the optical bench.

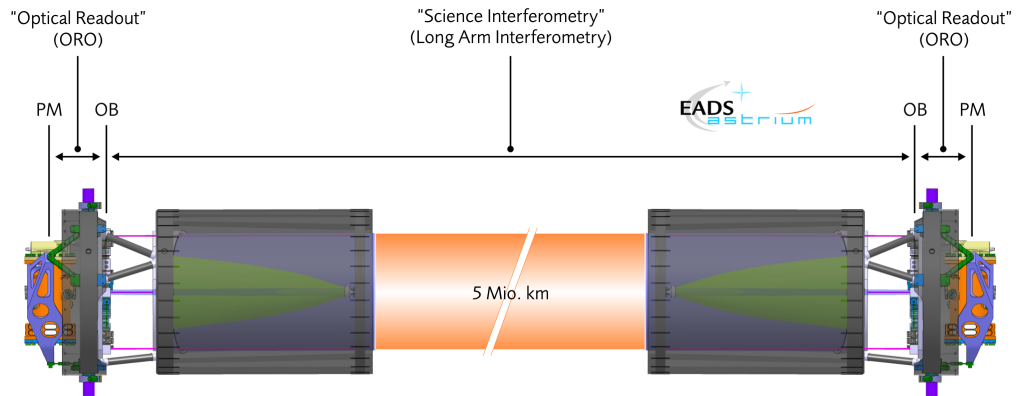


Figure 12: Breakdown of the split interferometry for a LISA arm.

2.2 OPTICAL BENCH INTERFEROMETRY

The LISA optical bench (OB) provides a stable mechanical support for the optical components, e.g., beam-splitters and mirrors as well as for the sensing components like photoreceivers. To this end, the OB is being built using the same technique as in LISA Pathfinder, i.e., the interferometry is bonded on a ceramic Zerodur baseplate with a hydroxy-catalysis bonding technique. This technique allows a high mechanical stability with a low thermal expansion. The optical pathlength noise requirement of the OB interferometry is about $1 \text{ pm}/\sqrt{\text{Hz}}$ in the mHz band. A detail description of the OB interferometry can be found in [34]. Figure 13 shows the current OB layout. The interferometric measurements can be briefly described as

- Science interferometer:** It measures the relative displacement and attitude of the two benches located at opposite ends of a LISA arm. The gravitational wave (GW) signal is contained in small fluctuations of this displacement measurement. The incoming beam is interfered with a local laser and the interferometric signal is detected by two quadrant photodiodes working in hot redundancy. Each detector receives approximately 100 pW of signal power. The phase measurements provide a reference to lock both laser beams in frequency, thus enabling operation of the laser link in a transponder mode (further details in chapter 4). In addition, this interferometer performs the advanced capabilities of the laser link described above, including laser ranging and data communications, and therefore this interferometer is taken as the basis for the realization of this thesis.
- Test-mass interferometer:** It measures the position of the test mass with respect to the local optical bench. The local laser bounces off on the test mass and interferes with the second local laser of the second optical bench. The interferometric signal is sensed by two quadrant photodiodes working in cold redundancy with approximately $90 \mu\text{W}$ of incident optical power.

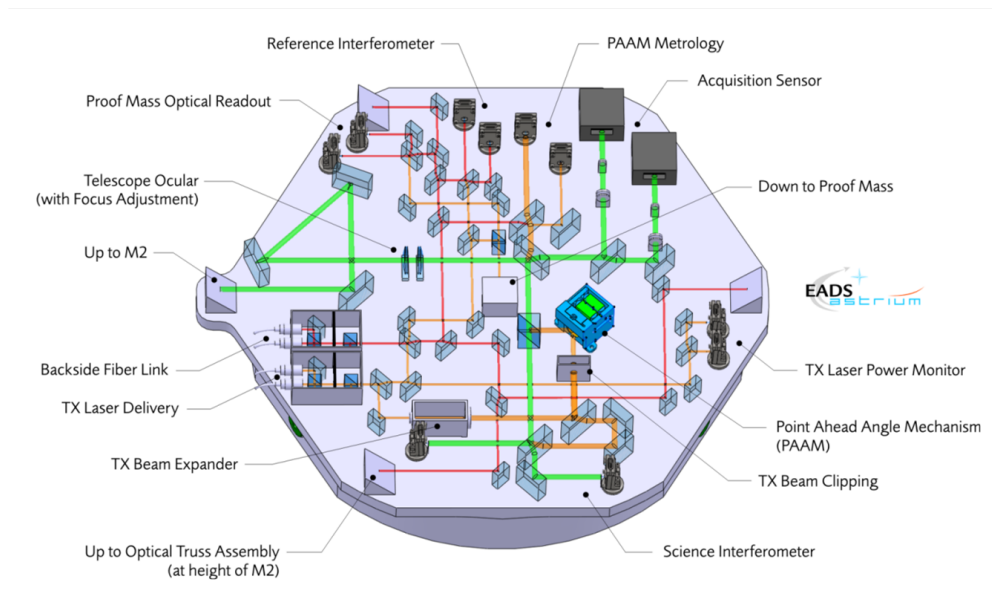


Figure 13: LISA optical bench reference layout.

- The Point Ahead Angle Mechanism (PAAM):** A PAAM interferometer measures the angular displacement between the incoming and outgoing laser beams. A highly mechanical stable PAAM mechanism actuates over the transmission angle of the outgoing beam to compensate the angular variations given by orbital dynamics. The PAAM interferometer uses two split photodiodes working in cold redundancy.
- Reference interferometer:** It establishes a connection between the two local optical benches, providing a low-noise phase reference between interferometric measurements. It aims to reduce the phase noise coupled between laser beams given, for example, by laser frequency noise and residual phase noise in the fiber link between optical benches [35]. The resulting phase reference also enables phase-locking between local lasers. The reference interferometer uses two single photodiodes working in cold redundancy.
- Optical truss interferometer:** This interferometer provides a diagnostic tool of the mechanical stability of the telescope by measuring optical pathlength fluctuations between the telescope and the bench. This interferometer uses three single photodiodes per telescope with no redundancy.

The technology development of key instrumentation for the LISA electro-optical payload, including this optical bench interferometry, is being developed and tested in the framework of the scientific ESA project: *LISA optical bench* [36] at the AEI facilities in close cooperation with the University of Glasgow, EADS Astrium and TNO. Besides,

the LISA metrology system (LMS) for interferometric readout of the optical bench is being also developed at the AEI [37] in collaboration with DTU Space and Axcon Aps, and described in the following section.

2.3 LISA METROLOGY SYSTEM

The core processing of the LMS is based on field-programmable gate array (FPGA). The main task is the measurement of the phase of a heterodyne signal at the output of the photoreceivers on the optical bench. Thus the LMS consists of:

- **The Phase Measurement System (PMS):** It performs the science metrology like precise interferometric phase readout. Besides, the PMS performs the ancillary laser link capabilities: clock noise transfer, laser ranging and data communications. The signal levels and expected noise sources of the LMS are described in chapter 3. The science metrology and the required performance are described throughout chapter 4.
- **The Frequency Distribution System (FDS):** It includes the ultra-stable oscillator (USO), which is the on-board reference clock. The FDS distributes the clock along the metrology system and provides the reference frequency for clock noise transfer.

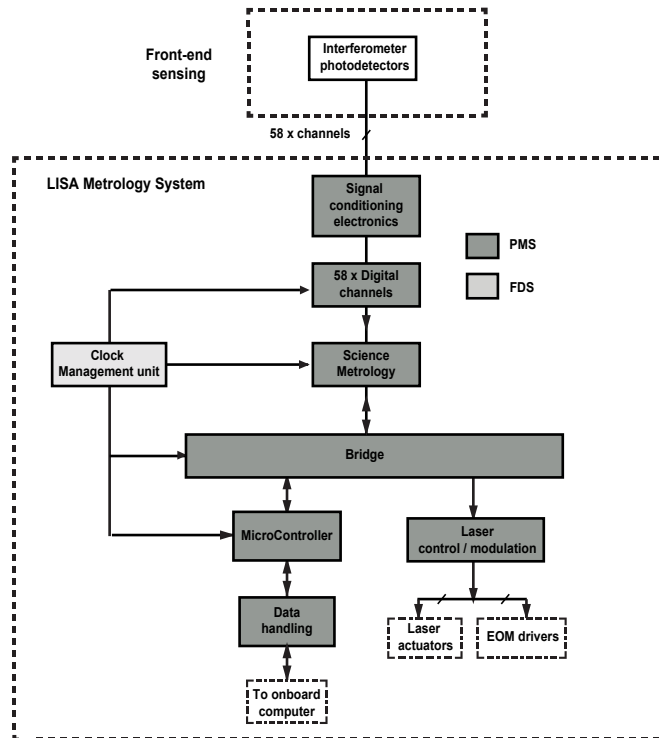


Figure 14: Block diagram at the system level of the LISA metrology system (LMS).

The LMS excludes optical instrumentation such as the optical bench interferometer, telescope, the laser system as well as sensing devices like the photoreceivers. Figure 14 shows a description at the system level of the LMS. The LMS is connected to the photoreceivers of the optical bench requiring 29 analog channels per bench, and therefore 58 channels (for 2 benches) per satellite, not including redundancy. Of these, 40 channels are simultaneously active in science mode. The signal processing of the science interferometer is the most challenging part from the point of view of the LMS, and as already mentioned it is taken as the basis for the realization of this thesis. Each LMS channel processes the interferometric signal, tracking slowly varying frequencies (± 4 Hz/s) in the frequency range between 2 MHz to 20 MHz, and delivering a phase estimation to the on-board computer at a constant rate of 3 Hz-10 Hz with an accuracy of $2\pi 10^{-6}$ rad/ $\sqrt{\text{Hz}}$ in the mHz band. The DS/SS modulation requires an EOM driver to modulate the pseudo-random noise (PRN) codes together with the transmission of the GHz clock sideband signals. In addition, the LMS also performs laser control to phase lock the incoming and outgoing beams for an optical transponder configuration. A more detailed insight into the LMS is given by the following chapters. Among the key objectives of this thesis are the validation of the LMS by developing a breadboard of the PMS (see chapter 4) as well as the development of a testing setup to show compliance with required performance (see chapter 5) for laser ranging and data communications.

LISA METROLOGY SYSTEM: SIGNAL MODEL AND NOISE SOURCES OVERVIEW

Laser metrology systems based on optical heterodyne detection are a promising technique for space-borne measurements of amplitude and phase of a received laser beam at a frequency ν_s , typically in the THz band. In contrast to non-coherent detection schemes, this method leads to an achievable phase sensitivity of microradian noise level, even when the received beam is detected at low light power levels. A strong local oscillator (LO) signal at a frequency ν_l is used as a stable light reference, and recombined with the incoming beam translates the information of the received signal to the radio-frequency (RF) band, i.e., to a designed intermediate frequency $\nu_{\text{het}} = \nu_s - \nu_l$, being then easily processable by standard electronics¹. The resulting beat signal is detected by a photoreceiver so that its photocurrent is a phase replica of the optical signal relative to the stable local reference, but moved to a lower frequency range. Thus, this technique enables the development of precise laser metrology systems through phase measurements of optical wavelengths (typically in the nanometer range), allowing the monitoring of relative displacements at sub-nanometer accuracy.

The baseline architecture of the opto-electronic front end, and the structure of a LISA-like signal impinging at one of the photoreceivers is described in section 3.1. The LISA metrology system (LMS) has been designed to be shot noise limited [17]. Nevertheless, the excess noise coupled by the analog detection chain could compromise the phase readout performance of the proposed experimental realization. From section 3.2 to section 3.5, the contributions of individual noise sources in the analog front-end are examined as well as their resulting impact on the phase performance of the proposed LMS (described in chapter 2 and chapter 4). In section 3.6, the applied phase modulations for advanced laser link capabilities are analyzed, setting the required optical power allocated to these modulations in terms of their modulation indices. Section 3.7 describes the Doppler shifts that result at the input of the metrology system given by orbital motion of the satellites. This effect has a significant impact on the design of the LMS. Finally, section 3.8 describes the effect of an idealized GW signal on the basis of its expected phase shift induced on an optical link.

¹ In LISA, the LO phase is tightly controlled to provide a stable heterodyne beat signal in the MHz frequency range

3.1 OPTO-ELECTRONICS FRONT-END

In the science and the test-mass interferometers defined in chapter 2, quadrant photodetectors (QPD) are used for monitoring the angular beam motion via differential wavefront sensing (DWS) [38, 39]. As a by-product of separate phase measurements on independent quadrant segments, this technique enables tilt measurements between the two incident beams for precise laser pointing [40], as well as angular test-mass motions for satellite drag-free control [41, 42]. Figure 15 shows a block diagram of the signal detection chain. The front-end electronics accept the photocurrent from the four QPD segments and amplify them for a digital signal processor based on a field programmable gate array (FPGA) unit for independent optical readouts. Each front-end channel consists typically of an InGaAs quadrant photodiode with a transimpedance amplifier (TIA), and the signal-conditioning electronics, which consists of an anti-aliasing filtering (AAF) and variable gain controller (VGC). The first amplification stage is the most critical part in the analog chain design. It has to maintain nearly shot noise limited performance over a measurement bandwidth up to 20 MHz range as well as to provide a relatively large signal-to-noise ratio (SNR) to the following components. The signal conditioning electronics is responsible for adapting the input signal in bandwidth and amplitude to the optimal dynamic range of the analog-to-digital converter (ADC) (see details in section 3.5). The digitized signals are processed in a FPGA to perform phase measurements as core processing (see section 4.6), i.e., monitoring of longitudinal optical pathlength displacements and the DWS angle measurements. The eight segments (2 QPDs) are operated in a hot redundant configuration, and combined to a single longitudinal signal. The metrology system performs in back-end processing the auxiliary functions of the laser links, including clock noise transfer, absolute laser ranging measurements, and data communications.

As derived in appendix A.1, a signal model of the incident power for a single segment of a quadrant photodiode is given by

$$P_{\text{pd}}(t) = \underbrace{\frac{P_{\text{LO}}}{2N} + \frac{P_s}{2N}}_{\text{DC}} + \underbrace{\frac{1}{N} \sqrt{P_{\text{LO}} P_s} \gamma \cdot \sin(\omega_{\text{het}} t + \Delta\phi)}_{\text{AC: beat note}} \quad [\text{W}], \quad (3.1)$$

where P_s and P_{LO} are the available optical powers in front of the beam splitter for the incoming and the local oscillator beams respectively. N is the number of segments in the photodiode at one of the two equivalent output ports of the beam splitter, $N = 4$ in a QPD or $N = 1$ for a single-element photodiode. γ is a factor describing the mode overlap between the two lasers ($0 \leq \gamma \leq 1$), known as heterodyne efficiency, and denotes the quality of the interference. ω_{het} is the angular heterodyne frequency of the beat note, which corresponds to the difference $\omega_{\text{het}} = 2\pi\nu_s - 2\pi\nu_l$ between the

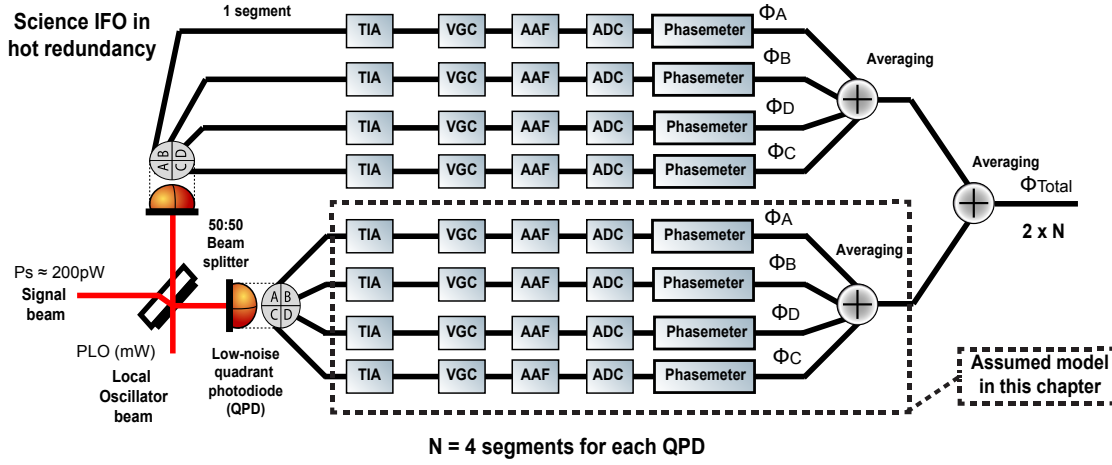


Figure 15: Block diagram of the opto-electronics front-end. The signal detector chain is based on optical heterodyne detection with four independent phase readouts for tilt measurements through differential wavefront sensing (DWS). Each segment comprises a transimpedance amplifier (TIA), an anti-aliasing filter (AAF), and a variable gain controller (VGC). The analog signal is digitized by an analog-to-digital converter (ADC), and processed in a field-programmable gate array (FPGA) unit for science measurements.

optical frequencies. Either $\Delta\phi$ or simply ϕ denotes the phase of the beat note which contains the science information.

From equation 3.1 it is possible to state two important features of heterodyne receivers. First, this scheme enables the design of the beat note within a certain frequency range which depends on the designed frequency plan, thus translating the optical phase information from an electronically undetectable frequency band (THz) to a more benign frequency range for standard electronics, e.g. the designed MHz band given for LISA. As second design parameter, equation 3.1 shows that the amplitude of the beat note is proportional to the $\sqrt{P_{LO}}$ optical power. Therefore, the local laser can be used to control the beat note signal level amplitude well above the measurement noise, thus amplifying the received weak signal above the noise floor. While a relatively strong LO power enhances the signal level in the detection scheme, there are also upper limits given by the optical metrology requirements in order to reduce power dissipation from the detection electronics and thermal effects on the optical bench, and by the influence of laser intensity noise. In the optical range of LO powers (i.e., such that neither electronic noise nor laser intensity noise are a significant contribution), the effective SNR is given by the shot noise and independent of the LO power, as both signal and shot noise increase similarly proportional to the square root of the LO power. This will be discussed in detail in the following sections.

3.2 SHOT NOISE LIMIT

The science interferometer (see section 2.2) aims to ultimately reach a sensitivity performance limited by shot noise. This interferometer has to handle the low power level of the incoming laser light. The available optical power (100 pW), yields to a fundamental limit in the residual phase fluctuations on the weak beam, which is known as shot noise limit. It is caused by the statistical phase distribution of the detected photons [43]. Thus, the shot noise limit to the phase measurement needs to be calculated. The photocurrent $I_{\text{seg}}(t)$ on each segment of a QPD is proportional to the total incident optical power according to

$$I_{\text{seg}}(t) = \eta P_{\text{pd}}(t) = \eta \left[\frac{P_{\text{LO}}}{2N} + \frac{P_s}{2N} + \frac{1}{N} \sqrt{P_{\text{LO}}P_s\gamma} \cdot \sin(\omega_{\text{het}}t + \phi) \right] \quad [\text{A}], \quad (3.2)$$

where η is the responsivity of the photoreceiver, typically $\eta = 0.7 \text{ A/W}$ for an InGaAs photodiode at a wavelength of 1064 nm. The shot noise is computed based on the total average (DC) photocurrent². For weak-light conditions $P_s \ll P_{\text{LO}}$, the shot noise level is dominated by the contribution of the LO beam power. Thus, the single-sided linear spectral density of the shot noise $\tilde{i}_{\text{seg}}^{\text{sn}}(f)$ in the photocurrent of a single PD segment is given by

$$\tilde{i}_{\text{seg}}^{\text{sn}}(f) = \sqrt{2q_e I_{\text{dc}}} \approx \sqrt{\frac{q_e \eta P_{\text{LO}}}{N}} \quad [\text{A}/\sqrt{\text{Hz}}], \quad (3.3)$$

where q_e is the electron charge ($1.602 \times 10^{-19} \text{ C}$). Although $\tilde{i}_{\text{seg}}^{\text{sn}}(f)$ is written as a function of f , shot noise presents a white noise distribution with a flat power spectral density. As described in appendix B.1, and taking into account equation 3.2 and equation 3.3, it is possible to compute the resulting phase noise as a function of the carrier to noise power density ratio (C/N_0)

$$\tilde{\vartheta}_{\text{seg}}^{\text{sn}}(f) = \frac{1}{\sqrt{C/N_{\text{seg}}^{\text{sn}}}} = \frac{\tilde{i}_{\text{seg}}^{\text{sn}}(f) \approx \sqrt{\frac{q_e \eta P_{\text{LO}}}{N}}}{I_{\text{seg}}^{\text{AC}}(t) = \frac{\eta}{N} \sqrt{P_s P_{\text{LO}} \gamma} \cdot \frac{1}{\sqrt{2}}} = \sqrt{\frac{2q_e N}{\eta P_s \gamma}} \quad [\text{rad}/\sqrt{\text{Hz}}]. \quad (3.4)$$

This easy to remember relationship (phase noise in $\text{rad}/\sqrt{\text{Hz}} = 1/\sqrt{C/N_0}$) can also be applied for additive noise sources in the front-end electronics, including phase errors due to electronic noise and laser intensity fluctuations. The last $1/\sqrt{2}$ reflects the fact that $I_{\text{seg}}^{\text{AC}}(t)$ is expressed as rms value as opposed to the sine amplitude in equation 3.2.

² This is an approximation good enough for the present purpose. Fine corrections can be found in [44, 45].

Converting phase into pathlength, the equivalent optical pathlength noise limit due to shot noise is

$$\tilde{\chi}_{\text{seg}}^{\text{sn}}(f) = \frac{\lambda}{2\pi} \cdot \sqrt{\frac{2q_e N}{\eta P_s \gamma}} \quad [\text{m}/\sqrt{\text{Hz}}]. \quad (3.5)$$

Although the shot noise level in the photocurrent is dominated by the contribution of the relatively strong LO optical power (equation 3.3), the phase sensitivity however, is limited by the received signal power (equation 3.5). The reason is that both shot noise and signal increase in parallel proportional to $\sqrt{P_{\text{LO}}}$. This implies that the weak optical signal received in LISA from the remote spacecraft leads to a fundamental noise limit in the phase sensitivity of the interferometer. For example, assuming a total received power of $P_s = 200 \text{ pW}$, a heterodyne efficiency of 0.8, and a photodiode responsivity of 0.7 A/W , the resulting optical pathlength noise per segment due to the shot noise is $\tilde{\chi}_{\text{seg}}^{\text{sn}}(f) \approx 18 \text{ pm}/\sqrt{\text{Hz}}$. By averaging the four segments, the total shot noise level yields to $\tilde{\chi}_{N_{\text{seg}}}^{\text{sn}}(f) \approx 9 \text{ pm}/\sqrt{\text{Hz}}$. Moreover, with all eight segments, the shot noise levels is $\tilde{\chi}_{2N_{\text{seg}}}^{\text{sn}}(f) \approx 6 \text{ pm}/\sqrt{\text{Hz}}$. To avoid excess instrumental noise, and therefore to achieve optical sensitivity with a nearly shot noise limited performance, each element in the interferometric chain gets allocated a pathlength noise budget of less than $2 \text{ pm}/\sqrt{\text{Hz}}$.

3.3 ELECTRICAL NOISE BUDGET

A transimpedance amplifier (TIA) converts the photocurrent (equation 3.2) into a proportional voltage. The residual noise introduced by the TIA needs to be lower than the shot noise limit, otherwise the phase sensitivity of the LISA metrology breadboard would be limited by this technical noise. The target noise budget for the input current noise is better than $\tilde{i}_{\text{seg}}^{\text{en}}(f) \approx 3 \text{ pA}/\sqrt{\text{Hz}}$ in the beat note frequency band. Thus, the phase noise induced by electronic noise can be estimated by

$$\tilde{\vartheta}_{\text{seg}}^{\text{en}}(f) = \frac{1}{\sqrt{C/N_{\text{seg}}^{\text{en}}}} = \frac{\sqrt{2} \cdot \tilde{i}_{\text{seg}}^{\text{en}}(f) \cdot N}{\eta \sqrt{P_{\text{LO}} P_s \gamma}} \quad [\text{rad}/\sqrt{\text{Hz}}]. \quad (3.6)$$

A model of the main input current noise sources for a LISA-like photoreceiver is described in appendix C.1.

3.4 OPTICAL NOISE BUDGET

Commercial laser systems [46] are taken as reference in this section since they are being widely used in precision experiments due to their high frequency stability and their optical output powers. Their physical properties are also representative for laser

considered as candidates to be flown in LISA [17]. The active medium is a monolithic neodymium-doped Yttrium Aluminum garnet (Nd:YAG) crystal in a non-planar ring oscillator (NPRO) topology. That type of laser has two control ports for the laser frequency to actuate the temperature of the crystal and the resonator geometry through a piezo-electric transducer. These actuators produce optical pathlength changes in the resonator to control the output frequency of the laser. This allows to close feedback loops for offset-phase locking between two different lasers in order to control the beat note frequency. In this section, the relevant noise sources such as laser power noise, frequency fluctuations and beam misalignment are described.

3.4.1 Laser intensity noise

Similar to the shot noise and electronic noise, laser power fluctuations couple to the photocurrent as

$$\tilde{i}_{\text{seg}}^{\text{RIN}}(f) = \text{RIN} \cdot \eta \cdot \frac{P_{\text{LO}}}{2N} \quad [\text{A}/\sqrt{\text{Hz}}]. \quad (3.7)$$

Thus an equivalent phase noise contribution of

$$\tilde{\vartheta}_{\text{seg}}^{\text{RIN}}(f) = \frac{1}{\sqrt{C/N_{\text{seg}}^{\text{RIN}}}} = \frac{\sqrt{2} \cdot \tilde{i}_{\text{seg}}^{\text{RIN}}(f) \cdot N}{\eta \sqrt{P_{\text{LO}} P_s \gamma}} = \text{RIN} \cdot \sqrt{\frac{P_{\text{LO}}}{2P_s \gamma}} \quad [\text{rad}/\sqrt{\text{Hz}}], \quad (3.8)$$

where RIN is the relative intensity noise, which denotes fluctuations in the laser power relative to the average absolute power level. Figure 16 (left side) shows the measured RIN of a NPRO laser at the wavelength of 1064 nm in the relevant frequency band. The plot on the right side represents the induced phase noise due to laser intensity fluctuations (equation 3.7) and the shot noise floor reference per segment (equation 3.4). It assumes typical values in accordance with the LISA design [47], i.e., a signal optical power of $P_s = 200$ pW, a local oscillator optical power of $P_{\text{LO}} = 3.44$ mW, a heterodyne efficiency γ of 0.8, and photodiode responsivity η of 0.7 A/W. The excess laser power noise below 5 MHz is due to the relaxation oscillation of the laser.

Figure 17 and figure 18 show a comparison of the impact of the RIN and the electronic noise for the science interferometer, with a typical optical signal power of 200 pW, and the test-mass interferometer, with a designed signal power of 90 μ W. The residual pathlength noise introduced by the RIN is dominated by the available signal power and the relatively strong LO power. The phase noise in the beat note of the test-mass interferometer is not limited by the residual RIN. The science interferometer requires a RIN lower than $2 \times 10^{-8}/\sqrt{\text{Hz}}$ and a local oscillator power at milliwatts levels to achieve a RIN-driven phase noise contribution below the shot noise limit.

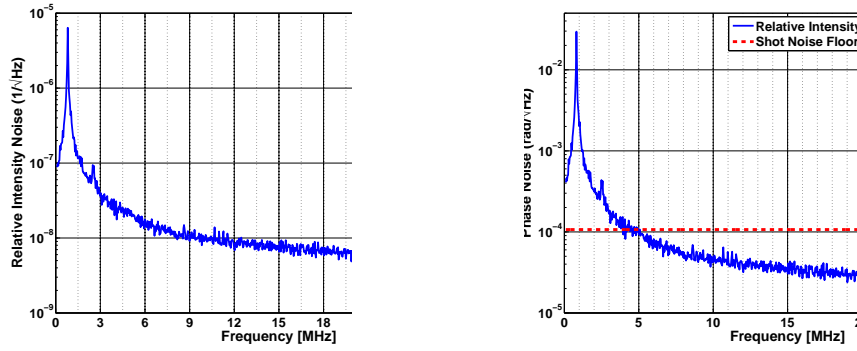


Figure 16: Left side: Measured relative intensity noise of a non-planar ring oscillator laser. Right side: induced phase noise due to laser intensity fluctuations and shot noise floor reference.

Table 1 and figure 19 summarize the noise contributions described in this chapter in terms of photocurrent noise. For shot noise and laser intensity noise, their noise contributions are proportional to $\sqrt{P_{LO}}$ and P_{LO} respectively, while the electronic noise is independent of P_{LO} . Since the signal is proportional to $\sqrt{P_{LO}}$, the equivalent phase noise contributions are proportional to 1, $\sqrt{P_{LO}}$ and $1/\sqrt{P_{LO}}$ respectively. In contrast to laser intensity noise, shot noise and electronic noise are non-correlated contributions between QPD segments. Moreover, electronic noise is independent of P_{LO} , thus the effect of this contribution can be reduced by increasing P_{LO} . In summary, the contributions from both shot noise and laser RIN results in a noise level that is independent of whether that result is obtained with a single-element photodiode or by averaging four QPD segments. For the case of preamplifier noise, given the multichannel stages, its influence increases by \sqrt{N} with respect to the case of a single element photodiode.

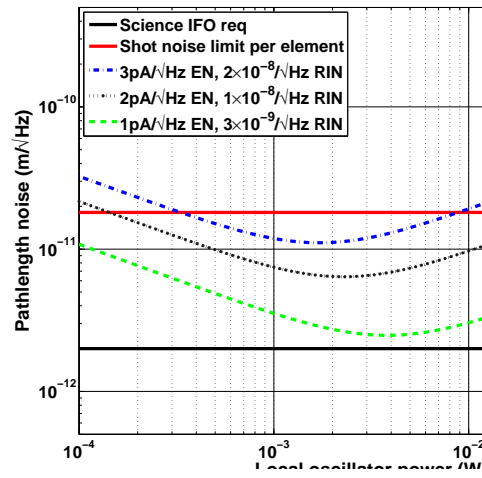


Figure 17: Equivalent displacement noise for the science interferometer readout with a signal light power of 200 pW.

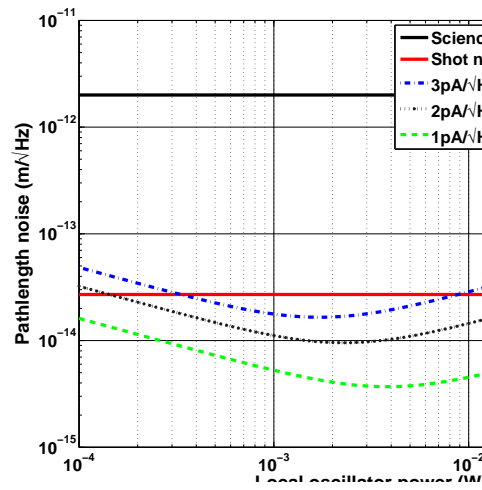


Figure 18: Equivalent displacement noise for the test-mass interferometer readout with a signal light power of 90 μW.

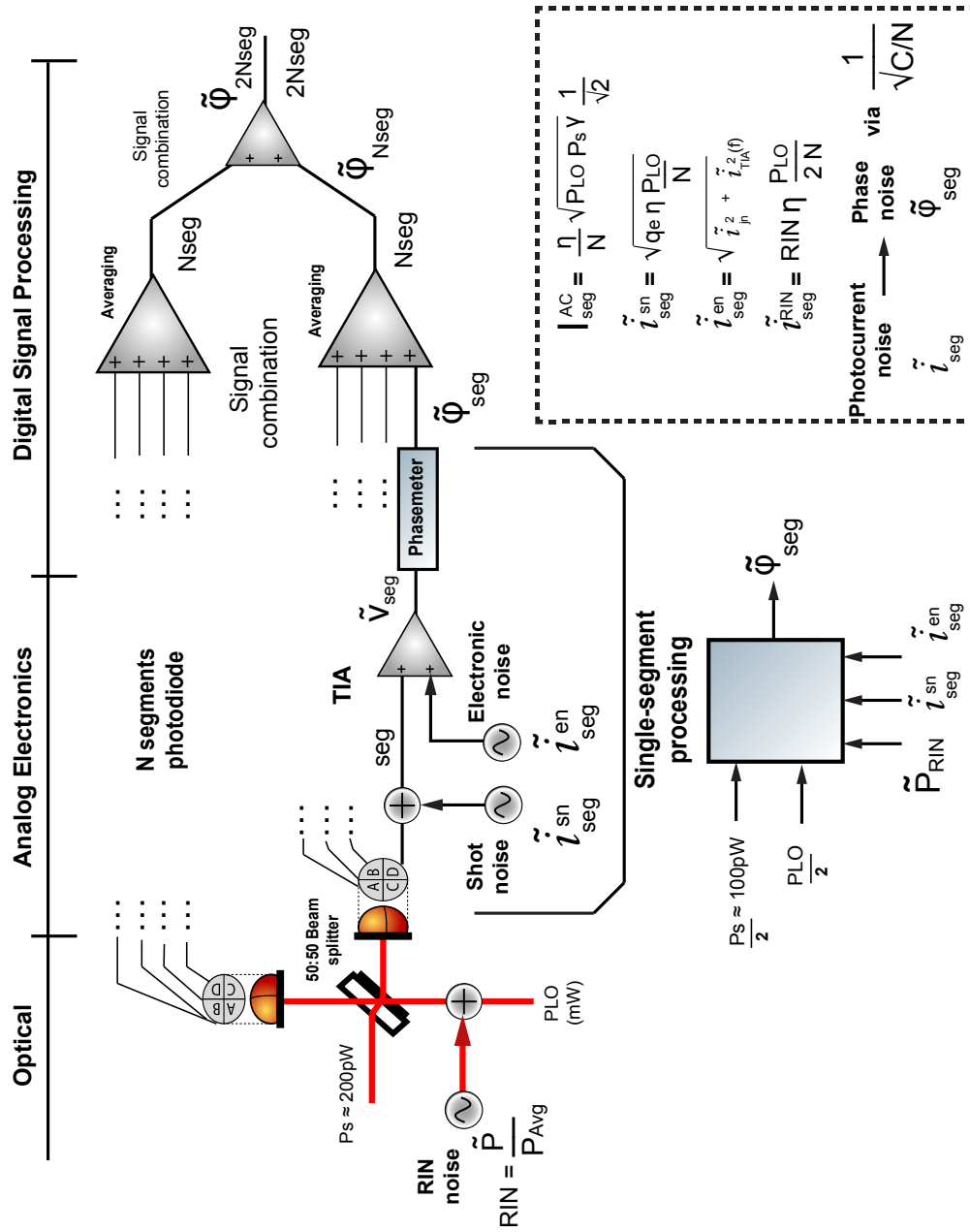


Figure 19: Topology and noise model of the opto-electronic front-end in terms of a single QPD segment. It sketches laser intensity noise, shot noise and electronic noise. The different photocurrent noise contributions are converted to phase noise via $1/\sqrt{C/N_0}$.

Detector Type	Photocurrent Signal (rms)	Photocurrent Shot Noise (rms)	Photocurrent Electronic Noise (rms)	Photocurrent RIN (rms)
SE	$I_{se}^{DC} = \eta \sqrt{P_{LO} P_s \gamma} \cdot \frac{1}{\sqrt{2}},$ $I_{se}^{AC} = \eta \sqrt{P_{LO} P_s \gamma} \cdot \frac{1}{\sqrt{2}},$	$\tilde{i}_{se}^{sn}(f) = \sqrt{q e \eta P_{LO}},$	$\tilde{i}_{se}^{en}(f),$	$\tilde{i}_{se}^{RIN}(f) = RIN \cdot \eta \frac{P_{LO}}{2},$
1 Seg	$I_{seg}^{DC} = \eta \frac{P_{LO}}{2N},$ $I_{seg}^{AC} = \frac{\eta}{N} \sqrt{P_{LO} P_s \gamma} \cdot \frac{1}{\sqrt{2}},$ $I_{seg}^{AC} = \frac{I_{se}^{AC}}{N},$	$\tilde{i}_{seg}^{sn}(f) = \sqrt{q e \eta} \frac{P_{LO}}{N},$ $\tilde{i}_{seg}^{sn}(f) = \frac{\tilde{i}_{se}^{sn}(f)}{\sqrt{N}},$	$\tilde{i}_{seg}^{en}(f) = \tilde{i}_{se}^{en}(f),$	$\tilde{i}_{seg}^{RIN}(f) = RIN \cdot \eta \frac{P_{LO}}{2N},$ $\tilde{i}_{seg}^{RIN}(f) = \frac{\tilde{i}_{se}^{RIN}(f)}{N},$
Linear addition				
Quadrature addition				
NSeg	$\frac{1}{N} \cdot \sum_i^N [I_{seg,i}^{DC} + I_{seg,i}^{AC}],$ $I_{Nseg}^{AC} = I_{seg}^{AC},$ $I_{Nseg}^{AC} = \frac{I_{se}^{AC}}{N},$	$\frac{1}{N} \cdot \sqrt{\sum_i^N \tilde{i}_{seg,i}^{sn}(f)^2},$ $\tilde{i}_{Nseg}^{sn}(f) = \sqrt{N} \cdot \frac{\tilde{i}_{seg}^{sn}(f)}{N},$ $\tilde{i}_{Nseg}^{sn}(f) = \frac{\tilde{i}_{se}^{sn}(f)}{N},$ $\tilde{\vartheta}_{Nseg}^{sn}(f) = \tilde{\vartheta}_{se}^{sn}(f)$	$\frac{1}{N} \cdot \sqrt{\sum_i^N \tilde{i}_{seg,i}^{en}(f)^2},$ $\tilde{i}_{Nseg}^{en}(f) = \sqrt{N} \cdot \frac{\tilde{i}_{seg}^{en}(f)}{N},$ $\tilde{i}_{Nseg}^{en}(f) = \sqrt{N} \cdot \frac{\tilde{i}_{se}^{en}(f)}{N},$ $\sqrt{N} \cdot \tilde{\vartheta}_{Nseg}^{en}(f) = \tilde{\vartheta}_{se}^{en}(f)$	$\frac{1}{N} \cdot \sum_i^N \tilde{i}_{seg,i}^{RIN}(f),$ $\tilde{i}_{Nseg}^{RIN}(f) = \tilde{i}_{seg}^{RIN}(f),$ $\tilde{i}_{Nseg}^{RIN}(f) = \frac{\tilde{i}_{se}^{RIN}(f)}{N},$ $\tilde{\vartheta}_{Nseg}^{RIN}(f) = \tilde{\vartheta}_{se}^{sn}(f)$
$\boxed{SNR_{Nseg}^{sn} = SNR_{SE}^{sn}}$				
$\boxed{SNR_{Nseg}^{en} = \sqrt{N} \cdot SNR_{SE}^{en}}$				
$\boxed{SNR_{Nseg}^{RIN} = SNR_{SE}^{RIN}}$				
Linear addition				
Quadrature addition				
2NSeg	$I_{2Nseg}^{DC} = \eta P_{LO},$ $I_{2Nseg}^{AC} = \eta \sqrt{2P_{LO} P_s \gamma},$	$\tilde{i}_{2Nseg}^{sn}(f) = \sqrt{2q e \eta P_{LO}},$ $\tilde{\vartheta}_{2Nseg}^{sn}(f) = \sqrt{\frac{q e}{\eta P_s \gamma}},$ $\tilde{\vartheta}_{2Nseg}^{sn}(f) = \sqrt{2} \tilde{\vartheta}_{2Nseg}^{sn}(f),$	$\tilde{\vartheta}_{2Nseg}^{en}(f) = \sqrt{2} \tilde{\vartheta}_{2Nseg}^{en}(f),$	$\tilde{\vartheta}_{2Nseg}^{RIN}(f) = RIN \sqrt{\frac{P_{LO}}{2P_s \gamma}},$ $\tilde{\vartheta}_{2Nseg}^{RIN}(f) = \tilde{\vartheta}_{2Nseg}^{RIN}(f),$
$\boxed{SNR_{2Nseg}^{sn} = \sqrt{2} SNR_{Nseg}^{sn}}$				
$\boxed{SNR_{2Nseg}^{en} = \sqrt{2} SNR_{Nseg}^{en}}$				
$\boxed{SNR_{2Nseg}^{RIN} = SNR_{Nseg}^{RIN}}$				

Table 1: Noise contributions in the opto-electronics front end for shot noise (sn), electronic noise (en) and relative intensity noise (RIN). For comparison, four cases were considered: a single-element photodiode (SE), a single segment (Seg), the averaging of N segments of a QPD (NSeg), and the case of hot redundancy, the averaging of two times N segments (2NSeg).

3.4.2 Laser frequency noise

Laser frequency noise is the major noise source of the LISA mission, setting stringent requirements in the design of its interferometry system. As a consequence of the orbital motion, the length of the three LISA interferometric arms will be unequal and time-varying with a maximum mismatch of $\Delta L \approx 1 \times 10^8$ m so that laser frequency fluctuations $\delta\tilde{\nu}$ will couple via the arm-length difference ΔL into pathlength fluctuations $\delta\tilde{x}$ given by the following displacement sensitivity

$$\delta\tilde{x} = \Delta L \frac{\delta\tilde{\nu}}{\nu} \quad [\text{m}/\sqrt{\text{Hz}}],$$

and equivalent phase sensitivity (3.9)

$$\delta\tilde{\phi} = \frac{2\pi}{c} \Delta L \delta\tilde{\nu} = \delta\tilde{\omega} \frac{\Delta L}{c} \quad [\text{rad}/\sqrt{\text{Hz}}].$$

For an allocated pathlength noise budget of ≈ 1 pm/ $\sqrt{\text{Hz}}$ at 3 mHz, the required frequency stability is 2.8×10^{-6} Hz/ $\sqrt{\text{Hz}}$. With an inherent free-running laser frequency noise of typically

$$\delta\tilde{\nu}_{\text{free}} \approx \frac{10^4}{f} \quad [\text{Hz}/\sqrt{\text{Hz}}], \quad (3.10)$$

the noise suppression needs to be up to 10^{12} . This challenge will be overcome by an initial laser pre-stabilization to a stable frequency reference, an optional further stabilization to the long arm (called arm-locking [48, 49]) and afterwards a suppression of residual noise through time-delay interferometry (TDI). Thus, the different stages in the laser frequency control are:

- The first stage of the LISA frequency noise control scheme reduces the free-running noise of a master laser by locking it to a stable frequency reference [50]. Three main techniques have been widely investigated for LISA. The first one consists of an active pre-stabilization by using either a reference cavity or a molecular frequency standard such as iodine. These pre-stabilization techniques have been demonstrated in several research centers such as Goddard Space Flight Center (GSFC) and at the AEI with a proven frequency stability of up to $\delta\tilde{\nu} = 30$ Hz/ $\sqrt{\text{Hz}}$ at 3 mHz. In addition, a Mach-Zehnder stabilization has been proposed for LISA. It uses a scheme quite similar to the frequency stabilization for the LISA Technology Package (LTP) on-board LISA Pathfinder, achieving

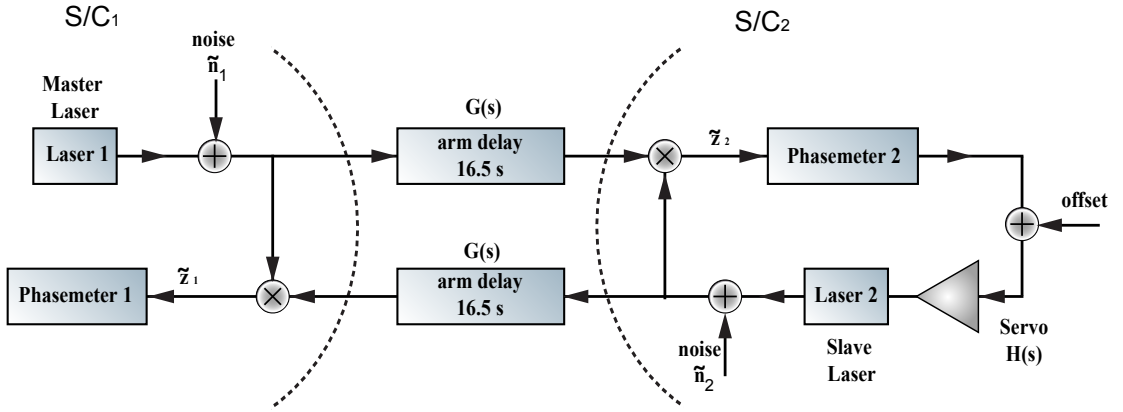


Figure 20: Linear model of the control loop for the laser transponder scheme.

frequency noise suppression around hundreds of $\text{Hz}/\sqrt{\text{Hz}}$. Once the master laser has been pre-stabilized with one of these active method, the other five lasers in LISA will inherit its frequency stability through offset phase-locking.

- The final step in the laser frequency noise suppression is based on the TDI algorithm. It uses precise measurements of the absolute inter-satellite distance in order to synthesize an equal arm-length interferometer. The TDI algorithm is limited by residual laser frequency noise and the ranging accuracy, i.e., assuming a laser pre-stabilization of $30 \text{ Hz}/\sqrt{\text{Hz}}$ and a ranging accuracy of 10 meters, this algorithm should be capable of achieving the required phase sensitivity of the mission. As shown in the following equation

$$\delta\tilde{\nu} = 300 \text{ Hz}/\sqrt{\text{Hz}} \times \left(\frac{1\text{m}}{\Delta L} \right) \times \left(\frac{\delta\tilde{x}}{1 \text{ pm}/\sqrt{\text{Hz}}} \right), \quad (3.11)$$

improvements in the ranging accuracy to the level of 1 meter lead to a relaxation of laser pre-stabilization requirements to the level of $\approx 300 \text{ Hz}/\sqrt{\text{Hz}}$, and therefore it would significantly reduce the complexity on the technology development of the LISA interferometry system.

Phase errors induced in the beat notes by laser frequency noise can be described considering the two stages of the lasers explained above: free-running and pre-stabilized.

Figure 20 shows the principle of operation of the laser transponder configuration for a LISA arm. A master laser with a laser frequency noise of n_1 is transmitted to a remote satellite. After a trip propagation delay of $\tau = L/c \approx 16.5 \text{ s}$ ($G(s) = e^{-s\tau}$, with

$s = i\omega = 2\pi i f$, i.e., Laplace variable), the incoming beam is recombined (modeled as a mixer) with the local slave laser and the resulting beat note processed in the phase measurement system. An offset phase locking scheme with a transfer function $H(s)$ controls the slave laser to return a high power replica of the incoming beam. After an overall propagation delay of $2\tau \approx 33$ s, the returning beam is recombined with the original laser in the master spacecraft and measured by its local phasemeter. By using standard control loop theory, the expected beat note frequency noise spectra can be easily derived for the laser frequency noise at the input of their respective phasemeters, yielding to

$$\tilde{z}_1^2 = \tilde{n}_1^2 \cdot \left| \frac{H(s)}{1+H(s)} \cdot e^{-2s\tau} - 1 \right|^2 + \tilde{n}_2^2 \cdot \left| \frac{e^{-s\tau}}{1+H(s)} \right|^2, \quad (3.12)$$

for the phasemeter in the master satellite, and where \tilde{z} is the linear spectral density given at the input of the phasemeter and \tilde{n} is the linear spectral density of the laser frequency noise. In a similar way, but for the phasemeter in the slave satellite, the expected beat note frequency noise spectra is given by

$$\tilde{z}_2^2 = \tilde{n}_1^2 \cdot \left| \frac{e^{-s\tau}}{1+H(s)} \right|^2 + \tilde{n}_2^2 \cdot \left| \frac{1}{1+H(s)} \right|^2. \quad (3.13)$$

The highest level of laser frequency noise during the mission occurs in the beat note acquisition stage. In this case, a pre-stabilized master laser ($\tilde{\nu}_{\text{stb}}$) is recombined with a free-running slave laser ($\tilde{\nu}_{\text{free}}$) under an unlocked ($H = 0$) transponder configuration. In this way, the noise spectra at the input of the phasemeter result in

$$\tilde{z}_1 = \tilde{z}_2 = \sqrt{\tilde{\nu}_{\text{stb}}^2 + \tilde{\nu}_{\text{free}}^2}. \quad (3.14)$$

Figure 21 shows the expected frequency noise spectra of beat notes for free-running and a pre-stabilized lasers as well as the expected noise spectra in a science transponder mode for \tilde{z}_1 and \tilde{z}_2 . Here a laser servo gain $H(s)$ with an integrator-type ($1/f$) shape and an unity-gain frequency at 10 kHz with $5 \mu\text{s}$ (200 kHz) of delay is considered. In the beat note acquisition stage, the laser frequency noise in the low frequency band is dominated by the free-running frequency noise of the slave laser. At a higher frequency band (above ≈ 1 Hz), the frequency fluctuations on the beat note are $\approx \sqrt{2} \nu_{\text{free}}$ since $\nu_{\text{free}} \approx \nu_{\text{std}}$, and both are uncorrelated. In science mode, the worst case occurs at the master phasemeter, and therefore this case will be considered for future simulations and hardware implementations in the digital signal synthesizer.

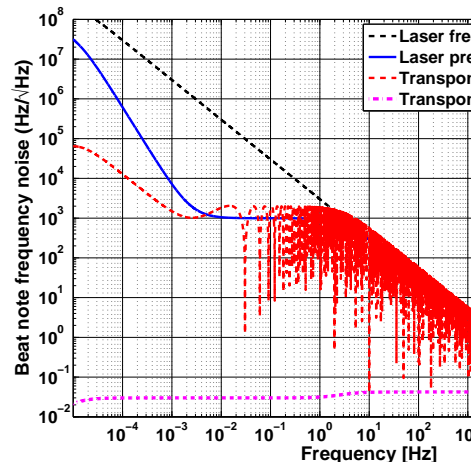


Figure 21: Expected laser frequency noise spectra in accordance to statement of work (SOW) of the ESA project: *LISA Metrology System*.

3.4.3 Beam misalignment

The precise orientation of the satellite with respect to the incoming laser is estimated by a differential wavefront sensing (DWS) technique. This technique uses the local oscillator as pointing reference and a quadrant photoreceiver as tilt sensors for measuring the incident angle of the incoming beam (see illustration in figure 22). Angular misalignments between the two beams result in a phase difference between QPD segments, but it also implies significant amplitude losses in the beat note level.

As shown in equation 3.2 and figure 23, the beat note amplitude depends on the heterodyne efficiency γ , which denotes the relative mismatch between the measurement beam wavefronts. For the science interferometer, satellite dynamics result in approximately 35% of losses in the heterodyne efficiency³.

The weak amplitude of the detected beat note requires a high gain factor in the photodiode preamplifier. As shown in the photocurrent equation 3.2, the DC term is dominated by the LO power, being some orders of magnitude higher than the AC

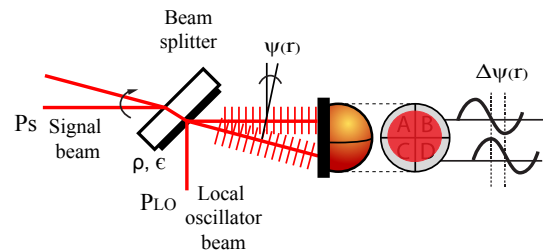


Figure 22: Principle of Differential Wavefront Sensing. Relative wavefront tilts can be inferred from separated phase readouts from different segments.

³ Obtained through IfoCad software simulations. The settings used to compute these values were described in G. Wanner's doctoral thesis; Complex optical systems in space: numerical modeling of the heterodyne interferometry of LISA Pathfinder and LISA

term. To maximize the amplification of the beat note, both terms AC and DC are decoupled in order to avoid saturation in the amplifiers of the AC channel. To determine the equivalent amplitude losses in the AC channel, and therefore the input signal levels for the LMS breadboard, the beat note of equation 3.2 is converted to a rms voltage as

$$V_{\text{rms}}(t) = G_{\text{pd}} \cdot \frac{\eta}{N} \sqrt{P_{\text{LO}} P_s \gamma} \cdot \frac{1}{\sqrt{2}} \quad [\text{V}], \quad (3.15)$$

where $G_{\text{pd}} = 2.14 \times 10^5 \Omega$ is set as the overall gain of the transimpedance amplifier, which contains an amplification factor of $30 \times 10^3 \Omega$ given by the TIA resistor. Taking into account a load resistance of 50Ω , the rms value of the beat note amplitude is translated to electrical power (dBm) and represented in figure 23. The photodetector preamplifier provides a signal level of about -24 dBm with approximately 2 dB of amplitude losses for a received optical power of 200 pW. Thus, the variable gain controller has to compensate for these amplitude variations. Furthermore, an additional amplification stage must provide the appropriate amplitude level for the ADCs. Table 2 summarizes the optical power for each LISA interferometer as well as the design parameters of the photoreceiver in order to assess the input signal levels for a single segment of the metrology breadboard.

IFO type	Optical Power	LO optical Power	Absolute beam tilt	Beam tilt jitter	TIA Gain [Ω]	LMS (dBm) input signal
Science	220 pW	3.44 mW	$\pm 100 \mu\text{rad}$	$450 \frac{\text{nrad}}{\sqrt{\text{Hz}}}$	2.14×10^5	$-26 \leq P_{\text{bn}} \leq -24$
Test-Mass	$90 \mu\text{W}$	2.24 mW	$\pm 500 \mu\text{rad}$	$150 \frac{\text{nrad}}{\sqrt{\text{Hz}}}$	4.14×10^2	$-26 \leq P_{\text{bn}} \leq -24$
Reference	2.97 mW	3.74 mW	$\ll \pm 100 \mu\text{rad}$	$\ll 17 \frac{\text{nrad}}{\sqrt{\text{Hz}}}$	TBD	TBD
PAAM	6.14 mW	3.49 mW	$\pm 500 \mu\text{rad}$	$17 \frac{\text{nrad}}{\sqrt{\text{Hz}}}$	TBD	TBD

Table 2: Optical and electrical power budget per segment for the metrology breadboard. Optical powers according to the ESA project: *Optical bench development for LISA*.

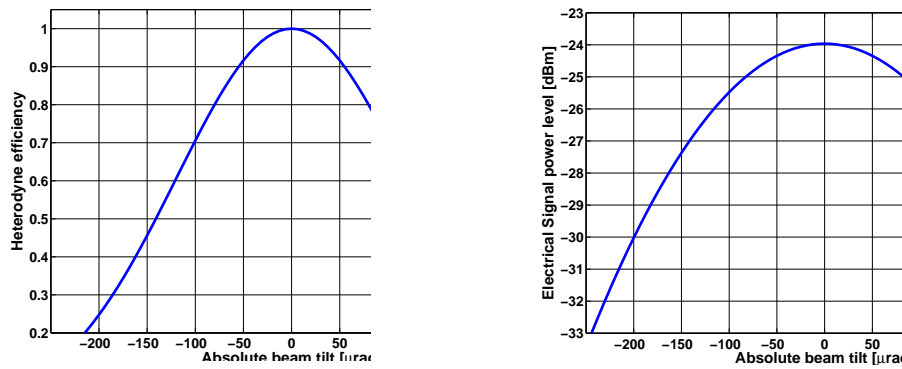


Figure 23: Heterodyne efficiency and electrical power budget in presence of absolute beam tilt errors.

3.4.4 Beat note acquisition

Star trackers are used for coarse satellite's orientation to the incoming laser beam. A laser acquisition sensor (CCD camera) assembled on the optical bench senses the incoming beam and compensates for small beam pointing deviations. Thus, the alignment of the incoming beam to the local optical bench is operated under four angular degrees of freedom, two from the transmitter satellite and two from the receiver satellite. These geometric acquisition stages ensure the incidence of the incoming laser beam on the science photoreceiver. A fifth degree of freedom is the beat note acquisition that consists mainly of the laser frequency offset between the local laser and the incoming laser. An adequate acquisition algorithm for this latter step will be implemented in the FPGA by combining the two following stages:

- A scanning algorithm that varies the optical frequency of the local laser by means of DACs connected to the piezo and temperature actuators.
- Simultaneously, the power spectrum of the electric signal corresponding to the measured photocurrent is continuously computed such as to detect a beat note as soon as it appears within the photoreceiver bandwidth.

To compute the signal spectrum for the full photoreceiver bandwidth, the most suitable technique is based on a Fast-Fourier Transform (FFT) algorithm. Although this technique requires a relatively high computational burden and FPGA resources, a FFT algorithm reduces significantly the computing time, and subsequently the beat note acquisition time. For example, assuming a 100% duty cycle and 2048 spectral points, a FPGA running at a sampling frequency of 50 MHz (20 ns) will process a complete spectrum estimation in the microsecond range ($20 \text{ ns} \times 2048 \approx 40 \mu\text{s}$), such that each output bin has a width of 25 kHz. At this measurement rate, the inherent beat note

frequency variations are given by the spectral linewidth of the incoming laser beam (typically ≈ 1 kHz for NPRO lasers), and therefore within one bin. The frequency information (bin numbers) is then used to initialize the phasemeter to help it to acquire lock.

Once the beat note has been acquired, DWS is used for highly precise interferometric laser pointing and satellite attitude control.

3.5 ADC NOISE

Digitization is a nonlinear process where an analog signal is rounded to the nearest digital value. The error between the real signal value and the quantized digital value is called quantization noise. This noise is typically evaluated in terms of the least significant bit (LSB), voltage resolution

$$V_{\text{LSB}} = \frac{1}{2^B} V_{\text{max}} \quad [\text{V}] , \quad (3.16)$$

where V_{max} is the full dynamic range of the ADC, and B is the number of bits. As shown in appendix D.1, the linear spectral density (LSD) of the quantization noise is given by

$$\tilde{V}_{\text{adc}}(f) = \frac{V_{\text{max}}}{2^B \sqrt{6 \cdot f_{\text{sampl}}}} \quad [\text{V}/\sqrt{\text{Hz}}] , \quad (3.17)$$

where f_{sampl} is the sampling frequency of the ADC. Assuming a normalized full analog input range $V_{\text{max}} = 1$, and an input rms input signal voltage of $\frac{A}{2\sqrt{2}}$, the resulting phase noise LSD yields

$$\tilde{\vartheta}_{\text{adc}}(f) = \frac{2\sqrt{2}}{A 2^B \sqrt{6 \cdot f_{\text{sampl}}}} = 40 \frac{\text{nrad}}{\sqrt{\text{Hz}}} \cdot \frac{1}{A} \rightarrow 0.007 \frac{\text{pm}}{\sqrt{\text{Hz}}} \cdot \frac{1}{A} . \quad (3.18)$$

Assuming a 12 bit resolution at 50 MHz of sampling rate, the quantization noise can be considered negligible in the design. The dominant noise source in ADCs is then given by clock jitter. For an optical wavelength of 1064 nm, and a desired pathlength sensitivity of $1 \text{ pm}/\sqrt{\text{Hz}}$ in the mHz band over a beat note oscillating at 20 MHz, the required timing errors $\delta\tilde{t}$ exceed the performance of space-qualified ADCs.

$$\tilde{\vartheta}_{\text{jitter}}(f) = f_{\text{het}} \cdot \delta\tilde{t} \quad \left[\text{cycles}/\sqrt{\text{Hz}} \right] , \quad (3.19)$$

$$\delta\tilde{t} < \frac{1 \text{ pm}/\sqrt{\text{Hz}}}{20 \text{ MHz}} \frac{1 \text{ cycle}}{1064 \text{ nm}} \approx 50 \text{ fs}/\sqrt{\text{Hz}} .$$

Timing errors between the three clocks on each spacecraft are measured by the sideband modulation scheme riding on the laser links (see chapter 4). However, errors in the ADC sampling latency between different channels of the same phasemeter cannot be subtracted with this technique. A method based on a pilot tone calibration has been investigated in both the Jet Propulsion Laboratory (JPL) and at the Albert Einstein Institute (AEI) for active ADC jitter correction. It consists in adding a stable reference tone at a fixed frequency at the input of each ADC. By injecting the pilot tone with a high frequency, the measured phase noise with an additional phasemeter is mainly attributed to ADC time jitter. A single pilot tone is added to all ADC channels of a LISA metrology breadboard, such that after applying an appropriate calibration factor, the phase jitter in the science measurements can be effectively subtracted through the phase measurements of the pilot tone. The phase errors induced by timing variations in two ADCs are described as

$$\begin{aligned}
 \Delta\vartheta_{\text{het}1}(f) &= f_{\text{het}1} \cdot [\Delta t + \varepsilon_1 + \theta_{h1}] && \text{[cycles]}, \\
 \Delta\vartheta_p(f) &= f_p \cdot [\Delta t + \varepsilon_1 + \varphi_{p1}], \\
 \\
 \Delta\vartheta_{\text{het}2}(f) &= f_{\text{het}2} \cdot [\Delta t + \varepsilon_2 + \theta_{h2}], \\
 \Delta\vartheta_p(f) &= f_p \cdot [\Delta t + \varepsilon_2 + \varphi_{p2}],
 \end{aligned} \tag{3.20}$$

where the sub-index ($i = 1,2$) denotes the number of the ADC channel. Δt is the sampling interval. ε is ADC aperture jitter. θ_{hi} and φ_{pi} are residual timing errors (e.g., either due to pathlength mismatches or cross talk) in the heterodyne signal and the pilot tone respectively. Although different linear combinations can be formed concluding in similar results, in this example for simplicity the two ADC channels are assumed at the same heterodyne frequency ($f_{\text{het}1} = f_{\text{het}2} = f_{\text{het}}$), and the respective pilot tones are subtracted from the heterodyne signals after scaling them with a calibration factor of f_{het}/f_p . The relevant information for LISA is the phase difference between two heterodyne signals. Thus, after calibration the resulting phase combinations yield to a residual phase error of

$$\Delta\vartheta_{\text{residual}}(f) = f_{\text{het}} \cdot [\theta_{h1} - \theta_{h2}] + f_{\text{het}} \cdot [\varphi_{p1} - \varphi_{p2}] \quad \text{[cycles]}, \tag{3.21}$$

Note that the ADC jitter ε is effectively removed from the science measurements, such that only residual timing errors of the input signal itself remain. Therefore, the pilot tone distribution along the metrology breadboard is a crucial part in the hardware design.

On the other hand, in the hardware implementation the pilot tone is directly added onto the incoming heterodyne signal. Consequently, the shot noise background is also

superimposed in the pilot signal. As described in appendix B.1, the phase error induced by shot noise depends on the SNR. Therefore the amplitude of the pilot tone should be designed with a relatively high magnitude. This reduces the coupling of extra shot noise into the science measurements in the calibration process.

3.6 LOW-DEPTH PHASE MODULATIONS FOR ADVANCED LASER LINK CAPABILITIES

The inter-satellite interferometry system dedicates a small portion of its available optical power to advanced laser link capabilities by applying two different low-depth phase modulations: a tone sideband modulation in the GHz regime with a 10% allocation of the optical power for clock noise removal, and a direct-sequence spread spectrum modulation (MHz) onto the main carrier with 1% allocation of the light power for ranging and data transfer.

3.6.1 High-frequency tone modulation for clock noise transfer

The modulation index is related to the fraction of total power that is allocated to an unmodulated carrier. Here, an analytical model for a tone sideband modulation is described in order to determine the required modulation index for transferring 10% of the optical power to the clock sidebands.

The optical field of a laser beam with a phase modulated $\phi(t)$ can be written as

$$E_s(t) = E_0 \cdot \exp(i\omega_s t + i\phi(t)), \quad (3.22)$$

If a tone sideband modulation with an angular frequency $\omega_m = 2\pi f_m$ and a modulation index m_{sb} (in radians) is applied, the resulting amplitude of a laser beam is

$$\begin{aligned} E_s(t) &= E_0 \cdot \exp(i\omega_s t + im_{sb} \cos \omega_m t) \\ &= E_0 \cdot \exp(i\omega_s t) \cdot \exp(im_{sb} \cos \omega_m t) \\ &= E_0 \cdot \exp(i\omega_s t) \cdot \left[J_0(m_{sb}) + \sum_{k=1}^{\infty} i^k J_k(m_{sb}) \left(\exp(ik\omega_m t) + \exp(-ik\omega_m t) \right) \right], \end{aligned} \quad (3.23)$$

where $J_k(m)$ denotes the Bessel functions of the first kind and order k . For small modulation index, the first terms of their Taylor series can be used to approximate the Bessel functions as follows:

$$\begin{aligned}
J_0(m_{sb}) &= 1 - \frac{m_{sb}^2}{4} \dots, \\
J_1(m_{sb}) &= \frac{m_{sb}}{2} - \frac{m_{sb}^3}{16} \dots, \\
J_2(m_{sb}) &= \frac{m_{sb}^2}{8} \dots, \\
&\vdots \\
J_k(m_{sb}) &= \frac{1}{k!} \left(\frac{m_{sb}}{2} \right)^k \dots,
\end{aligned} \tag{3.24}$$

Note that the only terms of the Bessel functions with a significant contribution in the optical amplitude of equation 3.24 are J_0 and J_1 . Under this approximation⁴, the signal is described by

$$E_s(t) \approx E_0 \cdot \exp(i\omega_s t) \times \left[J_0(m_{sb}) + iJ_1(m_{sb}) \cdot \exp(i\omega_m t) + iJ_1(m_{sb}) \cdot \exp(-i\omega_m t) \right], \tag{3.25}$$

From the first term in 3.25, one may notice that this type of modulation comprises the original optical carrier, $E_0 J_0(m_{sb}) \cdot \exp(i\omega_s t)$, plus two sidebands, i.e., the upper and the lower sidebands $iE_0 J_1(m_{sb}) \cdot \exp(i\omega_s t \pm i\omega_m t)$ which are oscillating at $\omega_s + \omega_m$ and $\omega_s - \omega_m$ respectively, and with a relative phase shift of $\pm i = \pm\pi/2$ radians against the main carrier. The amplitude of the carrier is then proportional to $J_0(m_{sb})$ and the amplitude of each sideband is proportional to $J_1(m_{sb})$, whereas their relative average power is described by the square of the Bessel function $|E_0 \cdot J_k(m_{sb})|^2$. Figure 24 shows the relative optical power of the main carrier and the first two sidebands as a function of the phase modulation depth. Here, it is shown that for low-depth phase modulation ($m_{sb} < 1$) the optical power transferred to the second pair of sidebands $J_2^2(m_{sb})$ is negligible with respect to the main carrier $J_0^2(m_{sb})$ and the first pair of sidebands $J_1^2(m_{sb})$. For a relative sideband power of 10% of the main optical carrier $1 - J_0^2(m_{sb}) = 0.1$, a modulation index of $m_{sb} \approx 0.45$ rad is needed⁵.

3.6.2 Spread spectrum modulation for ranging and data transfer

In the case of laser ranging, a DS/SS modulation scheme has been implemented. It conveys data by merging them with a pseudo-random noise (PRN) signal and

⁴ Actually, this type of modulation produces an infinite number of sidebands, $\omega_0 \pm 2\omega_m$, etc. However in practice their amplitudes are negligible.

⁵ By driving a modulation depth of about 2.4 rad, almost the entire carrier power is transferred to the sidebands.

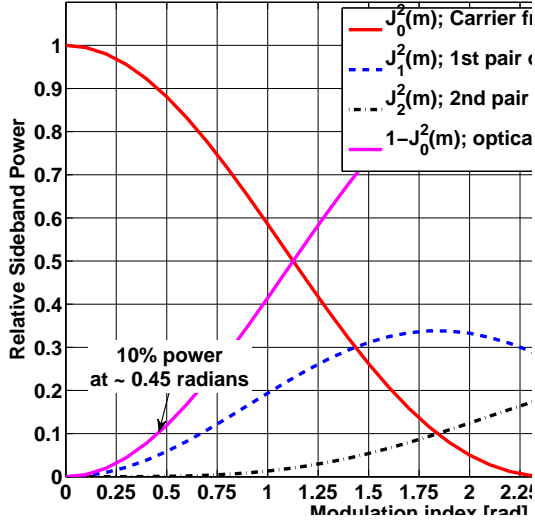


Figure 24: Relative optical powers versus modulation indices for clock noise transfer. The square of the Bessel function $J_0^2(m_{sb})$ denotes the optical power of the main carrier, $J_1^2(m_{sb})$ denotes the optical power of the first pair of sidebands, and $J_2^2(m_{sb})$ the power in the second pairs of sideband. For small modulation indices $m_{sb} < 1$, the optical power given by $J_2^2(m_{sb})$ can be assumed negligible. The modulation index that corresponds to 10% of the optical power can be computed from the fraction of the total power invested in the first pair of sidebands, which is given by $1 - J_0^2(m_{sb})$.

afterwards modulating both onto a laser carrier via a binary phase-shift keying (BPSK) scheme. The received beat signal at the output of the science photodetector can be written as

$$\begin{aligned}
 P_{\text{seg}}(t) &= \sqrt{\frac{\gamma P_{\text{LO}} P_s}{P_{\text{total}}}} \cdot \sin \left(\omega_{\text{het}} t + m_{\text{prn}} \sum_{n=-\infty}^{\infty} c_n p(t - nT_c) \right) + n(t) \quad [\text{W}] \\
 &= \sqrt{\frac{\gamma P_{\text{LO}} P_s \cos^2(m_{\text{prn}})}{P_{\text{carrier}}}} \cdot \sin(\omega_{\text{het}} t) + \\
 &\quad \sqrt{\frac{\gamma P_{\text{LO}} P_s \sin^2(m_{\text{prn}})}{P_{\text{modulation}}}} \times \sum_{n=-\infty}^{\infty} c_n p(t - nT_c) \cdot \cos(\omega_{\text{het}} t) + n(t). \quad (3.26)
 \end{aligned}$$

where the phase of the beat note ϕ was replaced by a binary PRN-data sequence c_n running at several kilobits per seconds with a pulse shape given by $p(t)$ of period $1/T_c$ and oscillating in the MHz range with a modulation index of m_{prn} . $n(t)$ denotes additive noise at the output of the TIA, which is dominated by shot noise as described in this chapter. By using trigonometry, it is possible to rearrange the first equation into

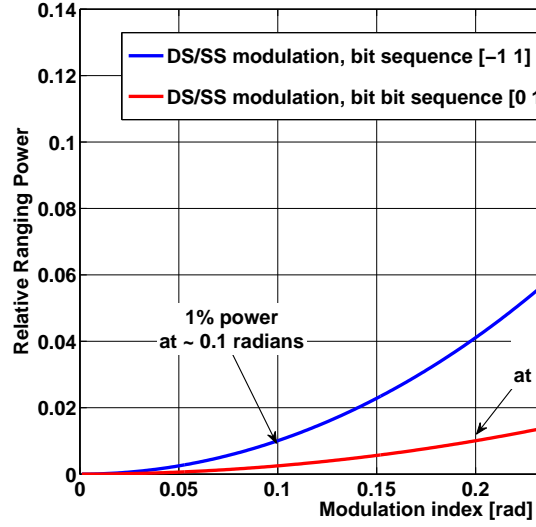


Figure 25: Modulation index for ranging and related ranging power.

the second one. Here, the fraction of the power allocated to the discrete carrier becomes $P_{\text{carrier}} = P_{\text{total}} \cdot \cos^2(m_{\text{prn}})$ with the remaining fractional power $P_{\text{modulation}} = P_{\text{total}} \cdot \sin^2(m_{\text{prn}})$ available for PRN modulation. The code bit sequences can be either $[-1, 1]$ such that the modulation index can be derived from the following equation

$$\frac{P_{\text{modulation}}}{P_{\text{carrier}}} = \frac{\sin^2(m_{\text{prn}})}{\cos^2(m_{\text{prn}})} = \tan^2(m_{\text{prn}}) \quad (\text{for bit values } [-1, 1]). \quad (3.27)$$

For FPGA implementation, it is optimal to apply a modulation index with digital values of $[0, 1]$, such that the modulation index yields

$$\frac{P_{\text{modulation}}}{P_{\text{carrier}}} = \tan^2\left(\frac{m_{\text{prn}}}{2}\right) \quad (\text{for bit values } [0, 1]). \quad (3.28)$$

The equivalent phase fluctuations correspond to $[-0.1, 0.1]$ and $[0, 0.2]$ radians respectively, as denoted in figure 25. Although the amplitude variations in both cases are equal, in laboratory conditions, it might be preferable to modulate the EOM with phase fluctuations between 0 to 0.2 radians, since it can be encoded using only one bit, i.e., a single digital pin in the breadboard. Afterwards, in the demodulation process, the carrier-tracking loop (described in chapter 4) only detects the magnitude of the phase variations, being thus independent of the previous modulation values.

3.7 DOPPLER SHIFT

Separate phasemeter channels track the Doppler-shifted carrier and the clock sidebands. The Doppler shift of an electromagnetic wave is given approximately by

$$f_{R_x} \approx f_{T_x} \left(1 + \frac{v_{\text{LOS}}}{c} \right) \quad [\text{Hz}], \quad (3.29)$$

where f_{T_x} is the transmitted frequency, f_{R_x} is the received frequency, v_{LOS} is the inter-satellite line-of-sight (LOS) velocity, and c is the speed of light. In terms of the Doppler shift $f_D = f_{R_x} - f_{T_x}$, the previous equation can be expressed as

$$f_D \approx f_{T_x} \left(\frac{v_{\text{LOS}}}{c} \right) \quad [\text{Hz}], \quad (3.30)$$

where

$$f_{T_x} \equiv \begin{cases} \nu_c, & \text{optical frequency of the main carrier} \\ \nu_c + f_{\text{mod}}, & \text{optical frequency of the upper sideband} \\ \nu_c - f_{\text{mod}}, & \text{optical frequency of the lower sideband} \end{cases} \quad (3.31)$$

Given a maximum inter-satellite velocity of $v_{\text{LOS}} = 20 \text{ m/s}$, and a tone modulation of $f_{\text{mod}} \approx 2 \text{ GHz}$, the resulting Doppler shift amounts to a frequency variation of up to $\pm 20 \text{ MHz}$ in the optical carrier and both sidebands plus $\pm 133 \text{ Hz}$ of Doppler difference between the carrier and the sidebands. Thereby, the Doppler shifts affect differently the carrier and the sidebands, and consequently it has to be taken into account in the design of the clock demodulation scheme in the phase measurement system.

On the other hand, equation 3.30 can be written as a function of the wavelength of the transmitted carrier $\lambda_{T_x} = c/f_{T_x}$ such that

$$v_{\text{LOS}} \approx \lambda_{T_x} f_D, \quad (3.32)$$

Note that from the previous equation one may estimate the average LOS velocity by measuring the Doppler frequency with a phase measurement system, i.e., by counting the Doppler cycles obtained from the carrier phase tracking over a short period of time, and then scaling by the nominal optical wavelength. Moreover, by integrating the velocity it is possible to estimate the change of range relative to the start of the integration with high precision. However, this measurement is ambiguous since it contains no information regarding the number of full cycles in the total distance. Laser ranging will resolve this ambiguity.

3.8 OPTICAL MEASUREMENT OF GRAVITATIONAL WAVE EFFECT

Although a gravitational wave (GW) transports a huge amount of energy, its effect in the curvature of the space-time is extremely weak. Only a few number of interferometers in the world provide enough sensitivity to detect the tiny phase variations that couples onto their laser links when a GW signal passes. These detectors will likely achieve soon the first direct measurements of GW signals. Here, the effect of a GW is only considered based on its expected phase shift induced on an optical link. The development of a digital signal generator is ongoing in order to simulate the optical phase shift effect of GWs to validate the metrology system.

Assuming a perfectly polarized GW signal with angular frequency ω_{gw} and amplitude h traveling perpendicularly to the interferometer plane, its induced phase shift onto a laser beam can be written as [51]

$$\delta\phi_{\text{gw}} \approx h \frac{\omega_c \sin(\omega_{\text{gw}}L/c)}{\omega_{\text{gw}}} \cdot \cos[\omega_{\text{gw}}(t - L/c)] \quad [\text{rad}],$$

$$\text{with } \left(\sin(\omega_{\text{gw}}L/c) \approx \omega_{\text{gw}}L/c \right) \quad \text{in the mHz band} \quad (3.33)$$

$$\approx h \frac{\omega_c L}{c} \cdot \cos[\omega_{\text{gw}}(t - L/c)],$$

where ω_c is the laser beam frequency. Thus the expected phase variations induced by a GW signal are mainly determined by the interferometric arm-length ($L = 5 \times 10^9 \text{ m}$) and the strain of the signal ($h \approx 10^{-21}$) and results in a magnitude of approximately 3×10^{-5} radians.

3.9 SUMMARY

The LISA metrology system (LMS) is based on a laser transponder configuration with a heterodyne detection scheme. Each component in the measurement chain is designed to provide a sensitivity with an allocated phase noise budget of microcycles. The design sensitivity will be ultimately dominated by shot noise for beat note frequencies above 5 MHz and laser intensity noise for lower frequencies.

One of the major challenge for the LISA mission is to measure phase shifts induced by gravitational waves in the presence of Doppler shifts, and in presence of two important noise sources: the laser frequency noise and phase noise between the on-board reference clocks. LISA will use a technique called time delay interferometry (TDI) to suppress

both noise contributions, while preserving the gravitational wave signal. To achieve the desired suppression, the TDI algorithm needs measurements of the differential clock noise between any two spacecraft and inter-spacecraft ranging measurements. These measurements are accomplished by applying two different phase modulations to the laser link: a high-frequency (GHz) sideband modulation using 10% of the available optical power and a PRN modulation using 1% of the optical power. As shown in this chapter, the equivalent modulation indices are ≈ 0.45 rad for clock noise transfer and ≈ 0.1 rad for laser ranging. The demodulation process on the LMS will be described in the following chapters.

Part II

LASER RANGING AND DATA COMMUNICATIONS

The Laser Interferometer Space Antenna (LISA) mission requires an inter-spacecraft laser ranging scheme with meter accuracy to reduce the effect of laser frequency noise using time-delay interferometry (TDI). This chapter describes the hardware development of a laser ranging scheme based on a Direct Sequence Spread Spectrum (DS/SS) modulation. Important benefits can be simultaneously accomplished by applying such a scheme. First, it allows both range and clock synchronization to be continuously measured from the inter-satellite laser links. Second, it enables encoded information to be transmitted with the ranging signal for data communication. Third, it provides significant noise reduction against spurious interfering signals, and therefore, it allows the implementation of bidirectional ranging and full-duplex optical data transfer. Finally, it can be implemented using only a small fraction of the total laser power. Thus, this scheme can be integrated into precision heterodyne interferometers for gravitational wave detection without performance degradation in the stability of the carrier phase science measurements.

In contrast to on-ground gravitational wave detectors, orbital dynamics of the LISA constellation result in an unequal and time-varying arm-length mismatch, such that the laser frequency noise becomes a limiting factor [17, 50]. This effect is addressed in the following section 4.1, and motivates the realization of a coherent laser ranging scheme applied to highly precise space-based gravitational wave interferometers. Section 4.2 presents an overview of the proposed optical metrology system based on a simplified scheme of a single LISA arm. Section 4.3 describes the relevant modifications of the ranging architecture applied to LISA with respect to conventional DS/SS schemes. Section 4.4 shows the design of the ranging signal in terms of its correlation properties. In addition, the auto-correlation background noise resulting from different sources of ranging errors was analyzed, including noise sources such as inter-code interference, additive Gaussian noise and the encoding of data bits for optical communication. Section 4.5 describes a model of the interferometric signal at the output of the photoreceivers. The receiver architecture is presented in section 4.6. Here, the two digital feedbacks controls loops required for implementing the laser ranging scheme are characterized, i.e., a phase-lock loop (PLL) architecture for interferometric phase measurements and a delay-locked loop architecture for ranging measurements. Section 4.7 presents the custom-designed hardware specifically development for testing the phasemeter and ranging performance with realistic LISA-like signals. Section 4.8 presents the first experimental validation of the ranging technique using an electric

signal modeling of the expected interferometer output. The optical part in the ranging scheme was substituted by a digital signal synthesizer (DSS), which mimics the signal structure at the output of the science photoreceivers. The ranging performance was evaluated achieving sub-meter accuracies and data communication at 24 kbps. Moreover, the DSS supports investigations on preliminary phasemeter performance at picometer levels in the mHz frequency band, which is extremely difficult to achieve in optical laboratory conditions due to e.g., thermal noise, and tiny optical displacements. The phasemeter performance was evaluated in an electrical environment, and using the DSS. Results show that the proposed DS/SS modulation scheme can be used in the metrology system without interferometric performance degradation. In addition, a second modulation scheme based on clock noise transfer is implemented in the LISA metrology system to reduce the clock phase noise coupled within the science measurements. To this end, on-board clock signals will be transmitted and accurately measured on the remote satellite [52, 53, 54]. Using the DSS, the phase noise requirement of the clock sideband signals has been demonstrated, validating the architecture to achieve an equivalent timing stability of $50 \text{ fs}/\sqrt{\text{Hz}}$ in the mHz band.

4.1 STATEMENT OF THE PROBLEM: UNEQUAL ARM LENGTH INTERFEROMETER

The phase sensitivity of an interferometer (e.g., Michelson-like interferometer) with an arm-length mismatch ΔL is limited by fluctuations in the laser frequency given by

$$\delta\tilde{\phi} = \frac{2\pi}{c} \Delta L \delta\tilde{\nu} \quad [\text{rad}/\sqrt{\text{Hz}}], \quad (4.1)$$

where c is speed of light.

In order to achieve the LISA strain sensitivity goal of $10^{-22}/\sqrt{\text{Hz}}$, the inter-satellite links will be continuously monitored with picometer accuracy through precise measurements of the optical carrier phases to a level better than $\delta\tilde{\phi} \approx 2\pi \times 10^{-6} \text{ rad}/\sqrt{\text{Hz}}$. Orbital dynamics cause distance variations between the spacecraft with a maximum mismatch of $\Delta L \approx 1 \times 10^8 \text{ m}$. This unequal arm-length configuration combined with a typical free running Nd:YAG NPRO laser frequency noise of $\delta\tilde{\nu} \approx 3 \text{ MHz}/\sqrt{\text{Hz}}$ at 3 mHz would result in a phase noise of $\delta\tilde{\phi} \approx 2\pi \times 10^6 \text{ rad}/\sqrt{\text{Hz}}$, i.e., twelve orders of magnitude above the required for LISA. In order to achieve the required phase sensitivity [50], an initial laser pre-stabilization will reduce the free running frequency noise [50] (see section 3.4.2). A second technique will measure the arm-length mismatch in order to synthesize an equal arm-length interferometer by post-processing on ground [50, 21, 55]. This post-processing technique is called time-delay interferometry (TDI) [20, 54] and requires knowledge of both the acquisition time of each phase measurement and the absolute distance between the spacecraft with one meter accuracy. With a laser pre-stabilization of hundreds of $\text{Hz}/\sqrt{\text{Hz}}$ in the millihertz band, and a ranging accuracy in

the order of one meter, the TDI algorithm will suppress the residual laser frequency to provide the desired LISA sensitivity. However, a ranging accuracy of meters is beyond the performance of the most advanced positioning techniques on-ground for deep space missions, and therefore, precise measurements on-board each spacecraft need to be obtained as auxiliary functions of the laser links. A laser ranging system based on an optical Direct Sequence Spread Spectrum (DS/SS) modulation is the foreseen technology to be incorporated into the precise inter-satellite interferometry system. Through such an integration, the metrology system will provide both relative measurements at picometer accuracy and absolute ranging measurements at sub-meter accuracy.

4.2 SYSTEM DESCRIPTION OVERVIEW

A simplified schematic of the optical metrology system for a single LISA arm is shown in figure 26. Two satellites separated by five million kilometers shield two free floating test masses from external disturbances. The test masses serve as inertial reference points of an inter-satellite interferometry system. Local interferometers monitor position and orientation of each test mass with respect to their respective optical benches [56]. In order to monitor relative displacements between optical benches, two laser beams with a transmitted light power of 2 W are exchanged between satellites. Due to diffraction losses of the beam after the long propagation and additional optical losses on the bench, only around 100 pW are detected at the remote spacecraft [17, 57]. The weak beam received is directly brought to interference with a local laser on the optical bench, thus providing a heterodyne beat note at their frequency difference. The phase of the resulting beat note is then measured with respect to its on-board clock in a phase measurement system (PMS), and used as control signal to return the local laser as a high power phase replica of the incoming beam. Note that this allows to operate the laser link as an optical transponder, receiving a master (incoming) laser and transmitting a slave (outgoing/local) laser. In LISA, the Doppler shifts produced by orbital motion of the spacecraft (relative velocity up to ± 20 m/s) lead to the beat notes in the range between 2 to 20 MHz. In order to achieve the required phase sensitivity, $\delta\tilde{\varphi} \simeq 1 \times 10^{-6}$ cycle/ $\sqrt{\text{Hz}}$ for a beat note up to 20 MHz, the necessary clock timing jitter would be approximately $\delta\tilde{t} \leq \delta\tilde{\varphi}/20 \text{ MHz} \simeq 50 \text{ fs}/\sqrt{\text{Hz}}$. This timing stability is beyond the performance of the most stable clocks available in space-based applications. Consequently the optical metrology system requires a clock noise removal scheme to subtract the excess phase noise that couples into the science measurements. To this end, each spacecraft clock is multiplied by an integer factor to GHz frequencies and phase modulated onto the laser links using 10% of the light power. This way, the clock jitter is intentionally amplified in the resulting sideband-to-sideband beat note such that its phase noise performance can be relaxed. For example, for clock sidebands at 2 GHz, the phase readout requirement can be relaxed by a factor of $2 \text{ GHz}/20 \text{ MHz} = 100$. Finally,

the phase measurements of the sideband beat notes on each satellite are transmitted to ground to be processed by TDI for clock noise removal [21].

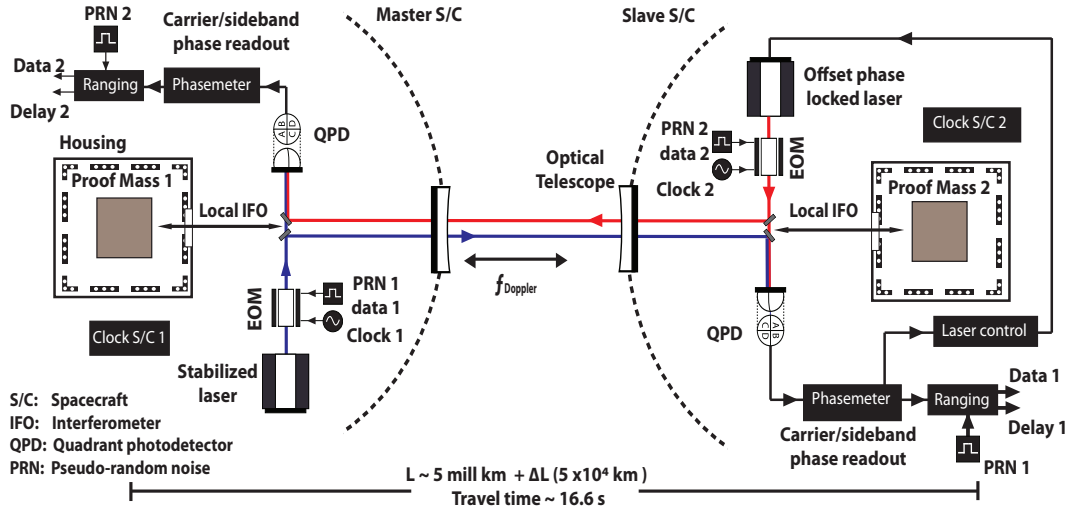


Figure 26: Simplified diagram of the optical metrology system for an interferometric arm in LISA. The metrology system with data communication capability provides measurements of the relative path length displacements between two free-floating test masses, inter-satellite clock jitter and the absolute arm length distance. On each satellite, the on board clock and pseudo-random noise (PRN) sequences encoded with data information are phase modulated onto a laser using an electro-optic modulator (EOM). Both lasers, labeled as master and slave, are exchanged between satellites and offset phase locked to generate the heterodyne beat signals. Each satellite measures the phase of their resulting beat signals in the phase measurement system (PMS), which is also used for PRN demodulation to perform ranging and data transfer.

In order to reduce the effect of laser frequency noise in the science phase measurement, TDI requires a measurement of the absolute inter-satellite distance, which is obtained from the laser transit time along a LISA arm with 3 ns ($\approx 1 \text{ m}$) accuracy. An indirect method to compute the signal transit time can be obtained from the phasemeter measurements by differencing the carrier phase measurements of the incoming beat note with respect to the initial phase at the instant of the measurement. This provides a precise relative ranging measurement as a fractional part of an optical wavelength, and therefore with an ambiguity range of one cycle, $\lambda = 1064 \text{ nm}$. By counting the number

of measured carrier cycles in the phasemeter over a period of time, the relative motion between satellites can be estimated as

$$\Delta\text{PR}(t) = \frac{\lambda}{2\pi} \times \left[\underbrace{\widehat{\phi}(t) - \phi(t - \tau)}_{\text{fractional part}} + \underbrace{N_{\text{cycles}}}_{\text{integer part}} \right] \text{ [m]}, \quad (4.2)$$

where $\widehat{\phi}(t)$ denotes the phase of the local oscillator in the PMS at time t . $\phi(t - \tau)$ is the phase of the incoming signal, which is delayed τ by the transit time. N_{cycles} is the numbers of full carrier cycles. In standard positioning systems such as GPS, this measurement is known as delta pseudo-ranges and provides an extremely precise estimation of the inter-satellite distance. Unfortunately, delta-pseudo ranges contains no information regarding the initial number of full cycles before phase locking, resulting in an ambiguous measurement. In order to resolve this ambiguity and to transmit data between satellites, an optical modulation based on a Direct-Sequence Spread Spectrum (DS/SS) scheme is applied on each laser link. To this end, a pseudo-random noise (PRN) sequence encoded with data is phase modulated using 1% of the light power before being transmitted to the remote spacecraft. After signal propagation along the LISA arm, the PRN modulation is recovered as phase transitions at the remote phasemeter output. A delay-locked loop (DLL) architecture is implemented for PRN tracking, absolute delay measurements and data demodulation. It aligns the local PRN reference to the incoming code by correlating both sequences, while the data modulation is directly decoded from the PRN sequences. This ranging scheme is identical for each of the six lasers in LISA and it provides six independent delay measurements referred to the three unsynchronized clocks. Thereby, a PRN is generated and transmitted at a known rate in accordance with its on-board clock, and subsequently encoding the PRN transmission time $t_{\text{tx}}(t)$ onto the laser phase at precise time stamps (3 ns given by its ranging accuracy). The received PRN signal at the remote satellite is then decoded and tracked at a later time based on a different clock, thus providing the time of reception $t_{\text{rx}}(t)$. The corresponding range can be therefore computed as the apparent signal propagation delay scaled by the speed of light

$$\text{PR}(t) = c \times [t_{\text{rx}}(t) - t_{\text{tx}}(t - \tau)] = D + c \delta t \text{ [m]}, \quad (4.3)$$

where D is the absolute inter-satellite distance and δt is the clock bias. This distance measurement is often called pseudo-range $\text{PR}(t)$ given that clock differences between satellites are coupled as ranging errors. In order to improve this pseudo-range measurements, both clock noise measurements from the sideband beat notes and ranging measurements from the carrier Doppler estimations will be combined on-ground by data analysis techniques. In addition, orbital information gained from on-ground based

estimations and solar system dynamics will also be combined in an optimal filter for effective noise suppression in the pseudo-range measurements. The development of such a filter is being currently conducted at the AEI, and addressed in [22]. The output of the filter (e.g. Kalman-like filtering) will provide a set of TDI variables to form time-delayed linear combinations of phase measurements for laser frequency noise suppression [58]. The focus of this thesis is, however, the process of how the ranging measurements are obtained, and the achievable ranging accuracy of the resulting raw measurements in the on-board laser metrology system.

4.3 SPREAD SPECTRUM MODULATION

A Spread Spectrum modulation is a communication technique in which the transmitted bandwidth used to send a signal occupies a higher bandwidth than the minimum necessary to transmit the information. To do so, a pseudo-random noise (PRN) code formed by a sequence of bipolar bits, +1 and -1, is added as modulo-two with a lower data rate signal and then used to phase-modulate the optical carrier. This process is called the spreading operation. Although the spreading signal appears to be random, the codes are in fact perfectly deterministic with a given length, and with repetition periods at precise epoch times, as well as known by both the transmitter and the receiver. Among the major advantages of this type of modulation is the capability of measuring the propagation time from the transmitter to the receiver by time alignment of PRN sequences, thus allowing an absolute distance estimation between both stations. The spread spectrum implementation used here modulates the data-encoded PRN sequences into the phase of a laser carrier using a Binary Phase Shift Keying (BPSK) scheme. In contrast to other modulation schemes such as quadrature phase-shift keying (QPSK), the BPSK scheme uses only two stages (2 phase transitions) which are proportional to the modulation depth. It increases the energy per bit transmitted given that it uses the minimum transition states for the same available energy. This way, the BPSK scheme reduces the probability of bit errors in the code transmission, which is crucial for weak-light environments (see optical experimental results in chapter 5).

In contrast to other satellite-based PRN ranging systems such as the Navigation Satellite Timing and Ranging Global Positioning System (NAVSTAR GPS) [59] operating in the radio band with a high modulation index that fully suppresses the carrier, the proposed architecture for LISA modulates the phase of an optical carrier at a low-depth modulation index (0.1 rad, described in chapter 3, section 3.6.2). This reduces both the optical power allocated to the PRN modulation and the residual carrier phase noise induced by fast PRN transitions. Thus, this ranging scheme uses only 1% of the available optical power to achieve sub-meter accuracy over a 5 million km inter-satellite distance while the rest of the optical power remains in the carrier and is used for precise interferometry. This yields to a ranging system operating at 1 pW

power levels out of the 100 pW of total incident power at the remote photoreceiver. Thereby this technique exploits one of the major advantages of DS/SS modulations, i.e., the capability of supporting ultra-low light power levels given its robustness against strong noise sources. In addition, this technique provides a significant reduction in the susceptibility to interferences between signals that share the same channel and the same frequency band. This feature is important given the transponder configuration in LISA because each photoreceiver is receiving two ranging signals, one from the local oscillator and the other from the incoming laser of the remote satellite. An important benefit of this transponder configuration is the unidirectional single-beam propagation. Laser transponders only have $1/D^2$ signal loss compared to $1/D^4$ for passive ranging (transmission and reflection). Therefore, this reduces the required laser power and enables measurements over larger distances as well as it enables bidirectional ranging measurements and a full-duplex data communication scheme. Another difference of this scheme with respect to the standard receivers is a significant improvement in the data transmission rate. The proposed architecture supports optical communications at ≈ 24 kbps against the 50 bps data stream modulated onto the conventional GPS signal.

4.4 CODE-CORRELATION PROPERTIES

In the LISA topology, each laser is phase modulated by applying a low-depth BPSK-DS/SS scheme for bidirectional ranging and data communication. Each satellite carries two local lasers, resulting in a total of six laser beams, which are exchanged between the three satellites. Therefore, a family of six orthogonal PRN codes is foreseen for the mission. Given the laser transponder configuration, each local laser simultaneously provides a beam for local interferometry and transmits a beam for an inter-spacecraft link, resulting in a beat note with two codes modulated onto its phase. The main design driver for the code is that after the interference between any two given lasers, a single PRN code can be tracked without suffering significant mutual interference from other pseudo-sequences. Hence, a fundamental issue in the ranging performance is the optimization of the correlation properties of the six codes. As shown in figure 27, for the designed pseudocodes in LISA, their respective auto-correlation presents a peak at zero delay and almost vanishing autocorrelation for other delays. This peak serves as delay detector and as a time-stamp if the start of the PRN is synchronized with the clock of the remote spacecraft. Additionally, a negligible cross-correlation is desirable since it reduces the inter-code interference noise modulated on the local laser.

Figure 28 shows a comparison of the auto-correlation function of a LISA-like pseudo-code with respect to a standard Gold code employed in GPS [60, 61]. The main difference between the proposed LISA and GPS codes are the designed code length. The Gold codes are generated by Linear Feedback Shift Register (LFSR) circuits. This way, the bit in the tapped stages are combined following a characteristic polynomial of order m and the results are fed back to the first stage of the register on the next shift. The maximum

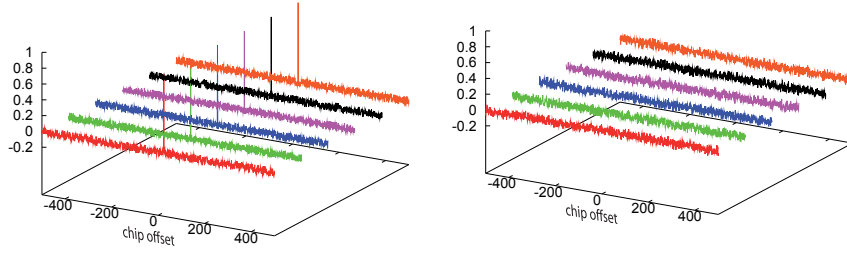


Figure 27: Auto-correlation (left) and cross-correlation (right) between a family of six different PRN combinations designed for LISA.

length pattern that can be generated by the LFSR with a m -stage shift register is $2^m - 1$, yielding to an odd code length. In the case of the Coarse/Acquisition (C/A) codes developed for the GPS systems, the code-length is $M = 1023$ chips ($m=10$), which generates an auto-correlation function with four amplitude levels [60] given by

$$\begin{cases} 1 - |\tau| \left[1 - \frac{1}{M} \right], & \text{for } \tau \leq 1 \\ \frac{2^{(m+2)/2} - 1}{M}, \quad \frac{-1}{M} \quad \text{or} \quad \frac{2^{(m+2)/2} + 1}{M}, & \text{for } \pm 2, \dots, \pm [M - 1], \end{cases} \quad (4.4)$$

where τ is the lag value in units of code chips. In LISA, the pseudo-codes were specifically designed by numerical optimization to enhance their correlation properties, using a C-program and developed by G. Heinzel [62]. As shown in figure 28, the peak-to-peak amplitude of the background noise in the auto-correlation function of the LISA code is lower than the GPS code. Figure 29 shows the auto-correlation noise after interference between the incoming and outgoing codes, as well as its resulting interfering time series. Note that after interference the designed code for LISA provides a low auto-correlation background noise. An additional design driver for the LISA pseudocodes is the development of an orthogonal family of six codes all with an even length of 1024 chips. This even length reduces the FPGA computation burden, enabling integer sub-divisions in modulo-2 arithmetic of the PRN sequences into several data periods. For each data period the sign of the code auto-correlation is constant, while it is inverted for a different data bit. Adding the absolute value of the correlation of each data period over a full code-length, the correlation function is recovered by code acquisition and tracking. By applying this method of data de-encoding, the ranging signal increases its data rate capability to a several kbps without an excessive reduction in the code tracking performance of the system ¹.

¹ In GPS the data rate is 50bps over a PRN sequence of 1023 chips running at 1 MHz. This implies that one period of data involves several PRN periods. In LISA the data rate requirement is about 15 kbps of 1024

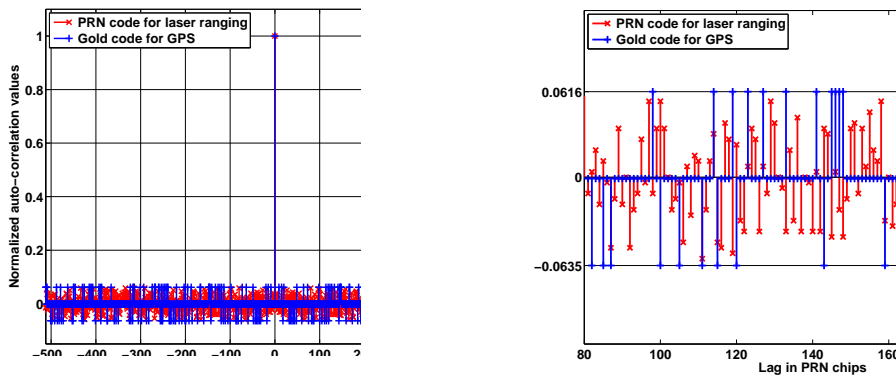


Figure 28: Left side: comparison of the auto-correlation function between a Gold pseudo-code used in GPS systems and a pseudo-code used in laser ranging for LISA. Right side: it shows a zoom in the auto-correlation background noise.

Figure 30 shows the auto-correlation background noise due to different data rates. In ideal auto-correlation conditions, i.e, without another sources of ranging errors, the maximum data rate allowed for the detection of a correlation peak is about 300 kbps. In LISA, the effective data rate requirement is about 15 kbps with bit error rates (BER) close to zero. As shown later in the optical experimentation (section 5.2.1), highly reliable data communication is achieved in weak-light conditions after a forward error correction (FEC) technique (e.g. Reed-Solomon encoding) by including redundancy in the data bits transmitted with a raw rate of 24 kbps. By comparing figure 29 and figure 30, one may realize that the impact of data encoding in the auto-correlation function is similar to the second code interference, but lower (see figure 31) than the shot noise effect given the weak-light power conditions and the low-depth modulation index (0.1 rad). Figure 31 shows a preliminary characterization of the distortion in the autocorrelation function given a LISA-like shot noise reference of $60 \mu\text{rad}/\sqrt{\text{Hz}}$ (see shot noise characterization in section 3.2). Note that the codes spread over a photoreceiver bandwidth of about 20 MHz are thus buried in an additive white Gaussian noise (AWGN) distribution. Even under these conditions, a correlation peak is observed with a relatively high amplitude margin. Thereby, the shot noise contribution is the expected dominant source of ranging errors.

4.5 SIGNAL STRUCTURE

The input signal of the ranging receiver is formed by averaging eight independent phase measurements of two quadrant photoreceivers (QPDs) operating in hot redundancy (see section 3.1). This configuration is depicted in figure 15, and it maximizes the

chips running at roughly 1 MHz. Hence, one PRN period contains several data bit periods. This leads to the requirement of easily divisible code length, i.e., 1024 instead of 1023

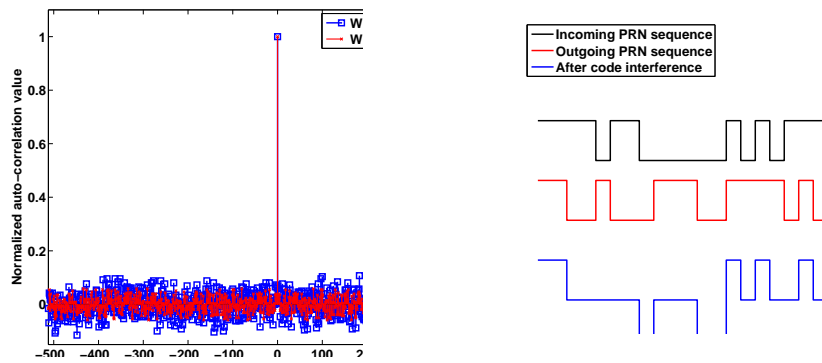


Figure 29: (Left side) Auto-correlation function after incoming and outgoing code interference given by the laser transponder configuration. (Right side) Time series of the two code sequences and its resulting interference.

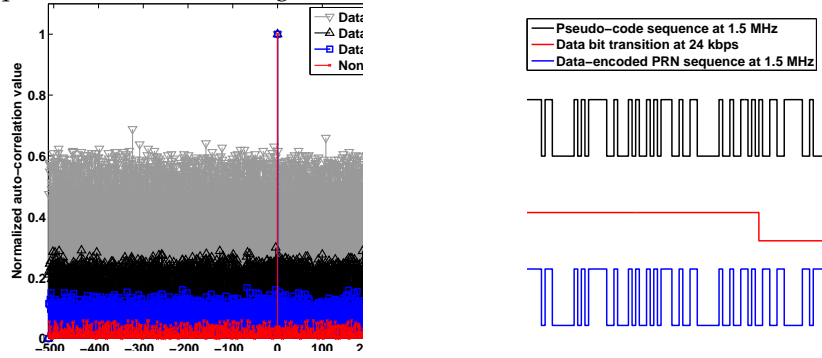


Figure 30: (Left side) Auto-correlation functions under different data rates. The designed code shows a peak of correlation up to 300 kbps. The LISA mission requires lower data rates (≈ 15 kbps). A raw data rate of 24 kbps has been implemented and tested in this thesis. (Right side) illustrates the resulting time series of a data-encoded PRN sequence at 24 kbps.

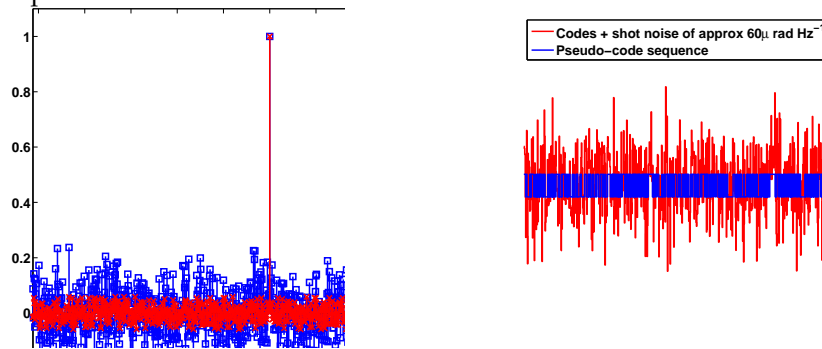


Figure 31: (Left side) Auto-correlation function in presence of LISA-like shot noise. (Right side) Time series of a PRN code within noise spectral density of $60\mu\text{rad}/\sqrt{\text{Hz}}$ over a photoreceiver bandwidth of 20 MHz.

received optical power at the input of the ranging system. Thus, if a QPD fails, the carrier-to-noise density (C/N_0) would decrease by a factor of $\sqrt{2}$, degrading the overall ranging performance as observed in Table 1 of chapter 3. Throughout this thesis, the worst case is assumed and the ranging architecture is designed taking into account an equivalent input signal with four (one QPD) active segments.

As shown previously in chapter 3, a signal model of the expected output for a quadrant segment in the science interferometer is given by

$$\begin{aligned} V_{\text{seg}}^{\text{AC}}(t) &= \eta G_{\text{TIA}} J_0^2(m_{\text{sb}}) \frac{1}{N} \cdot \sqrt{\gamma P_{\text{LO}} P_s} \cdot \sin\left(\omega_{\text{het}} t + \phi + m_{\text{prn}} \sum_{n=-\infty}^{\infty} c_n p(t - nT_c)\right) \\ &+ \eta G_{\text{TIA}} J_1^2(m_{\text{sb}}) \frac{1}{N} \cdot \sqrt{\gamma P_{\text{LO}} P_s} \cdot \sin(\omega_{\text{sb1}} t + \phi_{\text{sb1}}) \\ &+ \eta G_{\text{TIA}} J_1^2(m_{\text{sb}}) \frac{1}{N} \cdot \sqrt{\gamma P_{\text{LO}} P_s} \cdot \sin(\omega_{\text{sb2}} t + \phi_{\text{sb2}}) + n(t) \quad [\text{V}], \end{aligned} \quad (4.5)$$

where η is the photodiode responsivity. G_{TIA} refers to the overall gain of the transimpedance amplifier (TIA). $J_0(m_{\text{sb}})$ and $J_1(m_{\text{sb}})$ are the Bessel functions of first kind, which result from sinusoidal clock sideband modulation scheme with an equivalent modulation index m_{sb} . N represents the number of segments with either $N=4$ for a QPD or $N=1$ for a single element photoreceiver. γ denotes the heterodyne efficiency. P_{LO} and P_s are the available optical powers at the input port of a beam splitter² for the incoming signal and local oscillator beams respectively. ω_{het} , ω_{sb1} , ω_{sb2} are the angular heterodyne frequencies for the main carrier-to-carrier beat note, the lower sideband-to-sideband beat note and the upper sideband-to-sideband beat note respectively. ϕ , ϕ_{sb1} and ϕ_{sb2} represent their phases, which contain the science information and residual noises such as laser phase noise. m_{prn} denotes the modulation index applied for ranging and data communication. c_n is a binary PRN-data encoded sequence with either +1 or -1 values and a pulse shape given by $p(t)$ of period $1/T_c$. The second code presents a similar shape, but different code and data bit sequences. $n(t)$ denotes the shot noise at the output of the transimpedance amplifier (TIA). The signal levels and the applied modulation indices were already described in chapter 3.1.

Figure 32 shows the resulting spectrum of this signal in dBm according to the signal levels and the noise analysis summarized in Table 3. Note a power reduction in the sideband beat notes by a factor of $J_1^4(m_{\text{sb}})/J_0^4(m_{\text{sb}})$ with respect to the main carrier, i.e., roughly 24 dB for $m_{\text{sb}} \approx 0.45$. The DS/SS modulation spreads its power throughout a large bandwidth. Most of the code energy is packed into the first pair of sidelobes with nulls at $\pm 1/T$, i.e., ± 1.5 MHz (current PRN chipping rate as described later section 4.6.3)

² In the science interferometer, it is considered a beam splitter with a 50:50 coating. The optical powers P_s and P_{LO} are referred before beam interference.

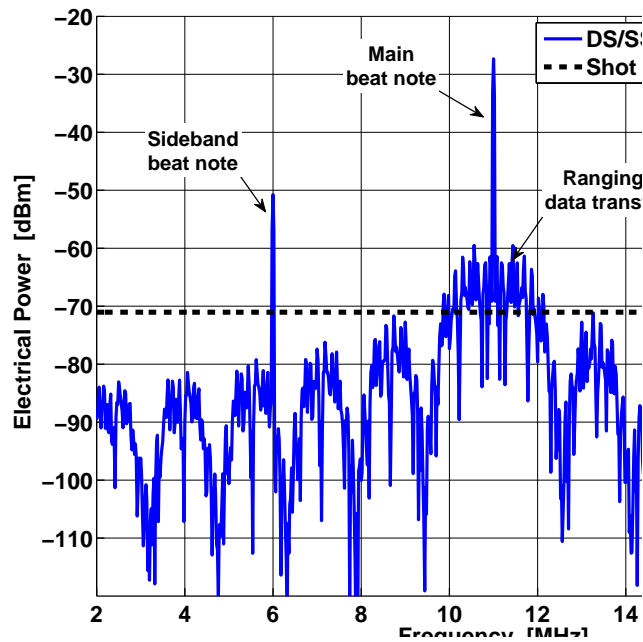


Figure 32: Expected photoreceiver power spectrum of a low-depth DS/SS modulation scheme with clock tone sidebands. The PRN sequences are encoded with a non-returning zero (NRZ) scheme, where its code power spectrum is maximum at the carrier frequency.

with respect to the main carrier, and where the adjacent sidelobes lead to a power loss of about 10 dB. The PRN format is based on non-return to zero (NRZ) basis, and hence, the spectrum reaches its maximum at the carrier frequency. This signal model was confirmed in the optical experiment described in chapter 5.

Alternatively, as shown in figure 33, the PRN sequences can be encoded using a standard Manchester pulse shape, whose power spectrum is zero at the carrier frequency. Figure 34 shows a signal model of the resulting spectrum for a DS/SS modulation with Manchester encoding, and clock tone sidebands. This way, the PRN energy has been transferred to a higher frequency band, twice as wide, being the first pair of sidelobes shifted to 1.5 MHz from the main carrier frequency. This technique is planned since the carrier-tracking loop with a typical bandwidth in the kHz range would result in a reduction of the effect of code interference around its tracking point, and therefore provides operation of the feedback control loop with an enhanced carrier phase performance in presence of a DS/SS modulation. As analyzed in detail throughout the following section, Manchester encoding aims to reduce the PRN distortion given the phase response of the phasemeter architecture.

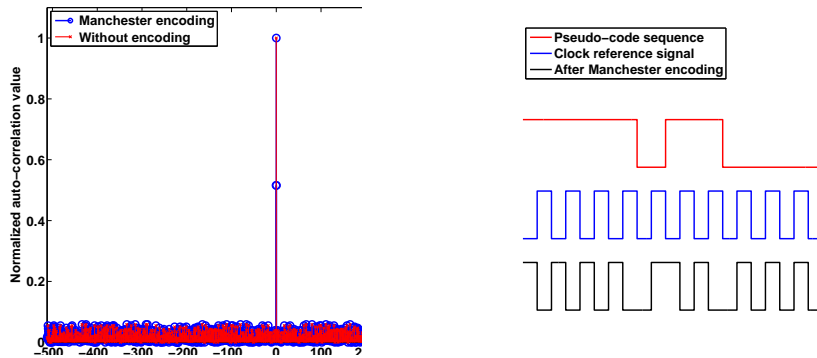


Figure 33: (Left side) Auto-correlation function of a Manchester encoding pulse shape. Manchester encoding doubles the code bandwidth, but ensures a bit transition every code chip. This technique aims to reduce the PRN distortion given by the phase response at the output of the phasemeter architecture. (Right side) Time series after applying Manchester encoding.

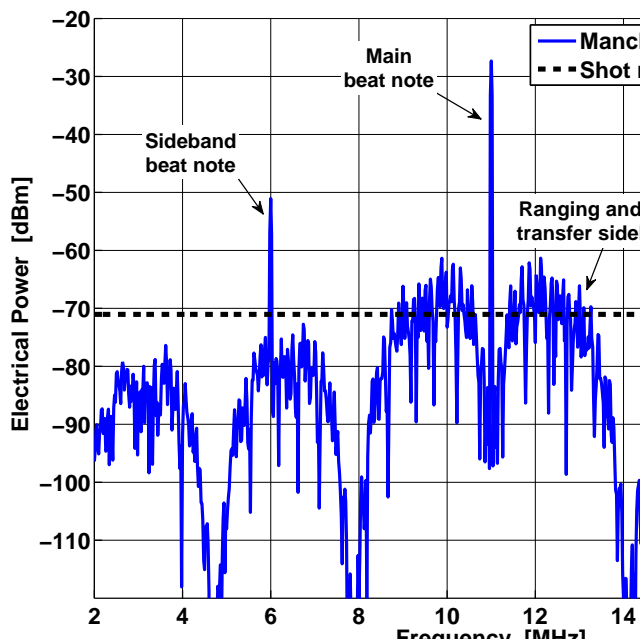


Figure 34: Spectrum model for the expected signal at the output of the science photodetector with Manchester encoding for binary streams at $[-1, 1]$. The code power spectrum is zero at the carrier frequency.

Baseline parameter	Design value
Heterodyne frequency range	$f_{\text{het}} = 2\text{-}20 \text{ MHz}$
Optical signal power	$P_s = 200 \text{ pW}$
Optical local oscillator power	$P_{\text{LO}} = 2 \text{ mW}$
Photodiode responsivity	$\eta = 0.7 \text{ [A/W]}$
Heterodyne efficiency	$\gamma = 0.7$
Sideband modulation index	$m_{\text{sb}} = 0.5 \text{ rad}$
PRN modulation index	$m_{\text{prn}} = 0.1 \text{ rad}$
PRN frequency	$f_{\text{prn}} \approx 1.5 \text{ MHz}$
Data rate	$\text{DR} = 24 \text{ kbps}$
Transimpedance resistance	$R_{\text{TIA}} = 5.11 \text{ k}\Omega$
Second amplification stage	$g = 8.2$
Overall transimpedance gain	$G_{\text{TIA}} = g \cdot R_{\text{TIA}} = 41.9 \text{ k}\Omega$
Load resistance	$R_{\text{load}} = 50 \text{ }\Omega$
Photocurrent noise	$\tilde{i}_{\text{se}}(f) \approx 15 \text{ pA}/\sqrt{\text{Hz}}$

Table 3: Design parameters taken into account in this analysis

4.6 RECEIVER ARCHITECTURE

The core architecture of the LISA phasemeter is based on a phase locked-loop (PLL) operating on the frequency range between 2 MHz to 20 MHz. This architecture was chosen after numerous previous experiments at the AEI [63, 64, 65] together with relevant research centers such as NASA/JPL [66, 67] and the University of Florida in Gainesville [68]. Benefits of our prototype with respect other groups include a custom-designed breadboard based on space-compatible FPGA (see section 4.7). It allows portability to flight hardware. The current performance of our design complies with LISA requirements. The phase performance of the digital control loop in the relevant measurement band is shown in section 4.8. Ongoing developments include the integration of the proposed phasemeter architecture together with the ranging architecture (see section 4.6.2) in a LMS breadboard (see section 2.3). The LMS breadboard is being implemented in the framework of the ESA project [37] *LISA metrology system* under a scientific collaboration with DTU Space and Axcon at the AEI facilities.

A general block diagram of the digital ranging receiver, and its integration with the LISA phasemeter is shown in figure 35. The first stage in the digital receiver is the phase demodulation of the PRN sequences encoded on the beat notes at the photodetectors

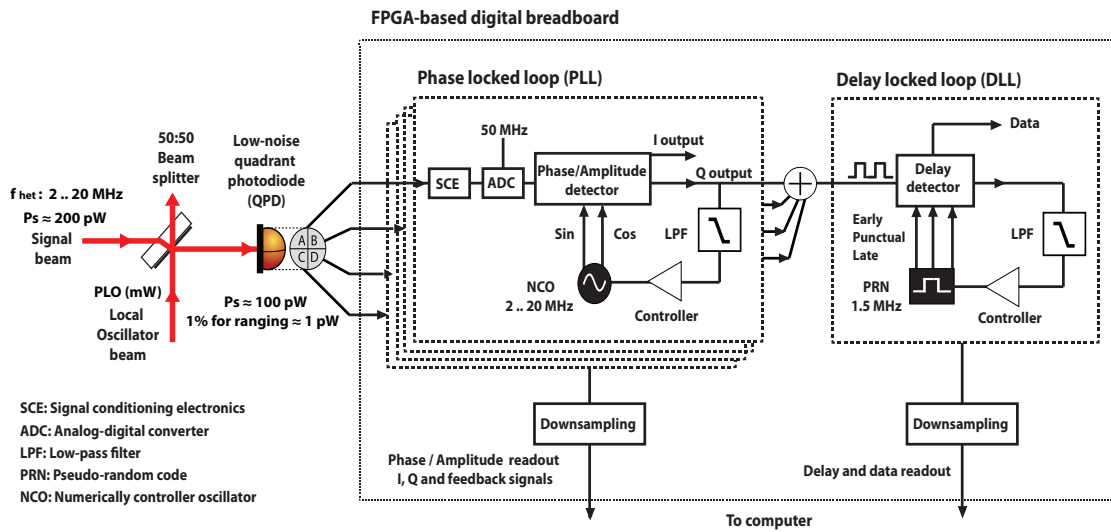


Figure 35: General architecture and interfaces of the digital control loops implemented for phase readout, ranging and data transfer.

on the optical benches. A digital phase-locked loop (PLL) architecture locks the phase of a numerically-controlled oscillator (NCO) to the incoming beat note. A phase and amplitude detector based on an in-phase/quadrature (I/Q) demodulator is used to control the NCO in a feedback loop. The phase measurement is obtained in a floating-point unit as the sum of raw phase estimations from the NCO and the arctangent of the I and Q components, while the amplitude of the beat note is computed as $\sqrt{I^2 + Q^2}$. Once the phase of the beat note has been processed, the PRN code modulated onto the optical carrier appears as abrupt phase transitions at the Q output, providing the input signal to the DLL for ranging measurements (described in section 4.6.2). The correlation of the incoming signal is computed with three versions of the same reference PRN: a punctual, an early and a late one. The punctual version is not delayed with respect to the received PRN. The early and late versions of the reference code are spaced with a delay difference smaller than one chip period. The punctual correlator is mainly responsible for data recovery and code acquisition, whereas the difference between early and late correlators is used as the error signal in a control loop to update the delay of the code generator to the input signal, thus providing tracking capabilities between the incoming and the local PRN sequences.

Apart from the phase demodulation of ranging signals, the phasemeter architecture allows the implementation of the following functions:

- Interferometric readout of the carrier beat note to provide the main science data streams, including GW measurements to the on-board computer at a measurement rate between 3 Hz to 10 Hz.
- Interferometric readout of the clock beat note sidebands to measure the relative phase noise between individual on-board clocks.
- Angular measurements for precise laser pointing and satellite drag-free control via differential wavefront sensing (DWS), as it is being implemented on the precursor mission LISA Pathfinder.
- Phase measurements with a bandwidth of about 1 MHz for laser frequency control by applying an offset-phase locking method [69, 57]. It enables a laser transponder configuration [70].
- ADC time jitter measurements for beat note sampling rate corrections through a pilot tone calibration with a phase sensitivity of $2\pi \times 10^{-6}$ rad/ $\sqrt{\text{Hz}}$ and a measurement rate of between 3 Hz to 10 Hz (described in section 3.5 in chapter 3).
- Doppler estimations by reading out the NCO frequency register, enabling precise measurements of both relative inter-satellite distance and velocity. This aims to smooth the absolute ranging measurements by post-processing on-ground.

Note that a PLL channel implements a Single-Bin Discrete Fourier Transform (SB-DFT) by computing the magnitude and phase components of an input signal for a single frequency. Through the I and Q phase readout and by opening the feedback loop, the phasemeter can be used to perform the input signal spectra for lock acquisition. By setting the frequency of the LO at different steps, a simple scanning with a resolution of a few kHz can obtain the spectra in the beat note MHz frequency range. Although in laboratory conditions this method is valid, in practice for LISA the spectral computation for the beat note acquisition needs to be as fast as possible (see section 3.4.4 for further details). A FPGA-based Fast Fourier Transform (FFT) algorithm, which processes in parallel different bin frequencies, will be implemented to significantly reduce the computing time, and subsequently the beat note acquisition time.

A more detailed view of the core processing for a digital phasemeter channel is reported in the following sections. Although the core architecture is similar for performing all those capabilities described above, the design parameters can differ accordingly to the expected input signal levels, i.e., depending on the incoming signal: a pilot tone, a sideband beat note or the main carrier beat note. Thus, each PLL instance is designed to optimize the loop parameters for the specific signal characteristic in terms of bandwidth, filtering and phase readout. Throughout the next sections, the proposed design parameters take into account the current implementation used for laser ranging and data communication.

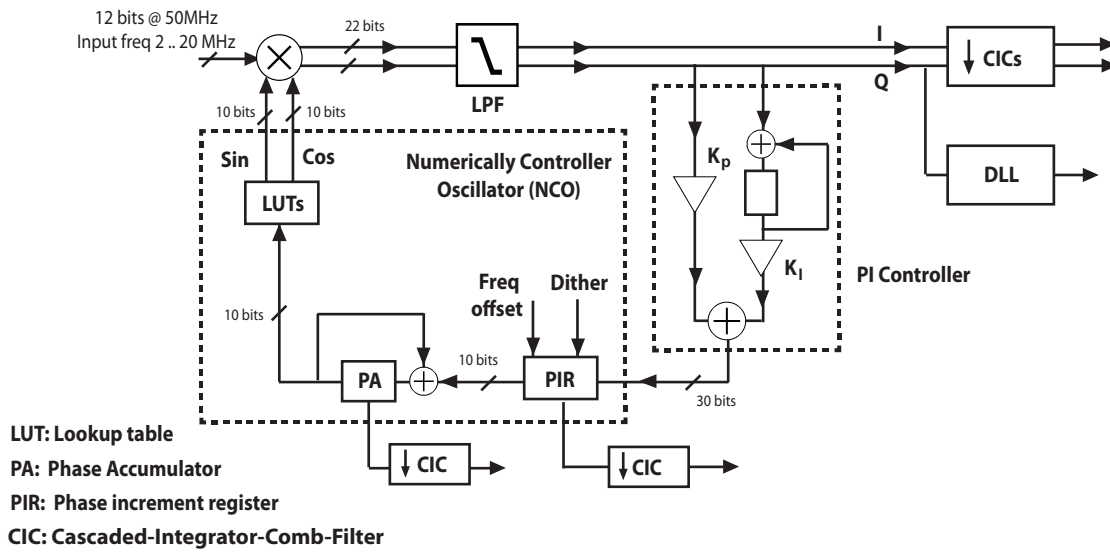


Figure 36: Digital block diagram of the phase-locked loop (PLL) core architecture for a single phasemeter channel. The control loop operates at the sampling frequency (50 MHz). For amplitude, frequency (PIR) and phase readout (PA), a down-sampling scheme based on CIC filters provides: the in-phase (I), the quadrature (Q) and the feedback signals (either PA or PIR) to a computer at Hz rates.

4.6.1 Phase measurement system: phase-locked loop

The core processing of the LISA phasemeter is based on a phase lock loop (PLL) architecture with an allocated phase noise budget of $2\pi \times 10^{-6} \text{ rad}/\sqrt{\text{Hz}}$ in the frequency range from 0.1 mHz to 100 mHz. The phasemeter must be able to operate in the presence of slowly varying Doppler shifts ($\approx \pm 4 \text{ Hz/s}$) with a beat note frequency range up to 20 MHz. In addition, the PLL is designed to isolate and extract the phase information from individual beat notes contained in the incoming photoreceiver signal, which are affected by strong noise sources including laser frequency noise and shot noise. In particular, the pilot tone is electrically added to the incoming photo-voltage signal, and therefore it is affected by the same shot noise background than the science beat notes. However, the pilot tone is an electrical signal derived from the ultra-stable oscillator, and it is therefore not affected by laser frequency noise. Its phase measurement is basically dominated by ADC time jitter in the mHz frequency range and by shot noise at higher frequencies.

Figure 36 shows the digital realization of the proposed phasemeter architecture. In order to reduce aliasing, the incoming beat signal is processed with an analog low-pass filter. After filtering, the signal is digitized in a low-noise analog-to-digital converter

(ADC) at a 50 MHz sampling rate and fed into the FPGA ³. The phase detection begins with the quadrature multiplication of the incoming beat note with a sine-cosine signal generated by a standard numerically controlled oscillator (NCO), consisting of a lookup table (LUT), phase accumulator (PA) and a phase increment register (PIR). The result of the multiplication, after low-pass filtering (LPF), produces in general two digital sine waves (I/Q) as outputs which are 90° out of phase. Their frequency is given by the difference between incoming signal frequency and NCO frequency. In lock, the frequency is held close to zero. For small in-loop phase changes $\phi \ll 1$, the I component is proportional to the amplitude of the incoming signal ($A \cdot \cos\phi \rightarrow A$), while the Q component is proportional ($A \cdot \sin\phi \rightarrow A \cdot \phi$) to the phase itself. Thus the Q channel is used as error signal in a feedback loop to adjust the phase of the NCO to the incoming beat note. This is done with a proportional-integral (PI) controller that transforms the phase error in a feedback signal for the PIR. Thus, the phase readout can be computed from the feedback signal based on:

- Phase increment register (PIR) readout: The PIR holds the instantaneous output frequency of the NCO. This register is initialized after phase acquisition with an estimation of the input signal frequency, which is shown in figure 36 as frequency offset. In lock, the PIR value is updated by the PI controller to make the NCO frequency track to the incoming signal, and thus the beat note phase can be derived from the PIR output by integration. The phase readouts of the main carrier beat, pilot tone and clock sideband beat notes are computed based on the down-sampled PIR measurements.
- Phase accumulator (PA) readout: The PA integrates the instantaneous frequency estimations from the PIR register, providing an accurate phase measurement every clock cycle. The PA value increases rapidly, which makes it being in practice more complicated to down-sample to the low measurement band (3 Hz to 10 Hz) for phase readout. However, the PA readout is needed for differential wavefront sensing (DWS) [38, 39] since DWS needs differences between absolute phases which are achievable only in the PA. Phase reconstruction from the PIR requires integration which involves an unknown constant.

In order to measure either phase noise outside the bandwidth of the PLL or high residual noise within its bandwidth, the arctangent (Q/I) is added to the NCO readout. This yields to a high-fidelity phase reconstruction even being close to the non-linear range of the phase detector.

Figure 36 shows in detail the bit resolution in the designed architecture. In order to reduce the number of bits in the control loop, and hence to reduce both the computational burden in the FPGA and the storage requirements, the LUT is addressed with

³ Future work will operate the LISA phasemeter at a sampling rate of 80 MHz, in accordance with the ESA project: LISA metrology system.

resolution of $b = 10$ bits. Thus, the PA is truncated before being fed to the LUT. As side-effect of the phase truncation, spurious peaks appear in the spectral performance at the output of the NCO, which depend on the PIR value and the truncation factor [71, 72]. An optimization in the control loop architecture can be achieved by implementing a suitable dithering technique [73]. By applying a triangular noise distribution of Dither at the least significant bit of the PA accumulator, these peaks vanish since this breaks the periodic errors given by the finite precision of the NCO. The phase noise introduced by dithering is well below the required phasemeter performance (see results of the digital phasemeter performance in figure 52). The induced dithering in our prototype yields to a linear phase noise spectral density of

$$\tilde{\vartheta}_{\text{Dither}} = \frac{2\pi\sqrt{3}}{2^b\sqrt{6}\cdot f_{\text{samp}}} \quad [\text{rad}/\sqrt{\text{Hz}}]. \quad (4.6)$$

This phasemeter architecture has been modeled, and implemented in the hardware breadboard. After designing the feedback control, and programming it into a FPGA processor, the loop behavior is controlled by setting the proportional k_P and integral k_I gains of the PI controller (see figure 36). The following section describes the loop behavior with a linear phasemeter model.

Phase-lock loop analysis: linear model

The behavior of the digital feedback control is analyzed taking into account the three basic blocks shown in figure 37: a phase detector, a loop filter and a numerically-controlled oscillator (NCO). Assuming that the loop is locked and is being operated within its linear range, the phase detector output is given by

$$u_d[n] = k_d \underbrace{(\theta_i[n] - \theta_o[n])}_{\theta_e[n]}, \quad (4.7)$$

where n denotes the sample index. k_d is the phase-detector gain factor, which is proportional to the input signal amplitude levels. $\theta_i[n]$ and $\theta_o[n]$ denote the phase steps of the input signal and the NCO output respectively, and $\theta_e[n]$ are the equivalent phase error. The phase detector output is fed into a loop filter. The loop filter consists of both the PI controller and the extra delay elements needed for its hardware implementation. The delay elements are counted as D clock cycles. The loop filter, characterized by its transfer function $F(z)$ in the z -domain, provides a reference frequency to the NCO every clock cycle

$$L(z) = \frac{F(z)}{U_d(z)} = \left(k_p + k_i \frac{z^{-1}}{1-z^{-1}} \right) \cdot z^{-D}. \quad (4.8)$$

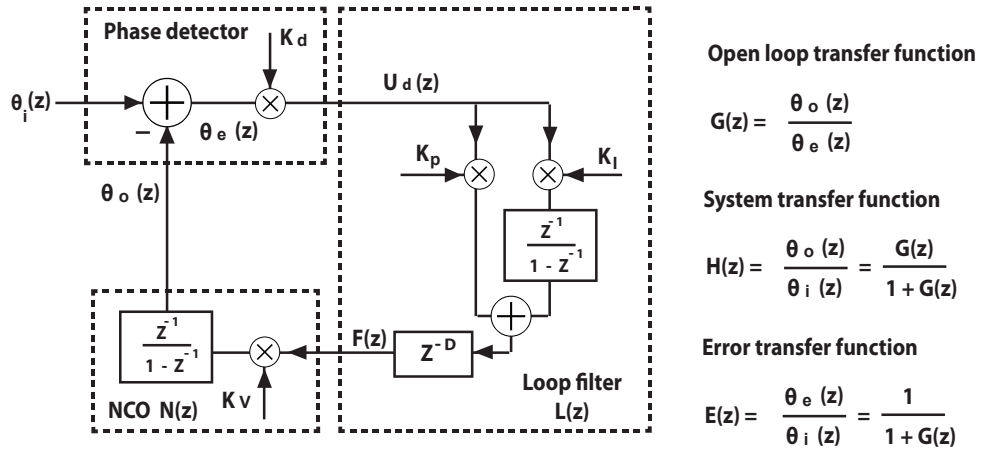


Figure 37: Linear model for the phase-locked loop and description of the main transfer functions.

Once the PLL has been implemented, k_p and k_i are used to control the loop response. By accumulating the output of the loop filter, the frequency signal $F(z)$ is converted to phase modulo one cycle (2π rad) in the NCO. Thus, the implemented NCO transfer function is given by

$$N(z) = \frac{\theta_o(z)}{F(z)} = kv \frac{z^{-1}}{1 - z^{-1}}, \tag{4.9}$$

where kv is the phase scaling coefficient (either 1 cycle or 2π rad).

The transfer functions of the individual elements can be combined to compute the open-loop transfer function given by

$$G(z) = \frac{\theta_o(z)}{\theta_e(z)} = kd L(z)N(z) = kd \cdot kv \cdot \frac{z^{-1}}{1 - z^{-1}} \cdot \left(k_p + k_i \frac{z^{-1}}{1 - z^{-1}} \right) \cdot z^{-D}. \tag{4.10}$$

Figure 38 represents the frequency response of the open-loop transfer function. As previously mentioned, the used loop parameters are in accordance with the current implementation for ranging and data communication. As known in standard control theory, the PLL is stable if its phase lag at the unity gain frequency (crossover frequency at 0 dB) is higher than -180° . As shown in the frequency response plots, the designed loop is stable providing a phase margin of $\approx 30^\circ$ and has a unity gain frequency of approximately 250 kHz.

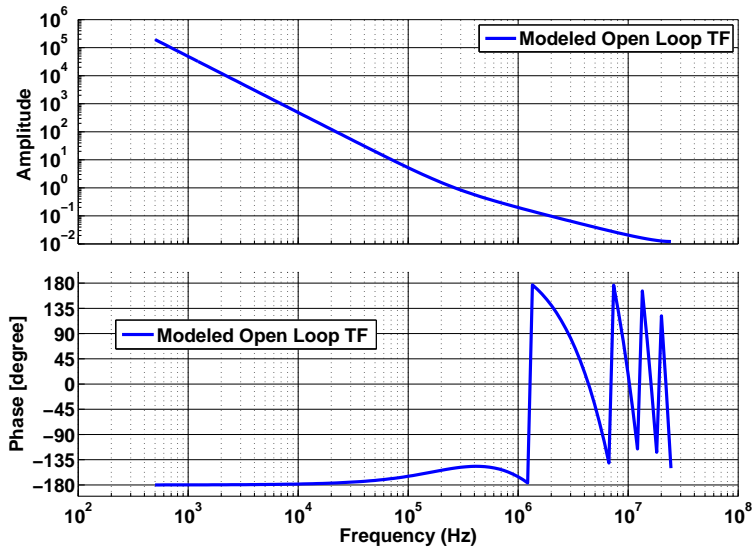


Figure 38: Open-loop transfer function of the phasemeter feedback control used for ranging and data communication.

The PLL in close loop operation described as a linear system is characterized by the system transfer function $H(z)$, which can be derived from equation 4.10 as

$$H(z) = \frac{\theta_o(z)}{\theta_i(z)} = \frac{G(z)}{1 + G(z)}. \quad (4.11)$$

In order to validate the applied linear model, the transfer function of the system was measured by a software simulation of the final phasemeter code ⁴. To this end, white Gaussian noise floor reference with frequency components in a broad spectral range (25 MHz) was used as input phase (θ_i). In closed loop operation, the resulting time series of θ_o and θ_e were measured to compute the different PLL transfer functions. Figure 39 shows a comparison between the modeled and the measured $H(z)$. Note that the PLL behaves as a low-pass filter with a bandwidth of a few hundred kHz. This way, the bandwidth is designed for tracking optical signals with the expected phase fluctuations driven by free-running laser frequency noise (see noise description in section 3.4.2). The control loop suppresses spurious high frequency components such as ranging signals from the interferometric measurements. Results of the PRN impact onto the phasemeter performance is described in section 4.8.1.

⁴ A LISA-like phasemeter was implemented in Matlab/Simulink using a specific tool that provides VHDL code for its final implementation into the FPGA, further details in appendix F.1.

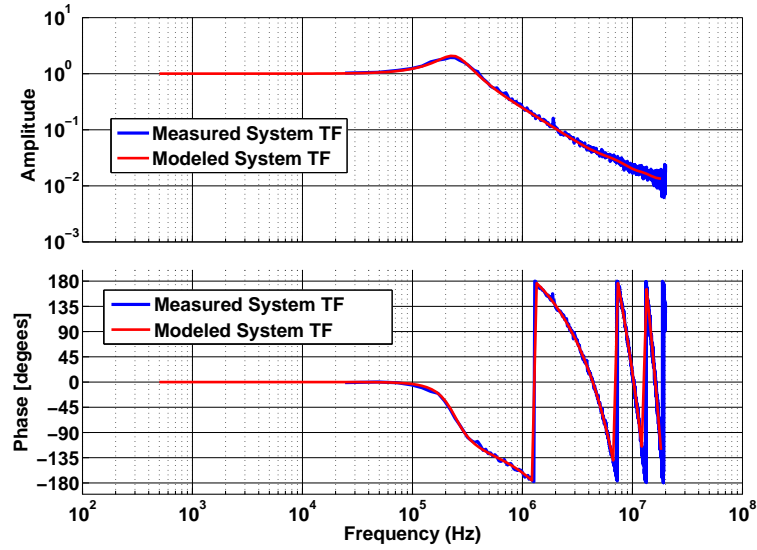


Figure 39: Comparison between the modeled and the measured system transfer function of a LISA-like phasemeter.

The input signal for the ranging system is the feedback phase error of the PLL. Thus, the PLL with a bandwidth in the kHz range behaves as a high-pass filter for the PRN pulse shape. This effect is characterized by the PLL error transfer function

$$E(z) = \frac{\theta_e(z)}{\theta_i(z)} = \frac{1}{1 + G(z)}. \quad (4.12)$$

Figure 40 shows the frequency response of $E(z)$. As described in section 4.5, the ranging spectrum spreads over a wide frequency range. This in combination with the high-pass filtering yield a pulse shape distortion in the ranging signal. Figure 41 illustrates the PRN distortion at the phasemeter output for a simulated FPGA-based beat note at 12 MHz, and a ranging signal running at 1.5 MHz. As observed, this high-pass filtering effect is even more significant for long code sequences without intermediate transitions. Due to the PLL action, the phase error is driven towards zero, inducing a visible decay in the pulse shape. In order to mitigate this effect, the PRN sequences can be alternatively encoded with a Manchester scheme. This method ensures a phase transition at the middle of each code bit. Therefore, it reduces the distortion in the pulse shape when passing through the phasemeter at the expenses, however, of doubling the ranging bandwidth.

From the phase response of the error transfer function, it is possible to estimate the time delay offset that the ranging signal experiences when passing through the phasemeter.

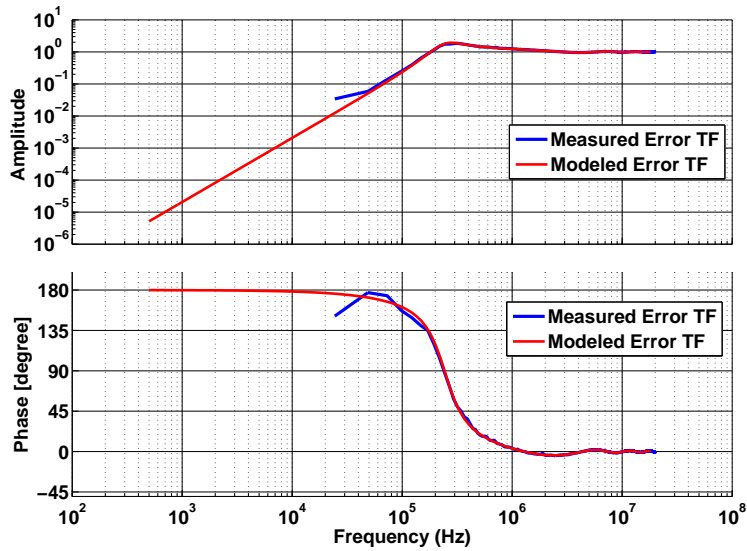


Figure 40: Error transfer function of the phasemeter feedback control.

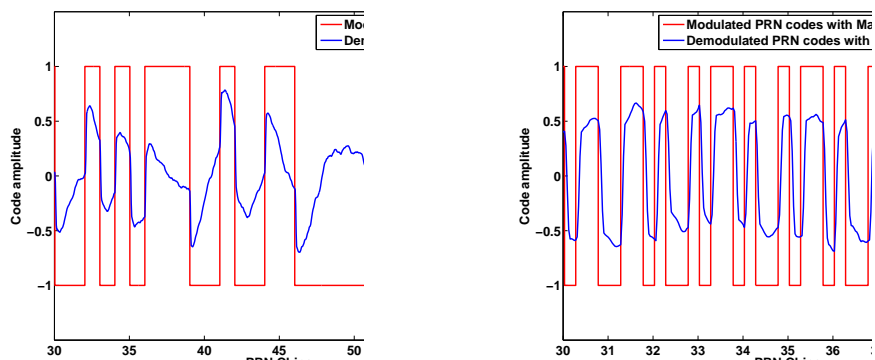


Figure 41: (Left side) PRN distortion due to the phasemeter pulse response. This effect can be reduced by encoding the ranging signal with a Manchester scheme.

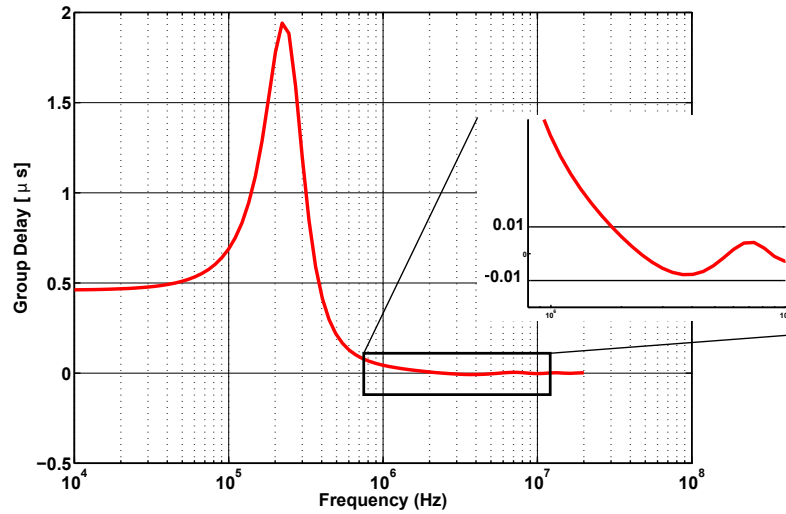


Figure 42: Expected group delay given by the phasemeter phase response.

In figure 42, the group delay of the phase error is computed, showing a delay offset at 1.5 MHz of ≈ 10 ns. This way, the time delay offset experienced by the PRN signal is expected to be below the DLL time resolution of ≈ 20 ns. Further experimental investigations are required to confirm this estimation by including an additional DLL instance for tracking both the incoming and outgoing (local) PRN codes. By tracking the outgoing PRN code, the local delay offset in the signal chain can be measured and transmitted to ground for timing corrections. A second DLL instance in the FPGA signal processing will also allow to reduce cross correlation errors due to PRN interferences. To this end, the local PRN copies of each DLL are adjusted in delay and amplitude to be subtracted from their input signals prior to delay tracking.

4.6.2 Ranging system: delay-locked loop

The use of a delay-locked loop (DLL) architecture for ranging measurements and data transfer was first proposed in 2002 by the AEI [31]. In this thesis, we show the first experimental demonstration of the proposed architecture, achieving performance under the stringent requirements of the mission. Figure 43 shows a block diagram of the realization of the DLL architecture. It consists of three main blocks: a delay detector, a loop filter and a PRN code generator. The delay detector performs the correlation of the incoming PRN signal, $d_n p(t - \tau)$, with three versions of the same reference PRN: a punctual, $p(t - \hat{\tau})$, an early, $p(t - \hat{\tau} + T_c/2)$, and a late version, $p(t - \hat{\tau} - T_c/2)$, where T_c is the chip period and $\hat{\tau}$ is the estimated delay. The punctual correlator is responsible for data recovery and peak detection, whereas the difference between early and late correlators is used as the error signal by the DLL loop filter to update the delay of

the code generator to the input signal, thus providing tracking between the incoming and the local PRN. Each correlator is implemented by mixing the incoming code and the local PRN to be afterward integrated over a data bit period. The polarity of the correlation is used to extract the encoded data from the PRN sequence as explained later in this section. A control logic is designed within the FPGA processor to switch between two different operation modes:

- **Code acquisition:** it is accomplished by adjusting the punctual correlator until the timing offset between the locally generated reference code and the incoming code are aligned for maximal correlation. This way, the delay between the local and incoming PRN sequences is determined at μs accuracy (one chip length). The local PRN is shifted with a coarse resolution of one code period until a correlation peak is detected at the correct delay. A lower code period could be used, but this would increase the acquisition time. Additional details on code acquisition are given in chapter 5 based on optical measurements. It concludes that a good compromise between the resulting correlation peak amplitude and the code step period provides an acquisition time from 0.67 s to 1.3 s for a 50 MHz sampling clock.
- **Tracking mode:** once the acquisition is finished, the timing delay is determined with higher resolution (ns accuracy), enabling data transfer. In the current implementation, the estimated delay can be updated between 24 kHz and 1.5 kHz, which corresponds to a data bit rate and a full code length rate respectively.

Binary data is encoded with the PRN sequence at lower rates (24 kHz) by a bitwise operation (XOR) of both sequences which divides the code length into several data periods. However, as the length of one data period is shortened with respect to one full code period, a coherent integration is only possible over one data bit. The rest of the code correlation is then completed by incoherent integration, resulting in a degraded code tracking performance of the system. As shown in figure 43, this also requires the implementation of either the absolute value or the squared value in the correlator architecture. This way, a first stage correlation implements a coherent integration every data period (T_d). The sign of the correlation output depends on the polarity of the received data, enabling data bit decoding. By adding the absolute value of each data period over a full code-length, the correlation function is recovered for code acquisition and tracking. Another feature of the designed system is a configurable measurement rate in the range of one data period and up to one full code-length correlation period. This feature allows to investigate the design for an optimal delay estimation by setting the number of measurement points. The delay readout is then averaged to a few Hertz and delivered to the on-board computer.

An optimization in the proposed architecture is the implementation of the PRN code generator based on look-up tables (LUT) instead of the classical linear feedback shift

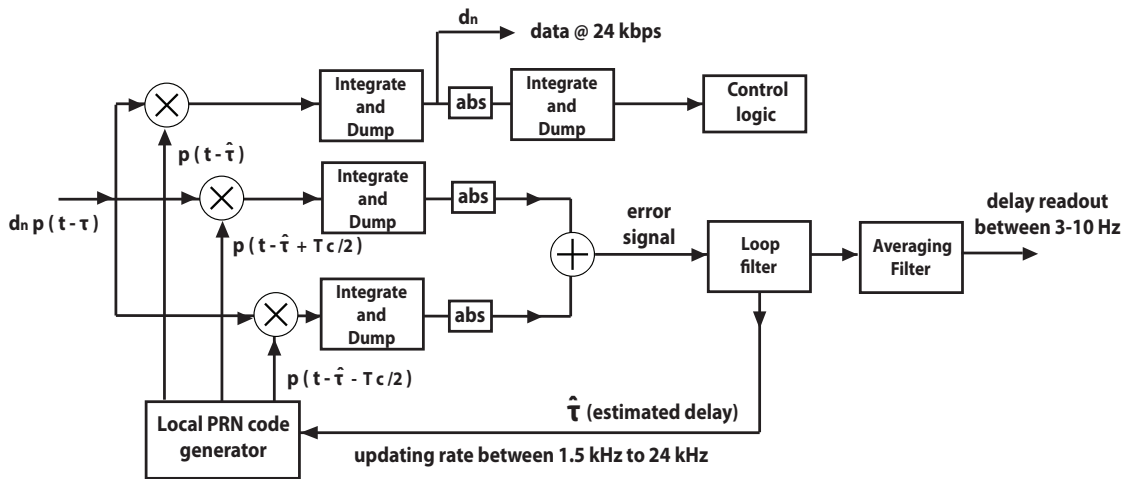


Figure 43: General block diagram of the control loop implemented for ranging and data communication. A data-encoded PRN signal coming from the phasemeter is correlated with three versions of the same pseudocode to perform data readout and delay measurements. An on-time version “punctual”, an early (shifted by $+T_c/2$) and a late (shifted by $-T_c/2$).

register (LFSR). The LUT configuration, or alternatively RAM-memories, stores and provides the PRN sequences, enabling its re-programming by software without re-routing the hardware circuit. Moreover, it allows the optimization of the correlation properties of the PRN sequences by applying numerical data analysis techniques (see section 4.4). Thereby, the LISA codes can be generated independently of a primitive polynomial (as with Gold codes), and with the desired code length.

4.6.3 Ranging design parameters

The chipping rate is designed as an integer sub-multiple of the FPGA sampling frequency, and the data rate as a sub-division of the PRN codes, both being strictly synchronized with the on-board clock, and preferably using modulo-2 divisions of the sampling frequency to reduce the FPGA computational load. The design parameters of the pseudo-codes are described in figure 44. The codes sampled at 50 MHz run at a chipping rate of ≈ 1.5 Mbps (50 MHz/32 samples) limited by the lower frequency of the beat note, and encoded with data streams at a maximum rate of 24.4 kbps (50 MHz/2048 samples). The data-encoded PRN signal provides a delay resolution of 20 ns $\simeq 6$ m with an update rate between 24.4 kHz and 1.5 kHz (50MHz/32768 samples, full code-length). Since the on board computer in LISA requires regular update rates between 3-10 Hz, the delay measurements are averaged down to achieve sub-meter absolute distance resolution (see results in chapter 5). Note that under these design parameters, the codes are periodic every 200 km over the 5 million kilometers, and therefore an initial

positioning system is required. The deep-space network (DNS) can provide an absolute inter-satellite distance with a resolution of ≈ 25 km. Here, a more accurate distance determination will be achieved using the proposed DLL architecture.

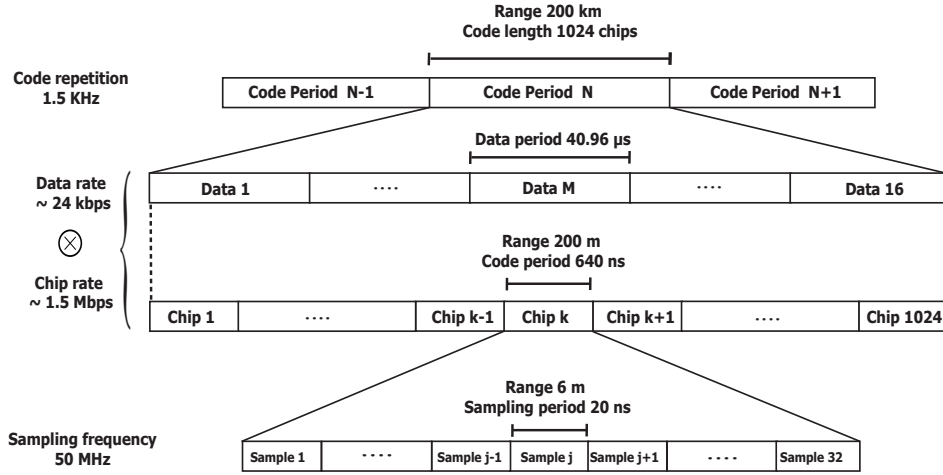


Figure 44: Design parameters of the ranging system. Code length of 1024 chips running at 1.5 Mbps encoded with a data rate at 24.4 kbps and sampled at 50 MHz. The design parameters enable a ranging system with an ambiguity range of 200 km, a distance resolution of 6 m, and a measurement rate of 1.5 kHz.

Due to the diffraction losses of the laser over the long inter-satellite beam propagation and additional optical losses on the optical bench, only around 1 pW of optical power is received for ranging and data communication. The low-light power available yields a ranging signal below the shot noise level (see section 4.5 for further details). Under these conditions, the shot noise introduced by the lasers at the photodetector limits the ranging accuracy and increases the data errors for optical communication. A forward error correction (FEC) coding format is implemented on top of the data streams to detect and correct bit errors in the optical communications. Note that this technique is independent of the previously mentioned Manchester encoding which aims to reduce the PRN distortion due to the phasemeter response.

4.6.4 Data bit synchronization and bit error corrections

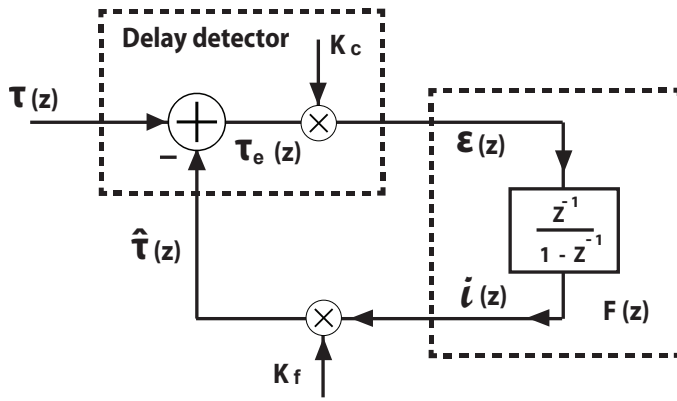
The DLL architecture recovers the data by mixing the incoming and local PRN copies over one data bit period. This decoding process is possible only if the local PRN is synchronized (locked) to the incoming code. This allows channel selectivity, which is an attractive feature for many applications, since it decodes data streams only from the synchronized PRN. In LISA, this selectivity is key to support full duplex data transmissions between satellites.

The optical receiver operates under low power conditions with a shot noise limited performance. As previously mentioned, the ranging signal is buried in the shot noise floor reference such that data errors in the bit transmissions are expected. For data error corrections, a well known Reed-Solomon (RS) encoding technique [74, 75] is applied to demonstrate the viability of reliable optical communications. To this end, a RS(n=15,k=9) scheme with m= 4-bit symbols has been implemented, where n corresponds to the code length and k refers to the data symbols per code. This includes (n-k) parity symbols over a raw data transfer of approximately 24 kbps, resulting in an effective data rate of 14.6 kbps. As shown latter in chapter 5, the data errors are fully corrected in the optical link with this configuration. From the point of view of the hardware implementation, the RS encoding can be implemented either into the FPGA or into a micro-controller. Throughout this thesis, the scheme is based on a FPGA development. Nonetheless, a new breadboard with an embedded micro-controller has been recently manufactured, and described in section 4.7. Further investigations will implement a RS encoding algorithm into the micro-controller, increasing the communication capability with intelligent data protocols.

The data decoding process is placed out of the DLL control loop, and requires two stages: a data bit synchronization and a RS decoding architecture [76, 77]. In order to verify this scheme, a long RS frame format is continuously transmitted at a raw bit rate of 24 kbps. Since the data sequences are strongly affected by bit errors, a bit alignment algorithm uses the RS decoder output to detect and correct a specific data pattern. A bit shifting process is used to align the input bit sequences for a successful decoding. This bit alignment process can be assisted by the PRN epoch time, since it is a well defined synchronization event. In the design of the optical data link, it is crucial that the receiver is capable of decoding the data streams without exceeding a maximum bit error rate (BER). As previously mentioned, the low light power conditions in LISA yield to a significant shot noise on the receiver signal that ultimately limits the sensitivity of the system. A commonly used metric for communication performance in coherent receivers is the power required to reach a bit-error ratio (BER) of 10^{-9} , which is calculated from the received optical power divided by the energy per photon and the data rate [13]. The receiver sensitivity is given by

$$\zeta_p = \frac{P_d}{h\nu \cdot DR} \approx 366 \quad [\text{photons/bit}], \quad (4.13)$$

where h is the Planck's constant (6.626×10^{-34} J.s), ν is the optical frequency, DR is the effective bit data rate (14.6 kbps), and $P_d \approx 1$ pW is the optical power. Coherent BPSK receivers can theoretically achieve a receiver sensitivity of 9 photons/bit [13]. However, this is referred to homodyne BPSK receivers. In LISA, heterodyne receivers are used, which result in a penalty of about 3 dB [13].



Open loop transfer function

$$G(z) = \frac{\hat{\tau}(z)}{\tau_e(z)}$$

System transfer function

$$H(z) = \frac{\hat{\tau}(z)}{\tau(z)} = \frac{G(z)}{1 + G(z)}$$

Error transfer function

$$E(z) = \frac{\tau_e(z)}{\tau(z)} = \frac{1}{1 + G(z)}$$

Figure 45: Linear model of the delay tracking loop.

4.6.5 Delay loop analysis: linear model

Here, a loop analysis of the first order DLL architecture is described. Figure 45 shows the linear model of the delay tracking loop. The dynamic range of the DLL in terms of Doppler shifts can be derived from section 3.7, i.e., for a line-of-sight velocity of $v_{\text{LOS}} \approx 20$ m/s, the frequency variation in the optical carrier ($\lambda \approx 1\mu\text{m}$) due to Doppler effect yields

$$f_D \approx \frac{v_{\text{LOS}}}{\lambda} \approx \pm 20 \text{ MHz}. \quad (4.14)$$

With an updating period in the DLL of $T_u \approx 1/1.5 \text{ kHz} \approx 655 \mu\text{s}$, the timing errors Δt due to frequency variations Δf within the optical carrier frequency ν are given by

$$|\Delta t| = \frac{f_D}{\nu} T_u \approx 32 \text{ ps}. \quad (4.15)$$

This means that optical pathlength delays do not change significantly over an updating period of the control loop. In other words, a pathlength change results in a time variation smaller than the DLL tracking range, which corresponds to one chip period ($\approx 1\mu\text{s} \gg 32 \text{ ps}$).

The digitized time-varying delay tracked by the DLL, and its time evolution Δt can be then written as

$$\begin{cases} \tau(0) = \tau_0 \\ \tau(n) = \tau(n-1) + \Delta t, \quad \forall n \geq 1. \end{cases} \quad (4.16)$$

After initial delay acquisition τ_0 , the DLL updates the estimated delay $\hat{\tau}(n)$ by using an increment of $i(n)$ in the DLL loop filter, which can be modeled as

$$\begin{cases} i(0) = 0 \\ i(n) = K_f \varepsilon(n-1) + i(n-1) \\ \varepsilon(n) = K_c [\tau(n) - \hat{\tau}(n)] \quad \forall n \geq 0 \end{cases} \quad (4.17)$$

where $\varepsilon(n)$ is the error signal (see figure 45). K_c is the delay detector gain. K_f is the loop filter gain. The loop filter transfer function is

$$D(z) = \frac{I(z)}{E(z)} = K_f \frac{z^{-1}}{1 - z^{-1}}, \quad (4.18)$$

and thus the system transfer function is given by

$$H(z) = \frac{G(z)}{1 + G(z)} = \frac{\frac{K_c K_f z^{-1}}{(1 - z^{-1})}}{1 + \frac{K_c K_f z^{-1}}{(1 - z^{-1})}} = \frac{K_c K_f z^{-1}}{(1 - z^{-1}) + K_c K_f z^{-1}}, \quad (4.19)$$

where $G(z)$ is to the open loop transfer function. Figure 46 and figure 47 show the open loop and the system transfer functions of the DLL. In a similar way to the PLL loop analysis, a white Gaussian noise was injected into the control loop as an input signal τ to compute the different DLL transfer functions by combining the spectral estimations of the measured time series $\hat{\tau}$ and τ_e . From the open loop transfer function, it can be observed that the designed feedback loop is stable, with a 90° phase margin. The loop behavior is externally controlled within the FPGA by setting the loop filter gain k_f . In the current implementation, the feedback error signal is updated at 24 kHz. For DLL readout, an out-of-loop down-sampling process computes a delay estimation from the feedback signal at a measurement rate of 1.5 kHz.

4.6.6 Delay measurements readout and estimation of the ranging accuracy

The DLL architecture provides a delay estimation $\hat{\tau}$ at 1.5 kHz, whereas the on-board computer expects a down-sampled measurement rate between 10 Hz and 3 Hz, corre-

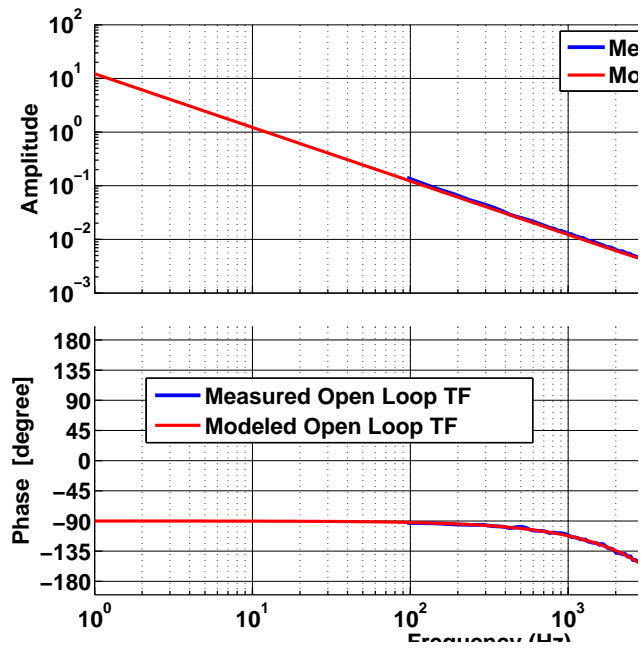


Figure 46: Frequency response for the DLL open loop transfer function.

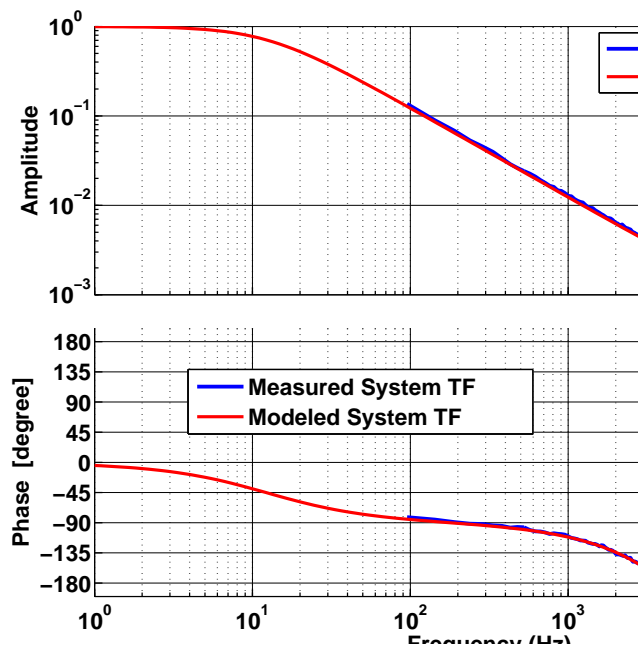


Figure 47: Frequency response diagram for the system transfer function.

sponding with the loop bandwidth. The delay readout consists of an averaging process of the feedback delay signal.

$$\hat{\tau} = \frac{T_u}{N} \cdot \sum_{n=1}^N \hat{\tau}[n] \quad [\text{sec}], \quad (4.20)$$

where N is the ratio between the DLL updating rate and the desired down-sampled measurement rate. The ranging accuracy in meters (scaled by the speed of light c) is determined as the rms value according to

$$\sigma(N) = c \cdot \sqrt{\frac{1}{M} \cdot \sum_{i=1}^M \left(\hat{\tau}_i - \tau_{\text{mean}} \right)^2} \quad [\text{m}], \quad (4.21)$$

where M indicates the number of points taken for computing the rms error from a given ranging measurement at the DLL output. As shown in section 4.8.4, the designed DLL provides ranging measurements with sub-meter rms noise in the loop bandwidth for representative LISA-like conditions.

4.6.7 Theoretical ranging accuracy limit

The main limiting factor to be considered for the estimation of the ranging accuracy is the width of the correlation peak. The ranging accuracy improves by increasing the chipping rate, i.e., narrowing the correlation peak. However, the beat note frequency range limits the chip rate to less than 2 MHz, since the frequency range is typically in the range of 2 MHz to 20 MHz. For a designed code rate of 1.5 MHz, the fundamental limit for the ranging accuracy is then given by shot noise. As shown in equation 4.22, an estimate of the rms ranging errors is mainly determined by two parameters [61]: the carrier to noise power density ratio (C/N_0) and the bandwidth of the code tracking loop.

$$\sigma_{\text{DLL}} \approx c \cdot T_c \sqrt{\frac{B_n}{C/N_0}} \quad [\text{meters}], \quad (4.22)$$

where c is the speed of light. T_c refers to the chipping period (1/1.5 MHz). A loop bandwidth (B_n) between 3 and 10 Hz is chosen due to the ranging measurement rates to the on-board computer. The C/N_0 is estimated by computing the linear-spectral density (LSD) of the shot noise contribution in the received photocurrent. Assuming LISA-like values, i.e., a local oscillator optical power $P_{\text{LO}} \approx 1$ mW a signal power for ranging $P_s \approx 1$ pW, a photodiode responsivity of 0.7 [A/W] and a heterodyne efficiency of ≈ 0.7 .

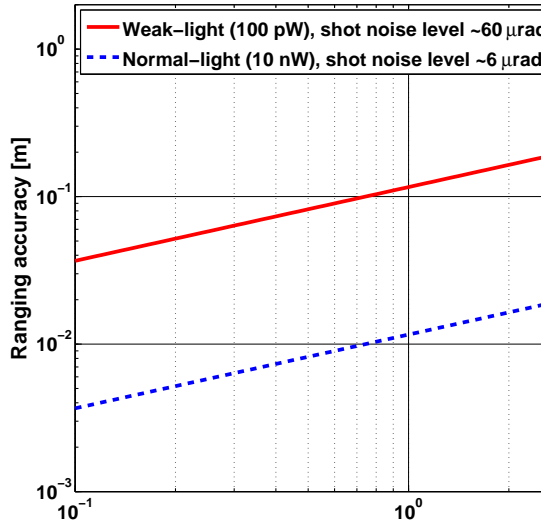


Figure 48: Theoretical ranging rms noise for two different shot noise levels.

The rms amplitude of the main beat note is given by:

$$bn_{rms} = 2\rho \cdot \sqrt{P_{LO}P_s\gamma} \cdot \frac{1}{\sqrt{2}} \approx 25 \text{ nA}. \quad (4.23)$$

The equivalent LSD of the photocurrent shot noise is:

$$sn = \sqrt{2q_e\rho P_{LO}} \approx 15 \text{ pA}/\sqrt{\text{Hz}}. \quad (4.24)$$

Thus, the resulting carrier to noise power density ratio (C/N_0)

$$C/N_0 \rightarrow \left(\frac{bn_{rms}}{sn} \right)^2 = \frac{\rho P_s \gamma}{q_e} \approx 3 \times 10^6 \text{ Hz} \rightarrow C/N_0 \approx 64 \text{ [dBHz]}. \quad (4.25)$$

Figure 48 shows the theoretical rms tracking error as a function of the code loop bandwidth. Note that the ranging accuracy is limited by shot noise to approximately 40 cm at 10 Hz. For comparison with experimental results see section 4.8.4 (electrical environment) and section 5.2.1 (optical environment). Ranging errors by cross-correlation between the codes and data encoding are not taken into account. The impact of these errors were electrically measured in section 4.8.4 and optically verified in chapter 5.

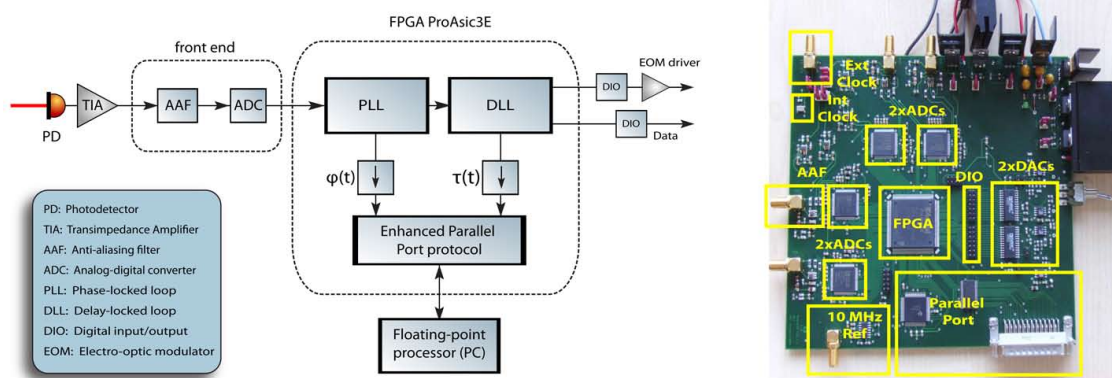


Figure 49: Photograph of a custom-designed breadboard currently used for performance investigation on phasemeter and ranging architectures. It provides four analog-to-digital (ADC) input channels, two digital-to-analog (DAC) output channels, and space-compatible FPGA processors.

4.7 FPGA-BASED CUSTOM-DESIGNED BREADBOARD

A versatile breadboard with four independent channels has been developed as a joint effort in the team at the AEI to support investigations such as phasemeter performance, ranging measurements and clock noise transfer. Figure 49 shows a photograph of this breadboard. In contrast to hard-wired analog-based implementations, a digital development makes it possible to update the firmware through re-programming the embedded FPGA, enabling the design of a versatile platform for many different purposes. It also has the ability to adapt the behavior of control loops in real-time, changing for example the loop bandwidth of the synchronization loops under different signal conditions. The main characteristics of this breadboard are:

- Four A/D-converters (AD9446-100) with 16-bit resolution. This allows independent phase measurements for each segment of a quadrant photoreceiver.
- Two D/A-converters (AD9744-210) with 14-bit resolution. The D/A converters (AD9744) can be used for laser control by controlling an analog actuator (piezo/temperature), as well as for PRN modulation by using an electro-optical modulator (EOM).
- Re-programmable ProAsic3E Actel FPGA with up to 3 Million system gates and with 147 high-performance digital inputs/outputs (I/Os).

- The prototype integrates a quartz clock running at 50 MHz that drives the ADCs, DACs and the FPGA. Alternatively, an external clock reference can be used via an external port to increase the sampling frequency up to 100 MHz.
- Enhanced parallel port (EPP) with an output rate up to approximately 200 kbps used for data readout.
- High-speed PCI digital input/output (DIO) board with direct memory access features a maximal rate of 2 GB/s that is useful for debugging purposes.

A new breadboard has been recently manufactured and is currently under electrical testing. This prototype is shown in figure 50. The new features with respect to the previous breadboard are:

- LPC 3250 OEM microcontroller board (Embedded Artists AB) that contains a LPC 3250 microcontroller (NXP Semiconductors) with Vector Floating Point (VFP) co-processor. This board is running at frequencies up to 266 MHz. It enables the development of advanced ranging capabilities, including smart code acquisition algorithms and enhanced data transmission protocols. For communication between the FPGA and the micro-controller, two interfaces can be used: Serial Peripheral Interface (SPI) and memory mapped input-output. The programming of the micro-controller board is performed through the USB/UART bridge connected to a computer.
- For data readout, two additional Universal Serial Bus (USB) ports were implemented. One is connected to the micro-controller and a second one to the FPGA. It replaces the EPP interface, which is nowadays obsolete. The USB ports increase the data readout capability for debugging.

4.8 ELECTRICAL TESTING

A digital signal synthesizer (DSS) has been developed for testing the performance of the designed metrology architecture: phase measurements at picometer accuracies and absolute ranging estimations at sub-meter resolution. The DSS generates representative electrical signals of the photodiode outputs in the LISA interferometry system. There are no commercial breadboards available for these purposes. Therefore, we have developed a versatile DSS platform based on a field-programmable gate array (FPGA) processor. In contrast to an optical test-bed (presented in the following chapter), the DSS is a compact electrical platform that provides easily controllable signal levels, frequency variations, modulation depths, able to mimic the expected signals and noise sources. The DSS enables the design of beat note signals with high phase fidelity, which is typically difficult to obtain in optical laboratory conditions due to the couplings of

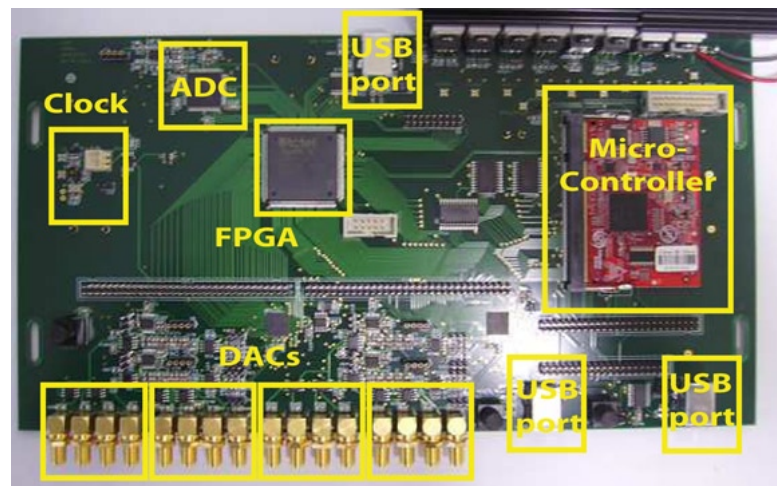


Figure 50: Photograph of a recent digital breadboard that incorporates micro-processor capabilities and enhanced interface communication based on a universal Serial Bus (USB).

real optical displacements, pressure changes and temperature fluctuations. Therefore, the goal of the DSS is to support the implementation and testing procedures with well-controlled and representative input signals. In addition, it is re-programmable with full signal visibility for debugging and it can be re-configured in case of future capabilities.

Four main tests were performed using a DSS prototype. The main goals were to verify functionality and performance of the phasemeter and ranging system: the first test was the PRN impact on the phase performance of the main beat note carrier. Secondly, the multi-tracking capability of the phasemeter by measuring the upper and lower clock noise sidebands as well as the achievable clock noise performance. Thirdly, the loop dynamics of the ranging system under fast time-delay variations. Finally a preliminary estimation of the achievable performance for ranging and data communication. All of them are discussed in the following sections.

4.8.1 Phasemeter performance with PRN modulation

PRN modulation spreads the carrier power over a large frequency range, causing fast phase transitions with an amplitude variation proportional to the modulation depth. In contrast to standard ranging methods, the proposed metrology system uses a low-depth PRN modulation scheme in order to reduce both optical power allocated to the PRN modulation and residual carrier phase noise due to fast PRN transitions. In order to assess the impact of the ranging system in the phase stability of the main science measurements, the phasemeter performance was tested at different PRN modulation depths.

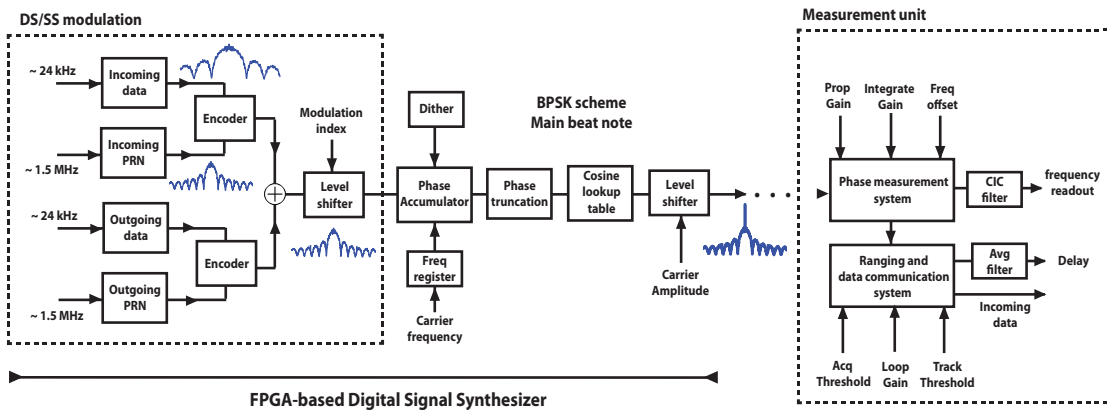


Figure 51: Block diagram of the measurement set-up for testing the PRN impact on the phasemeter performance.

Figure 51 illustrates the measurement set-up. A FPGA-based signal generator was used to produce a LISA-like signal with two data-encoded PRN sequences, providing the input signal for the phasemeter and the ranging system. The electrical spectrum of the phasemeter input signals and the noise spectral density of the resultant measurements are shown in figure 52. The phasemeter measurements were subtracted from a nominal phase at a constant heterodyne frequency, such that the differential phase noise due to PRN modulation could be measured. The phase noise of the instrument is limited by a dithering effect as explained in section 4.6.1.

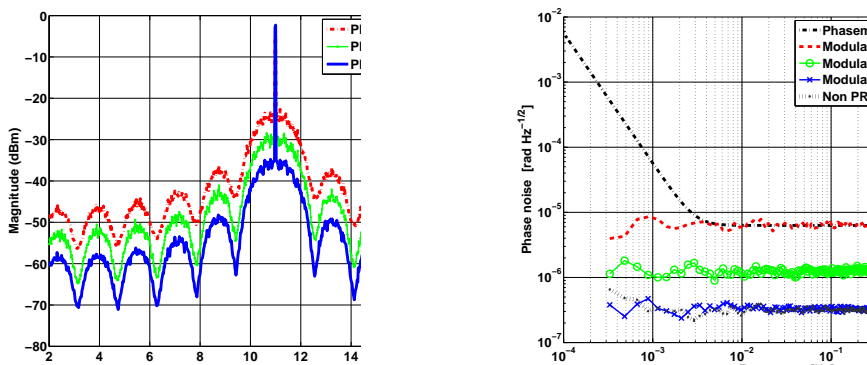


Figure 52: (Left side) Electrical spectrum of the phasemeter input signal at different modulation depths. (Right side) Noise power spectral density comparing the impact of different PRN modulation depths in the phasemeter performance. The measurements modulate two PRN sequences (local and remote pseudo-codes) encoded with data streams at 24.4 kbps.

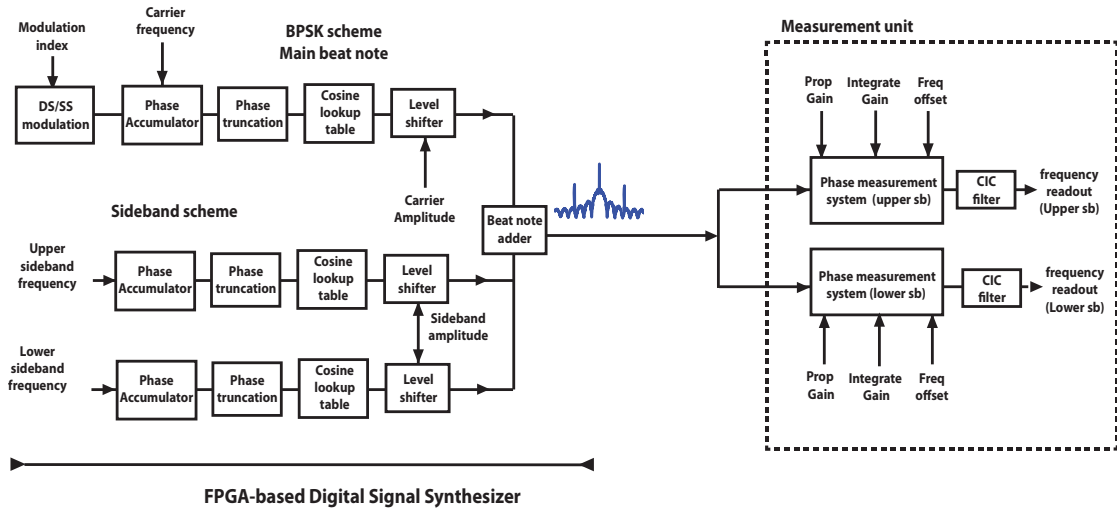


Figure 53: Block diagram of the measurement set-up for testing clock sideband performance.

For the designed DPLL architecture with a bandwidth of about 250 kHz, the residual phase noise produced by PRN modulation was successfully suppressed. The overall phasemeter performance reached levels below $1 \text{ pm}/\sqrt{\text{Hz}}$ in the mHz band for modulation depths below $\pi/8 \approx 0.4 \text{ rad}$. By applying modulation depths of the order of $\pi/32 \approx 0.1 \text{ rad}$, that correspond to an equivalent light power below 1%, the PRN modulation produced a broadband phase noise about one order of magnitude below the required phase fidelity for LISA.

4.8.2 Clock noise performance

As previously described, clock sidebands are phase modulated at 2 GHz onto each optical carrier for measuring the relative phase noise of the on-board clocks. Upon interference of the laser beams on the optical bench, the output of the photoreceiver shows an electrical signal spectrum with three beat notes. Two sideband-to-sideband beat notes from the clock modulation and the carrier-to-carrier beat note. The clock beat notes differ in two aspects with respect to the main carrier tracking: firstly, for an optical sideband modulation of 2 GHz, the phase noise performance is relaxed by a factor of $2 \text{ GHz}/20 \text{ MHz} = 100$. Secondly, for a modulation index of $m_{sb} \approx 0.5 \text{ rad}$, i.e., by using 10% of the optical carrier power, the sideband-to-sideband beat notes suffer from a high shot noise level since their power is $\approx 24 \text{ dB}$ lower than the main science beat note. In order to verify the functionality and noise performance of the clock sideband modulation scheme, the signal synthesizer was configured to generate the clock sidebands (see figure 53). Two independent phasemeter architectures were used for clock noise readout in presence of ranging signals.

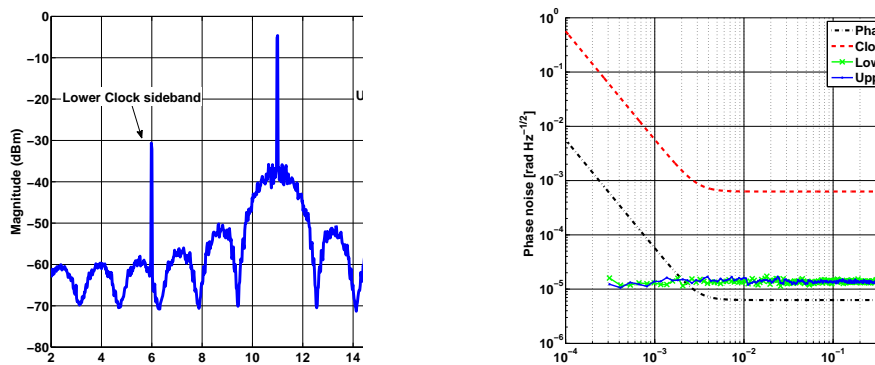


Figure 54: (Left side) Electrical spectrum of the phasemeter input signal with three different tone signals. (Right side) Noise power spectral density comparing the phasemeter noise performance for both the upper and lower clock tone sidebands.

Figure 54 shows the electrical spectrum of the phasemeter input signal and the phase noise spectral density for both the upper and lower clock tone sidebands. The measurement shows a flat noise floor over the whole frequency range, limited by strong power suppression on the clock sidebands. Although the clock noise performance is below LISA requirements, the spikes at high frequencies are currently subject of investigations, most probably being caused by non-optimal filtering of higher harmonics in the feedback control. In order to suppress those peaks, the control loop was modified to include a set of two averaging filters with a cut frequency of approximately 3 MHz.

4.8.3 Time-varying code tracking

The capability of the ranging architecture for tracking time-varying PRN codes was electrically tested by adding sinusoidal increments of the delay. This way, a delay function given by $\tau(t) = \tau_0 \cdot \cos(\omega t)$ was added to the code tracked. It mimics the two directions of the satellite motion (back and forth). Note that the relative inter-spacecraft velocity is equivalent to the time derivative of the delay function. Thus, the stability region in which the designed system is able to track a varying code depends on the product between the magnitude, τ_0 , and the angular frequency, ω . As shown in the DLL control loop analysis of section 4.6.5, the DLL was designed with a high loop dynamics to allow future investigations on optimal readout filtering. Figure 55 shows the DLL tracking capabilities of a fast delay function prior to down-sampling, i.e., with an updating rate of 1.5 kHz. In order to perform this FPGA-based measurement, a nominal delay function with a constant delay step of 20 ns (6 m), (limited by the sampling frequency) is added into the DLL control loop. Thus, the measured delay follows the nominal variations for equivalent inter-spacecraft velocity of about thousand meters per second. In LISA, the expected delay variations due to satellite motion is in

the order of $\pm 20\text{m/s}$. Figure 56 shows LISA-like delay variations, in which the raw DLL measurements were down-sampled to 10 Hz as expected by the on-board computer.

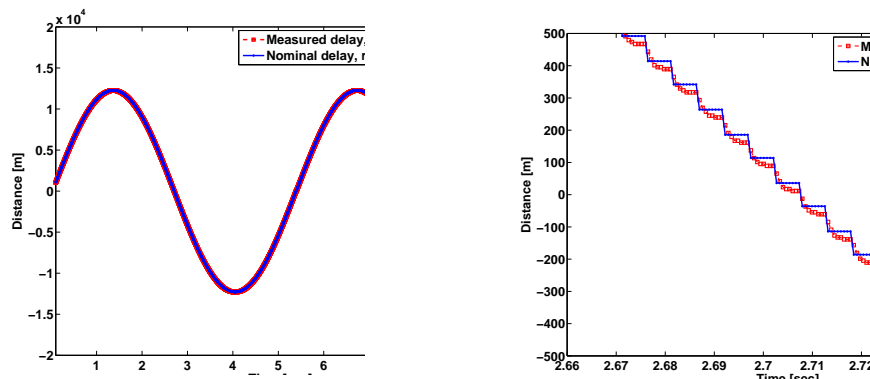


Figure 55: Delay-locked loop (DLL) tracking capabilities of fast time delay variation with an equivalent inter-satellite velocity of several thousand of meter per second.

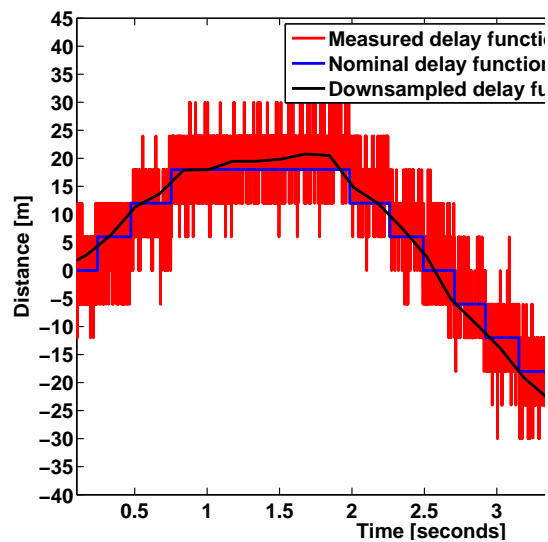


Figure 56: Delay-locked loop (DLL) tracking capabilities of slowly varying code delays with equivalent inter-satellite velocities of $\pm 25\text{m/s}$.

4.8.4 Ranging accuracy and bit data errors

The measurement set-up for testing the ranging accuracy and data bit errors is based on the previously presented configuration shown in figure 51. Two additional features were implemented into the FPGA: code timing variation on both PRN sequences and additive white Gaussian noise (AWGN). The AWGN generators aim to simulate shot noise, and it is added to the output signal amplitude. A true Gaussian noise distribution

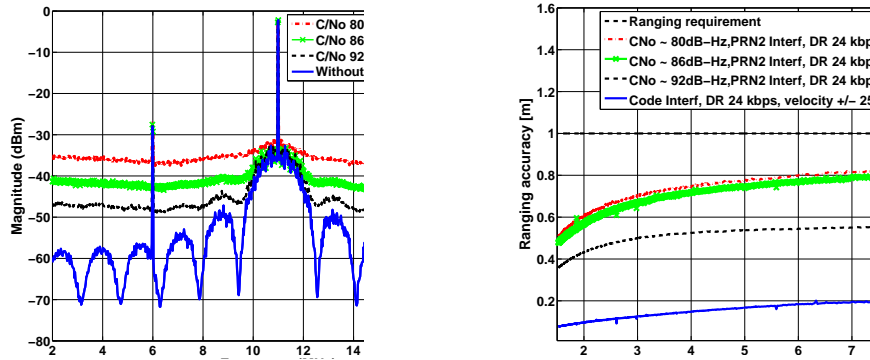


Figure 57: (Left side) Electrical spectral of the generated input signal under different Additive white Gaussian noise (AWGN) environments. (Right side) measured ranging accuracies. The ranging errors included AWGN noise, code interference, encoded data and delay variations with equivalent satellite motion at ± 25 m/s.

is difficult to implement in a FPGA, and it would also require a high computation load. Therefore, similar to the dither noise generators, a triangular noise distribution was generated by adding two uniform random noise generators. For a AWGN distribution, the resulting spectral density at the output of the DSS presents a constant background noise. Figure 57 (left side) shows the output spectrum of the generated signal under different AWGN levels. In LISA, the expected carrier-to-noise density ratio (C/N_0) is about 86 dB-Hz, which is obtained by computing equation 4.25 for an optical power of $P_s \approx 100$ pW.

Table 4: Ranging accuracies and bit error rates for different AWGN noise levels.

Carrier-to- noise ratio			Ranging rms noise		Bit Error Rate (BER)
Carrier	Noise density	C/N_0	10 Hz	3 Hz	Raw data at 24 kbps
-2 dBm	-82 dBm/Hz	80 dB-Hz	84 cm	50 cm	$< 26 \times 10^{-3}$
-2 dBm	-88 dBm/Hz	86 dB-Hz	82 cm	50 cm	$< 1 \times 10^{-3}$
-2 dBm	-94 dBm/Hz	92 dB-Hz	58 cm	38 cm	Not error detected

Figure 57 (right side) shows the measured ranging accuracies. The proposed architecture achieves sub-meter accuracies under high AWGN environments (80 dB-Hz). The ranging signal was generated by including a time-varying outgoing code interference, data rate at 24 kbps and delay variations with an equivalent satellite velocity of 25 m/s.

Table 4 summarizes the signal levels measured by a spectrum analyzer and the ranging and bit errors rates obtained at the output of the metrology system. As expected for

high AWGN environments, the raw data transmitted presents bit error rates (BER) up to 26×10^{-3} . In order to detect and correct bit errors in the raw data, a forward error correction (FEC) technique based on Reed Solomon encoding has been implemented and the results are shown in chapter 5. The bit errors were fully corrected allowing highly reliable optical data communications.

4.9 SUMMARY

This chapter describes the hardware configuration of the digital feedback control loops implemented for interferometric phase readout and ranging measurements. Two main architectures were developed based on a phase-locked loop (PLL) and a delay-locked loop (DLL). These architectures have been programmed on a FPGA processor. The PLL allows advanced capabilities in the metrology system such as clock noise transfer, whereas the DLL architecture additionally performs data communications. The performance of these digital control loops was evaluated with representative LISA-like noise signals. To this end, a custom-designed digital signal synthesizer (DSS) was built as electrical test bed to provide the input signal for the phasemeter and the ranging system. Experimental results fulfilled all requirements with margin, thus validating the metrology concept.

OPTICAL DEMONSTRATION OF LASER RANGING AND DATA TRANSFER

In this chapter an experimental demonstration of optical operation for the proposed laser ranging and data communication scheme is presented. A test-bed based on a Mach-Zehnder interferometer with a low-depth phase modulation scheme was built to provide representative LISA-like signals under a coherent transponder configuration. Due to the stringent requirements of the mission, the ranging scheme requires an experimental verification at picowatt optical power levels, and a ranging accuracy at sub-meter resolution with a highly reliable optical data communications. This weak-light environment combined with precision ranging measurements needs to be demonstrated under signal dynamics and strong interferences. The system dynamics performance was verified tracking a time-varying ranging signal following a simulated orbital motion. On the other hand, the signal interferences in the metrology system due to a side-effect of the auxiliary laser link capabilities i.e., adjacent sideband-to-sideband beat notes close in frequency to the main carrier-to-carrier beat note for clock noise transfer, and the inter-code correlation noise given by a bidirectional ranging scheme, were included in the experimental setup by means of additional phase modulations onto the laser link. Under these conditions, the designed delay-locked loop (DLL) architecture achieves a noise level of 42 cm for an output rate of 3 Hz for data transmissions at 24 kbps.

The experimental setup for testing laser ranging and data communications is presented in section 5.1. Section 5.2 shows the measured ranging performance and the dominant noise sources on the optical bed, verifying the previous noise models and the previous ranging performance achieved in electrical conditions. Section 5.3 shows the optical performance achieved by the clock noise transfer scheme in the presence of PRN ranging, verifying that the ranging system can be integrated with this scheme without degrading its performance. Section 5.4 presents the future test plan to demonstrate optical phase readout at picometer accuracy in the mHz frequency band in combination with the auxiliary functions for three laser links. This test plan will enable on-ground testing of time-delay interferometry (TDI) requirements [58].

5.1 EXPERIMENTAL SETUP

The low-light power available for ranging and data communications ¹ (1 pW) yields a ranging signal below the shot noise level, limiting the ranging accuracy and significantly increasing the data errors for optical communication. In order to demonstrate a ranging performance at sub-meter accuracy with reliable data communication, a heterodyne interferometer was built under a weak-light environment. Figure 58 shows a schematic diagram of the experimental setup. Two NPRO lasers were used as continuous light sources at 1064 nm. In each laser, two built-in control ports enable analog actuation of both the temperature of the crystal and its resonator geometry (piezo transducer) to control the output laser frequency. The temperature actuator with a thermal tuning coefficient of -3 GHz/K provides a tuning range up to 30 GHz for coarse laser control. The piezo actuator with a range up to ± 100 MHz leads to a finer tuning coefficient of 2 MHz/V. Through these frequency actuators, a weak-light laser offset phase locking method generated the heterodyne beat signal between the two lasers, denoted as master (received/incoming) and slave (local/outgoing). In order to implement offset-laser phase locking, the phase of the slave laser was tightly maintained to the free-running master one. This way, high-bandwidth (from kHz-MHz) phase measurements of the main beat note were used as feedback signal, after its optical sensing by a low-noise InGaAs photodetector pre-amplifier. The schematic electronic circuits for offset phase locking and the photoreceiver are attached in appendix E.1. In order to provide phase modulation capability in the experimental setup, both lasers were linearly polarized and isolated from back-reflected light before being coupled into a fiber-coupled electro-optic modulator (EOM). The EOM was driven with data-encoded PRN signals and clock sidebands at 2 GHz using 1% and 10% of the optical carrier power respectively. The PRN modulation onto the local laser was also included, through a phase modulation of a different pseudo-noise sequence, to provide the spurious interfering code that is a side-effect of the bidirectional ranging scheme. In order to reduce the optical power to 100 pW, a set of neutral gray filters were used to drastically decrease the power level of the master laser before interfering on the optical bench. The resulting heterodyne signal in the MHz range at the output of the photoreceiver was then digitized and processed in breadboard presented in section 4.7 for interferometric phase readout and ranging measurements.

The experimental setup was designed to provide two main features: a low-light power environment and a low-depth modulation index. Both features are analyzed in the following sections.

¹ Before laser interference in a 50:50 beam splitter, the optical power of the received beam is approximately 200 pW. After interference, the incident power at the photoreceiver is reduced to 100 pW. Only 1% of this optical power (1 pW) is used for laser ranging and data communications.

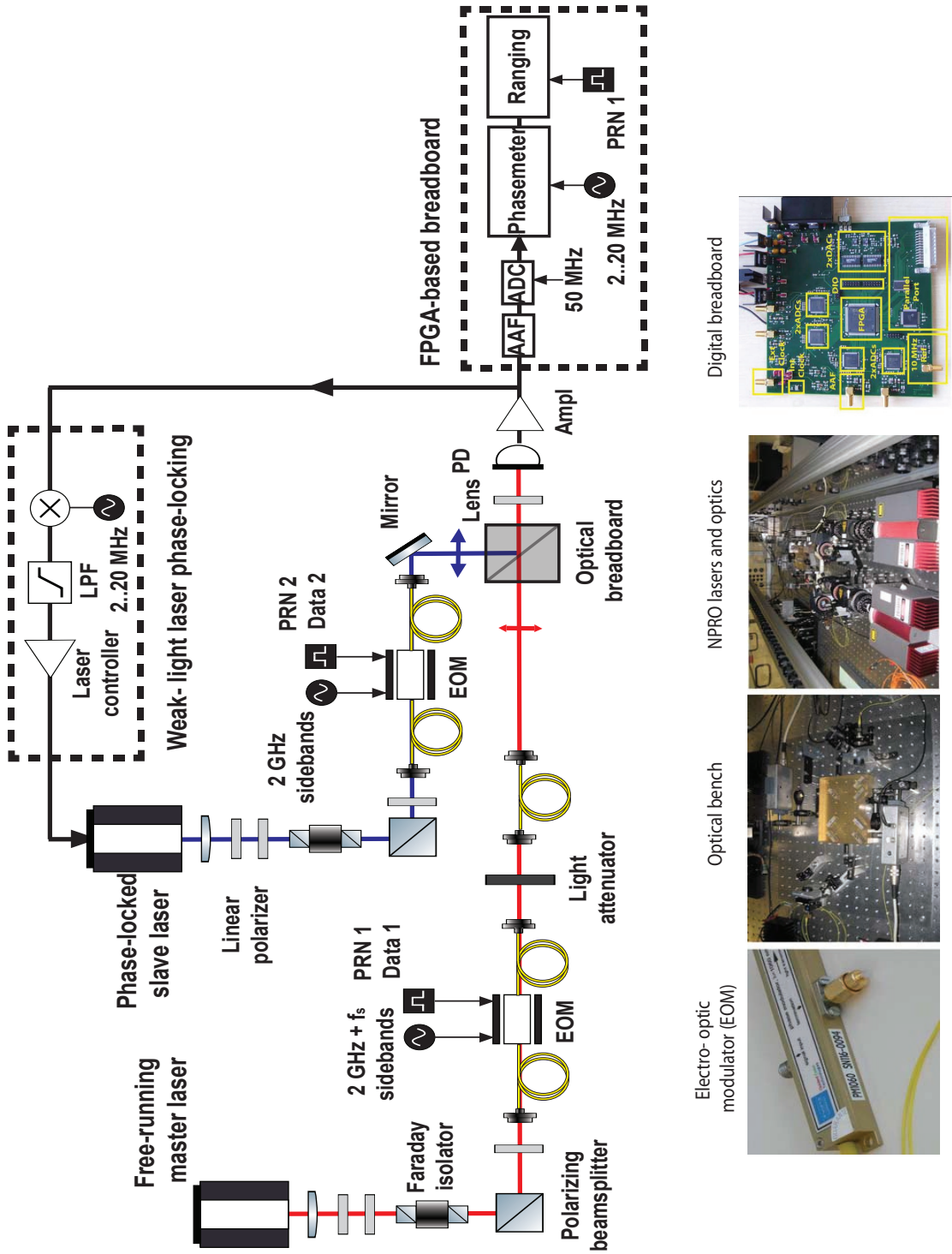


Figure 58: General schematic of the experimental setup built to test ranging and data communications performance.

5.1.1 Low-depth phase modulation

Two fiber-coupled high-frequency (GHz) EOMs [78] were used for low-depth phase modulations of clock tone sidebands and PRN ranging signals. Each EOM consists of a Lithium niobate (LiNbO_3) crystal whose refractive index, and therefore its optical path length, is a linear function of the strength of the local electric field. Hence, by applying a varying RF drive voltage, the phase of the transmitted beam causes a change directly proportional to voltage applied, enabling a linear phase modulation of a laser at the same frequency as the modulating signal. The used EOM is of the waveguide type to achieve very broadband performance and was experimentally characterized in an AEI diploma thesis [79], and also described in [33]. For the clock sidebands, a function generator was used to modulate the master laser with a sinusoidal tone at a nominal frequency of $f_m = 2 \text{ GHz}$. The slave laser was phase modulated using a second function generator with a reference tone oscillating at a frequency of $f_{\text{ref}} = 2 \text{ GHz} + f_{\text{sp}}$, where f_{sp} corresponds with the frequency spacing between both clock sidebands and the main carrier beat note. Therefore, the resulting sidebands at the output of the photoreceiver show up as two tone signals oscillating at $f_{\text{lower}} \equiv f_{\text{het}} - f_{\text{sp}}$, and $f_{\text{upper}} \equiv f_{\text{het}} + f_{\text{sp}}$ over the Doppler-affected beat note frequency band between $2 \text{ MHz} \leq f_{\text{het}} \pm f_{\text{sp}} \leq 20 \text{ MHz}$.

For laser ranging, a FPGA-based code generators was designed to modulate the data-encoded PRN sequences. As described in the design parameters of the ranging signal in section 4.6.3, a PRN sequence running at 1.5 MHz is encoded with a data stream at 24 Kbps. The data-encoded PRN codes were digitally generated by a FPGA-based breadboard (see section 4.7) running at 50 MHz (time resolution of 20 ns). A custom-designed EOM driver was designed for PRN phase modulation onto the laser carrier. The schematic of the EOM driver is attached in appendix E.1. It converts a CVMOS (3.3 V) digital output signal into a proportional voltage with adjustable gain. The adjustable output amplitude voltage enables a fine tuning of the PRN modulation depth. A rms PRN signal of about 200 mV is applied as RF drive voltage to the EOM, which corresponds with a modulation index of 0.1 rad or equally with about 1% of the optical carrier power.

5.1.2 Weak-light conditions

The optical power of the master laser is reduced by two-stages. Firstly by using the leakage field through a polarizing beam-splitter before light coupling in the EOM's fibers. Thereby, the output power of the laser system at 500 mW is reduced to a few mW (2 mW in the current setup), adjusting the optical modulators to an operation point with an appropriate beam power. A second stage is used for attenuation of the master laser to 200 pW with a large attenuation factor of $\frac{200 \text{ pW}}{2 \text{ mW}} = 1 \times 10^{-7}$. To this end, the modulated beam is decoupled from the fiber, and its optical power drastically reduced

by using a set of neutral gray filters. In addition, a more accurate adjustment of the optical power is accomplished through a controlled misalignment in the beam pointing before re-coupling into a second fiber. This way, the fiber is also used as bridge between the optical attenuator and the Mach-Zehnder interferometer in order to minimize the beam distortion within the optical bench. A beam splitter with 50:50 coating is used for interfering the master laser ($P_M = 200$ pW) with the local laser ($P_{LO} = 2$ mW). Note that at the output port of the beam splitter, the optical power of the master laser is reduced to 100 pW, which is the incident power of the master laser at the photoreceiver.

In weak-light conditions, the quality of the beam interference was measured in terms of optical field distributions at the photodiode surface, i.e., by measuring the heterodyne efficiency, γ (see appendix A.1). After a carefully alignment between the master beam and the LO beam in the optical bench for precise recombination, the heterodyne efficiency was then computed by measuring the contrast k in the experiment under equal power conditions ($P_M = P_{LO}$), i.e., by computing the AC amplitude of the beat signal divided by the mean power:

$$k = \frac{\overbrace{\frac{\sqrt{P_M P_{LO} \gamma}}{P_M + P_{LO}}}}{\text{AC beat note}}}{2}, \quad \text{such that} \quad \begin{cases} k = \sqrt{\gamma}, & \text{if } P_M = P_{LO}; \\ k = 2\sqrt{\frac{P_M}{P_{LO}}} \sqrt{\gamma}, & \text{if } P_M \ll P_{LO}; \end{cases} \quad (5.1)$$

This way, the heterodyne efficiency is measured as $k = \sqrt{\gamma}$. When the optical power of the master laser is drastically attenuated to reach weak-light conditions $P_M \ll P_{LO}$, the contrast differs from the heterodyne efficiency by a scaling factor depending on the relative power ($k = 2\sqrt{P_M/P_{LO}\gamma}$). Consequently, the contrast decreases whereas the magnitude of the heterodyne efficiency can be assumed invariant. Thus, γ is a more suitable estimator of the signal quality in weak-light coherent detectors since it only depends on the overlap between phase-fronts.

At picowatt levels, the master laser cannot be directly measured by a power meter. Therefore, the optical power of the master laser is inferred from the signal amplitude of the main beat note at the output of the photoreceiver. As derived from chapter 3, the designed photo-voltage at a single-element photoreceiver ($N = 1$) is given by

$$V(t) = \underbrace{\eta g R \sqrt{P_M P_{LO} \gamma}}_{\Lambda_c} \cos \psi(t) + n(t) \quad [\text{V}], \quad (5.2)$$

where R is the transimpedance resistance, designed at 5.11 k Ω , which corresponds to the feedback resistor of a low-noise operational amplifier in an inverting configuration

(see schematics in appendix E.1), g is the gain of a second stage in the photoreceiver, designed to 8.2, η is the responsivity of the photodetector (0.7 [A/W]) for a wavelength of 1064 nm, γ is the heterodyne efficiency, it was experimentally measured to ≈ 0.7 , P_{LO} is the optical power of the local beam at the input port of the beam-splitter, adjusted at 2 mW, and P_M is the optical power of the master beam to be determined. Taking these parameters into account and for a required power of $P_M = 200$ pW, the resulting electrical power at the output of the photoreceiver is approximately -27 dBm.

Figure 59 shows a comparison between the spectrum measured at the output of the photoreceiver in weak-light conditions and the modeled spectrum described previously in section 4.5. This way, the signal model with an equivalent modulation index of 0.1 rad for ranging and 0.5 rad for clock sidebands complies with the laboratory measurements. The ranging signal is below the shot noise level and spread over a bandwidth of $B_w \approx 20$ MHz. For 1 pW of optical power level, the carrier-power-to-noise density ratio of the ranging signal is $C/N_0 \approx 64$ dB-Hz, and therefore it results in a signal-to-noise ratio (SNR) of -9 dB. Figure 60 shows the different noise contributions at the output of the photoreceiver. In the beat note frequency band (MHz), the noise floor of the experiment is dominated by shot noise from the laser light for frequencies above 7 MHz with a level of -111 dBm/Hz and by laser intensity noise at lower frequencies. The expected shot noise level is computed based on a previous calculation given in chapter 3 (equation 3.3). Thus, the linear spectral density (LSD) of the shot noise in the photo-voltage for a single-element photoreceiver is given by

$$\tilde{v}_{sn}(f) = g R \sqrt{q_e \eta P_{LO}} \approx 627 \frac{\text{nV}}{\sqrt{\text{Hz}}} \rightarrow 10 \log \left(\frac{\tilde{v}_{sn}^2(f)}{1 \text{ mW} \cdot 50 \Omega} \right) = -111 \frac{\text{dBm}}{\text{Hz}} \quad (5.3)$$

where q_e is the electron charge (1.602×10^{-19} C). Instrumental noise such as dark photo-voltage in the detectors, and the spectrum analyzer noise floor were also measured and shown in figure 60. Note that the photoreceiver presents an oscillation at ≈ 15 MHz with an amplitude of 40 μ V (15 dB below the upper clock sideband). At this amplitude level, the peak, which is probably caused by electromagnetic coupling from the laboratory environment can be consider as noise, and assumed as negligible in the realization of this experiment. Due to the relaxation oscillation [80] of the NPRO lasers, a sharp peak at about 1 MHz produces an excess laser intensity noise spreads over the frequency band from ≈ 100 kHz to 7 MHz, decreasing at higher frequencies as was shown in figure 16 from section 3.4.1. This type of lasers were experimentally characterized at the AEI PhD thesis [80], and also described in [81] given their relevance for LISA and on-ground GW detectors. In order to reduce the influence of the relaxation oscillation, the laser systems implements a built-in power pre-stabilization technique so-called Noise Eater. Activating this feedback loop, the intensity fluctuations in the laser beam

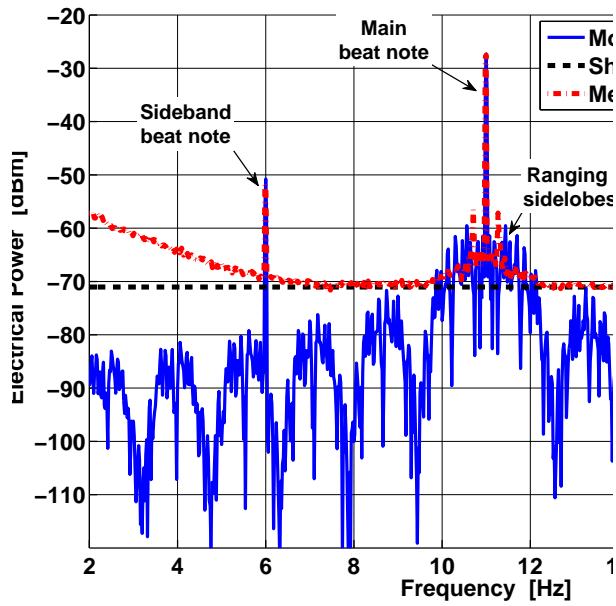


Figure 59: Spectrum comparison between the modeled signal spectrum at the output of the photoreceiver and the measured spectrum in weak-light conditions.

are suppressed around the oscillation peak. As drawback, the laser intensity noise level increases up to 5 dB in the frequency range between 2 MHz to 6 MHz. Throughout the realization of the ranging experiment, and for a beat note around 2 MHz, it was observed that the combination of both the excess laser intensity noise (lower SNR, consequently higher phase noise) and the strong relaxation oscillation signal produce a loss of lock of the laser offset phase-locking when the Noise Eater is deactivated. Therefore, the Noise Eater was activated in the realization of this experiment.

5.2 OPTICAL MEASUREMENTS IN WEAK-LIGHT CONDITIONS

The auto-correlation function at the output of the delay-locked loop (DLL) was measured in weak-light conditions and is represented in figure 61. The left plot shows a comparison of the measured auto-correlation function during delay acquisition under different code-scanning time resolutions. The right plot shows a zoom around the correlation peak to distinguish the magnitude of the auto-correlation and to show the delay averaging for different time resolutions. With a time resolution of 640 ns (equivalent to 192 m), i.e., one chip period for a PRN running at $50 \text{ MHz}/32 \approx 1.56 \text{ MHz}$, the code acquisition requires 0.67 seconds for scanning all possible delay over the full-code period (1024 chips). For this step size, in the worst case, the auto-correlation peak presents about 37% of amplitude losses with respect to the highest possible time resolution, i.e., 20 ns (6 m).

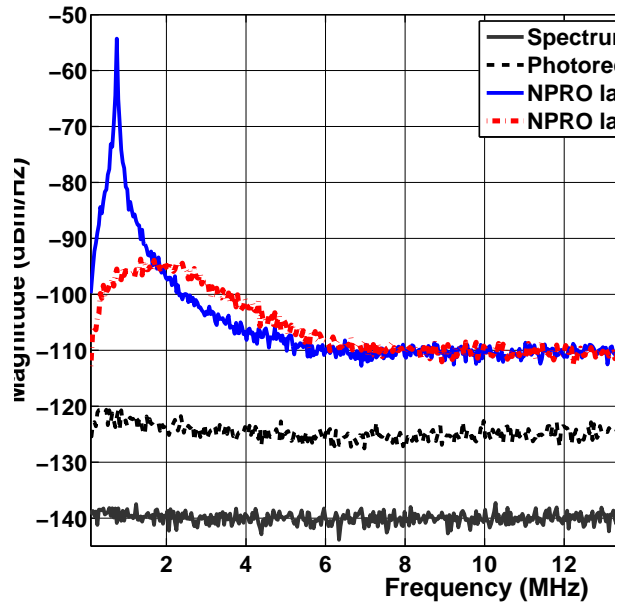


Figure 60: Measured noise contribution of the spectrum analyzer, photoreceiver and laser intensity noise in the relevant beat note frequency (MHz) range. The linear spectral density of the laser intensity noise without Noise Eater pre-stabilization activated is shown for comparison, since throughout the realization of this experiment the Noise Eater was activated.

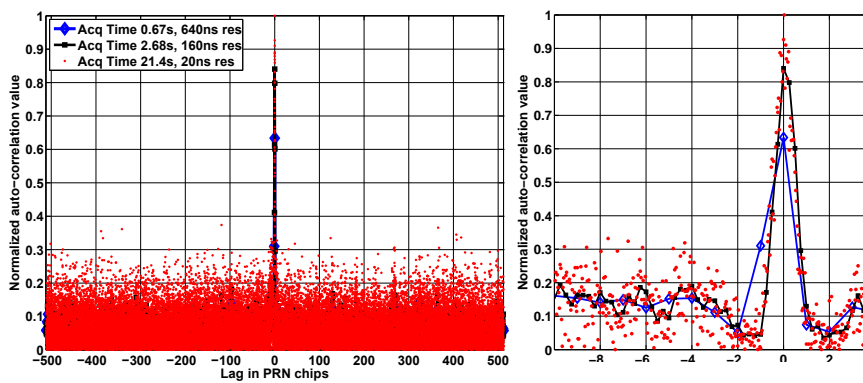


Figure 61: Left side: normalized auto-correlation function measured for different delay resolutions in the code-acquisition mode. Right side: it shows a zoom around the acquisition peak.

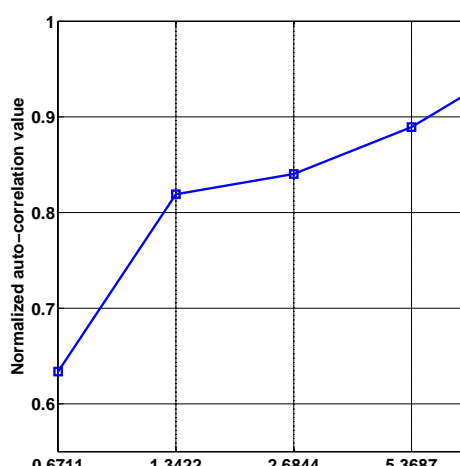


Figure 62: Auto-correlation peak amplitude for different acquisition times.

Figure 62 shows the resulting amplitude peak losses for different acquisition times. In order to reduce FPGA computational burden, time resolution on integer steps of two's powers were used for code acquisition. At the maximum resolution (20 ns), the required acquisition time is about 21.4 s. With an inter-satellite velocity up to 20 m/s, and with a maximum code acquisition time of 21.4 s, the satellite dynamics lead to a distance change of 428 m, exceeding the range dynamics for code tracking. Thereby, a distance range below 384 m needs to be designed, which corresponds to a maximum spacing between the early and late correlators of two code chips. A compromise between fast acquisition time and relatively high auto-correlation peak corresponds to a delay resolution of half chip, 320 ns, with an acquisition time of 1.34 s, and about 20% amplitude losses. Once the code acquisition has been accomplished, a control logic switches to code tracking. Figure 63 shows the measured discriminator function for an early minus late spacing of two chips. The slope of the discriminator function is thus equal to the absolute difference between early and late correlators, determining the delay detector characteristics. Ideally both early and late correlator presents the same amplitude level so that the discriminator function leads to an error signal with the tracking point at zero delay. Errors sources such as cross-correlation noise, shot noise and data communications produce a distortion in the amplitude and shape of the correlation function, as well as a deviation from the tracking point, which is measured and compensated by the feedback control loop.

5.2.1 Ranging accuracy: Experimental results

The dominant noise sources that limit the ranging performance are phase noise, cross-correlation noise, and dynamic stress errors. The different sources of phase noise were analyzed in chapter 3, which are induced by diverse factors including shot noise, laser

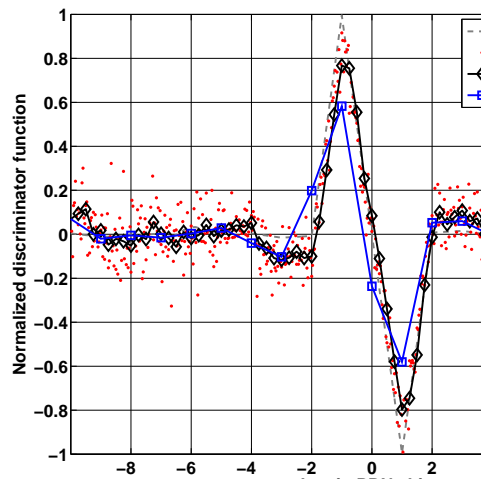


Figure 63: Normalized discriminator function measured for different delay resolution in code tracking mode.

intensity noise, and instrumental noise. The contribution of these noise sources are characterized by either SNR or C/N_0 , and the expected ranging accuracy limit was described in section 4.6.7. Cross-correlation noise is contained in the optical experiment through the presence of an additional strong ranging signal in the optical bench and the extra noise coupled by data transmission. The dynamic stress errors are determined by adding a motion function according to a relative satellite velocity larger than $\pm 20\text{m/s}$. In order to measure the ranging accuracy, this time-varying signal is subtracted from the tracked delay provided by the DLL within a measurement bandwidth between 3 and 10 Hz as expected for the on-board computer. Figure 64 shows a comparison of the corresponding rms ranging accuracy in meters for normal light ($P_M = 10\text{ nW}$) and weak-light environments. The ranging signal modulated onto the slave laser is also time-varying such that it performs a cross-correlation distribution for all possible delays. Under these conditions, experimental results demonstrate a ranging rms noise of 42 cm at 3 Hz for data rates of 24.4 kbps at 1 pW power levels.

In weak-light conditions, the raw data transmitted has a bit error rate (BER) of up to 26×10^{-3} . For data error corrections, and described in section 4.6.4, a FPGA-based Reed-Solomon (RS) encoding technique is applied to demonstrate the viability of reliable optical communications.

As shown in Table 5, RS technique provides the necessary data correction to achieve an error-free optical transmission.

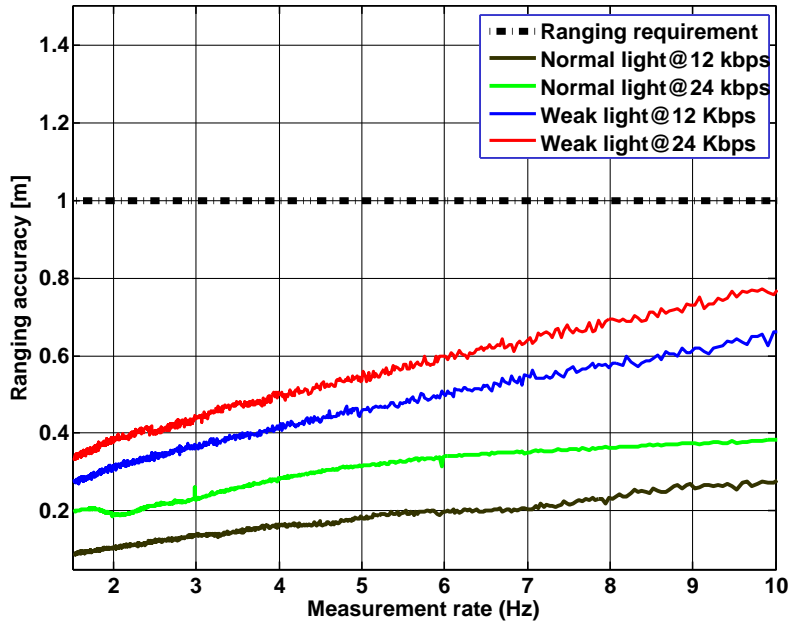


Figure 64: Measured ranging rms noise for different data rates and in the presence of LISA-like noise sources, including interference with a second PRN and signal dynamics with an equivalent inter-spacecraft larger than the expected 20 m/s.

Table 5: Ranging accuracies for different data rates and different optical power conditions.

Code parameters		Ranging rms noise		Bit Error Rate (BER)	
Optical Power	Data rate	10 Hz	3 Hz	Raw data	Reed-Solomon
10 nW	12 kbps	25 cm	15 cm	Not error detected	Not required
10 nW	24 kbps	38 cm	22 cm	Not error detected	Not required
1 pW	12 kbps	62 cm	38 cm	$< 6 \times 10^{-4}$	Not error detected
1 pW	24 kbps	76 cm	42 cm	$< 26 \times 10^{-3}$	Not error detected
Mission Requirements	Data rate	10 Hz	3 Hz	Bit Error Rate (BER)	
1 pW	11 kbps	1 m	1 m	$< 1 \times 10^{-9}$	

5.3 CLOCK SIDEBAND PERFORMANCE WITH PRN MODULATION

In a previous section 4.8.1, the clock sideband performance was electrically verified in presence of PRN modulation. Here, the clock sideband performance is optically verified to assess both:

- The phase fidelity of the clock sidebands in presence of PRN modulations.
- The driver set-up used for combining the GHz clock sidebands and PRN sequences onto the EOM.

To this end, ranging signals and clock sidebands were driven to a space-qualified version of an EOM currently under testing at the AEI (built by Northrop Grumman LITEF GmbH). The EOM leads to an efficiency of 0.7 rad/V at 2 GHz and was operated at 12 dBm to set the power in the generated sidebands to 10% of the carrier power. As shown in figure 65 (top), the EOM test experiment phase locked two lasers at 2 GHz + 1.6 kHz with one beam sent through an EOM driven by a signal at 2 GHz frequency. Both beams were heterodyned and impinged onto a photodiode. The clock sideband was combined with a ranging signal to show that neither the PRN code itself nor the combiner electronics (Mini-Circuits components: Power Combiner ZX10R-14+, DC-10 GHz; High Pass filter VHP-16, pass band 1.9-2.7 GHz; and Low Pass filter VLFX-825, pass band DC-825 MHz) interfere with the EOMs phase stability.

The phase of the 1.6 kHz sideband-carrier beat note was measured. The carrier-carrier beat note was mixed down, low-pass filtered and the phase of the resulting 1.6 kHz signals was also measured (figure 65, center). The difference of both measurements represents the noise of a single EOM sideband introduced by the EOM itself. Our measurements presented in figure 65 (bottom) show that the EOM under test complies with the LISA requirement.

5.4 FUTURE TEST PLAN: BONDED HEXAGONAL INTERFEROMETER

The LISA metrology instrument monitors picometer displacements from laser interference on the optical bench by means of phase readout at microcycle accuracy of the detected heterodyne beat note at the photoreceiver output. As shown in section 4.8, the digital phase-locked loop architecture (PLL) achieves microcycle accuracy in the mHz band. However, in optical conditions, several noise sources on the optical bench including thermal instabilities, pressure fluctuations and optical component displacements induce phase noise sensitivity at the output of the metrology system, which limits the performance of the designed metrology instrument.

Using the same technology as in LISA and LISA Pathfinder, an ultra-stable interferometer based on a hydroxy-catalysis bonding has been designed and built at the AEI

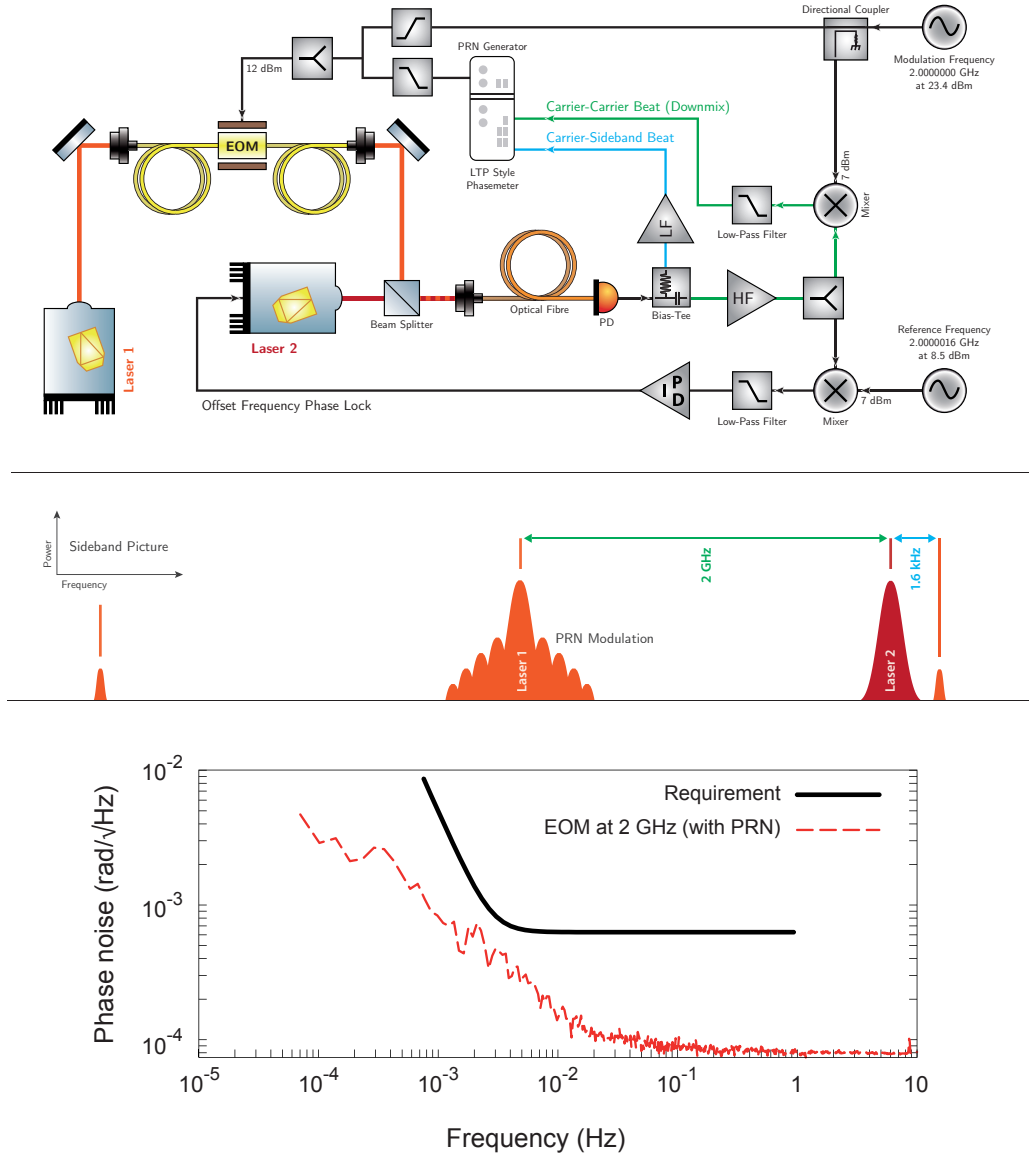


Figure 65: Top: Setup for measuring the phase fidelity of a single EOM sideband. Center: Sideband picture of the beatnotes as detected by the photodiode. Bottom: Measured phase noise of one single sideband for the EOM under test.

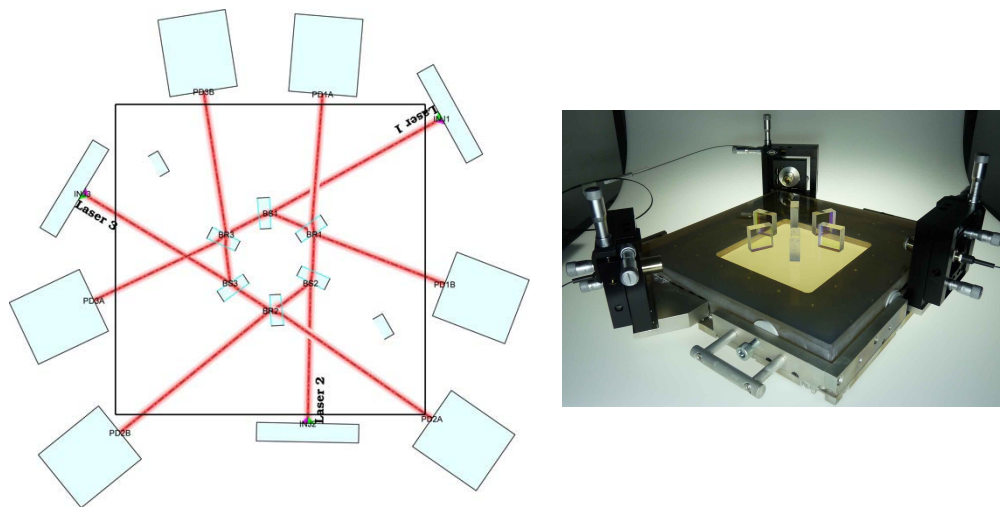


Figure 66: Left side: design of a hexagonal interferometer for optical testing in the mHz band of phasemeter performance, and TDI method using ranging and clock sidebands. Right side: photograph of current design bonded on a Zerodur baseplate.

facilities ². This bonding technique fuses together a zerodour baseplate with the optical components without using any glue or fasteners, such that it provides both a material with low-coefficient of thermal expansion and ultra-high robustness for component displacements. The optical components of the interferometer such as fiber injectors and beam splitters were precisely located, and its interferometry performance will be evaluated in vacuum conditions to reduce residual pressure and thermal fluctuations. Figure 66 shows a schematics and a photograph of the bonded interferometer. This interferometer will allow optical testing of the metrology system performance in the low-frequency (mHz) band. Thus, it will allow to gather different research threads carried out by the AEI such as data analysis technique for post-processing of raw ranging and clock noise measurements in order to converge to an optimal solution for laser frequency noise suppression using time-delay interferometry (TDI). This interferometer was designed with a hexagonal configuration to allow recombination of three separate lasers that are loosely phase locked to maintain their respective beat notes within the phasemeter (MHz) bandwidth. Common noise sources such as optical noise (intensity and frequency noise) and electronic noise at the photoreceivers are mutually canceled by linear combination of three independent phase readouts. The sum of the output signals is zero if each phasemeter has low enough noise, sufficient linearity and dynamic range, and if the synchronization, interpolation etc. all work properly. Thus, future investigations on this experiment aims to test all required functions for TDI that can be tested on ground.

² The hexagonal interferometer was designed by G. Heinzl and built by M. Dehne from the AEI institute.

5.5 SUMMARY

We have demonstrated operation of a coherent optical ranging scheme with data communication capabilities based on a laser transponder configuration. To this end, a heterodyne interferometer was built as a test bed for the PRN ranging. The experimental setup was designed to provide representative LISA-like signals, including an ultra-low light power environment equivalent to an inter-satellite distance of 5 million kilometers, and low-depth modulation scheme for its integration within a precise gravitational wave interferometer in the mHz detection band. Optical measurements presented in this chapter confirmed the analytic noise model previously presented in chapter 3, showing that the dominant system noise source results from the shot noise in weak-light conditions. Additional ranging errors due to data transfer and cross-correlation interference between the incoming and outgoing PRN sequences were electrically measured in chapter 4, and experimentally verified in an optical environment, achieving a sub-meter ranging accuracy for a signal bandwidth between 3-10 Hz.

We have also demonstrated a data encoding technique to fully reduce the bit error rate in the data transmission. This highly reliable data communication is of crucial importance since the science data measured on-board will be transmitted through the optical link. This combination of absolute ranging measurements at long distances and data communication is a key point for new architectures in deep space coherent optical transponders. Therefore, this technology development promises a significant improvement in future optical satellites, being also of great interest for other optical applications.

Throughout this thesis, it was assessed the impact of our ranging modulation scheme on the phase performance of the system and on the clock noise transfer scheme, verifying that the ranging system can be integrated without a interferometric performance degradation. This proposed ranging scheme together with advanced capabilities of the LISA metrology system provides a unique combination of precision and large ambiguity range. In contrast to other metrology systems, the presented architecture enables a set of advanced capabilities such as clock comparison of remote stations, Doppler estimations, and wavefront tilt measurements. These functionalities, together with the fact of the space applicability of the system, is not present in any other standard metrology systems.

ONGOING INVESTIGATIONS AND CONCLUSIONS

The laser ranging scheme presented in this thesis has been developed for laser frequency noise suppression via time-delay interferometry (TDI). This algorithm is applicable for interferometric gravitational wave detectors with unequal and time-varying arm-lengths. TDI combines precise laser ranging and phase measurements in order to suppress laser frequency noise by synthesizing an equal arm-length interferometer for significant sensitivity enhancement. However, the raw data received for the LISA spacecraft is not directly qualified for reconstructing the intermediate TDI variables since the three un-synchronized on-board clocks will jitter all data received. In order to form valid TDI variables, the raw data needs to be referred to a virtual common constellation clock [21, 58], which is synthesized from the ranging time stamps. An optimal filter (Kalman-like) is being investigated to allow precise data conditioning for TDI and to improve the data accuracy via integration with a dynamical model of LISA constellation [22, 82]. These ongoing investigations are being conducted in the basis of the future test plan shown in section 5.4. This optical test-bed has been designed to mimic a three arms interferometer with an unequal arm-length configuration as occurs in LISA. Each arm is formed by a single laser, and each station consists of a phasemeter reference with an independent clock. The expected results aim to demonstrate both a laser frequency noise suppression and a clock noise suppression using a TDI algorithm to achieve sensitivity at picometer level in the mHz band.

6.1 CONCLUSION OF THE THESIS

The research conducted throughout this thesis is focused on space-compatible embedded systems based on field-programmable gate array (FPGA) processing for advanced laser metrology systems. This thesis provides a detailed description of an inter-satellite metrology system. It combines a continuous-wave (c.w) laser interferometry with modulation techniques to provide in a single optical instrument both picometer-level interferometry and absolute ranging measurements with data communication capabilities. The proposed architecture allows to overcome one of the limiting factors on c.w laser interferometers, the ambiguity range. Moreover, this scheme is also used for precise timing of science data, thus enabling the inter-satellite clock synchronization by post-processing on-ground [21, 58].

In order to demonstrate functionality and the achievable performance of this development, we first modeled the system, studying the expected signal levels, the different

noise source contributions and the input signal dynamics such as the expected frequency variations due to e.g., Doppler shift. A second stage involved the hardware development of a FPGA-based prototype. We implemented the required core processing for interferometric readout, which is based on a phase-locked loop (PLL) architecture, and a delay-locked loop (DLL) architecture for absolute ranging measurements. We performed the electrical testing of the diverse laser link capabilities, validating the digital control loops and achieving the required performance. The last stage involved optical testing of the designed prototype within a representative LISA-like environment, which included the low-light power conditions and a coherent optical transponder configuration. The developed prototype is based on an optical heterodyne receiver for which the absolute range and data are extracted from a low-depth spread spectrum modulation scheme. The interferometric readout and additional capabilities such as Doppler estimations are extracted from the optical carrier itself. For such a metrology system, the most challenging developments included two key technologies. Firstly, a weak-light phase-lock loop scheme with the capability of recovering an optical carrier at microcycle accuracy ($2\pi \times 10^{-6}$ rad/ $\sqrt{\text{Hz}}$) over time scales of 1000s of seconds, corresponding to one picometer resolution in distance. Secondly, an offset phase locking method to generate a heterodyne beat signal between the incoming beam and the local laser. The heterodyne frequency in the LISA baseline is so high that independent phase measurements on different satellites cannot be read to sufficient accuracy when referenced to current space-qualified clocks. In order to overcome this challenge, a clock noise transmission scheme was implemented on the laser links and investigated in my PhD studies. Here, we achieved an equivalent clock stability of 50 fs/ $\sqrt{\text{Hz}}$ in order to provide picometer accuracy in the LISA interferometry system.

The novelties of this PhD thesis and the obtained results can be briefly described as follows:

- We have shown the first experimental demonstration of a novel concept for inter-satellite laser positioning at ultra-low light power (1 pW) levels. In this scheme, the time-of-flight of a pseudo-random noise (PRN) signal is used as a direct measure of the absolute distances between LISA satellites. Using phase-locking control, the laser link is time-stamped with precise PRN repetition epochs and the timing information extracted through cross-correlation of the incoming code sequence in a DLL architecture. This ranging concept is inherited from Global Positioning Systems (GPS), and applied to gravitational wave detectors. In contrast to other ranging methods, our development provides a low-depth modulation index to reduce both the optical power allocated to the PRN modulation and the residual carrier phase noise due to fast PRN transitions. Thus, our ranging scheme uses only 1% of the available light power and achieves sub-meter ranging accuracy over a 5 mill km inter-satellite distance while the rest of the light power is used for precise interferometry.

- We have included the first experimental demonstration of a data encoding technique to fully reduce the bit error rate in the data transmission at ultra-low light power (1 pW) levels. This improvement is of crucial importance due to the stringent requirements of operation for this scheme, being a key point for new architectures in deep-space coherent optical transponders. This capability for achieving highly reliable optical data communication, combined with the space applicability of the system, is not present in any other standard laser-based ranging systems. Therefore, it is an attractive prospect for satellite communication at long range.
- We have shown an improved data rate performance at several kilobits per second. In our architecture, the designed data rate depends on the lower heterodyne frequency (2 MHz), the PRN frequency (1.5 MHz) and the full code-length (1024 chips). Under this configuration, a standard data transfer scheme would involve several full-code length periods for a single data bit period. This configuration would limit the data rates well below 1.5 kHz (e.g. 50 bps in GPS systems). We have demonstrated that it is possible to transmit several data bit periods over a single full code-length period, increasing the data rate capabilities up to 24 kbps without a significant degradation in the correlation properties of the codes.
- We also report the operation of this ranging scheme in combination with a highly-stable heterodyne interferometer at picometer accuracy in the millihertz frequency band, providing an unique combination of precision and large ambiguity range. Thus, the proposed metrology system monitors both absolute measurements at centimeter accuracy and relative displacements at picometer accuracy. To this end, we have asserted the impact of our ranging modulation scheme on the phase performance of the system. We have included phase measurements in the mHz band to verify that both systems can be integrated without interferometric performance degradation.

The designed laser ranging scheme reaches sub-meter accuracy over equivalent distances of 5 mill km, achieving several orders of magnitude better precision for deep-space missions than currently possible with RF systems. In addition, this scheme enables data communications, which is not typical in standard laser ranging architectures. In standard telecommunication systems, the carrier does not contain information. Therefore, ranging and data communications are implemented using 100% of its power. However, for laser interferometry the carrier contains the main scientific information, such as optical pathlength fluctuations e.g. due to gravitational waves. For this reason we apply modulation schemes using a small fraction of the optical power. Furthermore, this architecture shows a great versatility and could easily be adapted to higher modulation depths, in case of an increase in the optical power available for ranging and data transfer. It would directly allow an improvement in the achievable ranging

accuracy, reducing the effect of the main limiting factor of the system, the shot noise. In a single-purpose ranging configuration, an increased frequency of the beat note would also improve the ranging accuracy. This would also provide higher bandwidth for data communication.

The designed architecture operated under the stringent requirements of the mission is unavailable in any other system, and therefore this development represents a highly innovative laser metrology system. This versatile technology is of great interest for future space missions involving formation-flying satellites, also being an attractive technology for other optical applications. Therefore, we are confident of reporting a novel development for an advanced optical metrology system of great interest for the scientific community.

Part III

APPENDIX

APPENDIX A

A.1 OPTICAL HETERODYNE DETECTION AT LOW-LIGHT POWER LEVEL

In this appendix, an analytical expression of the resulting beat note at the output of a photoreceiver for an optical heterodyne detection scheme is derived from the impinging optical fields in a beam splitter. The formulation takes into account two aspects related with the LISA metrology design

- A laser pointing misalignment caused by either satellite motion or active optical sensing of the test masses position, depending on the interferometer.
- A weak-light incoming beam caused by diffraction losses of the optical signal after propagation over the 5 million kilometer arm-length as well as additional losses on the bench.

In this analysis, two linearly polarized laser beams with parallel polarization vectors are assumed. The laser beams present slightly different wavefront angles and the recombined beam is propagating normal to the photodetector (PD) surface, being the plane of the PD represented by the vector \mathbf{r} . The optical fields of two laser beams, designated as signal $E_s(\mathbf{r}, t)$ and local oscillator $E_{LO}(\mathbf{r}, t)$, are given by

$$E_s(\mathbf{r}, t) = |E_s(\mathbf{r})| \cdot \exp(i\psi_s(\mathbf{r})) \cdot \exp(i[\omega_s t + \varphi_s]), \quad (\text{A.1})$$

$$E_{LO}(\mathbf{r}, t) = |E_{LO}(\mathbf{r})| \cdot \exp(i\psi_{LO}(\mathbf{r})) \cdot \exp(i[\omega_{LO} t + \varphi_{LO}]),$$

where $\psi_s(\mathbf{r})$ and $\psi_{LO}(\mathbf{r})$ represent the incident angles of their respective wavefronts. ω_s and ω_{LO} denote their angular frequencies ($\omega_s = 2\pi\nu_s$ and $\omega_{LO} = 2\pi\nu_{LO}$). φ_s and φ_{LO} are the optical phases of the signal and local oscillator respectively. As shown in figure 67, the two beams are recombined using a beam splitter. The interfering fields are given by

$$\begin{pmatrix} E_{\text{sym}}(\mathbf{r}, t) \\ E_{\text{asym}}(\mathbf{r}, t) \end{pmatrix} = \begin{pmatrix} i\rho & \epsilon \\ \epsilon & i\rho \end{pmatrix} \begin{pmatrix} E_s(\mathbf{r}, t) \\ E_{LO}(\mathbf{r}, t) \end{pmatrix} \quad (\text{A.2})$$

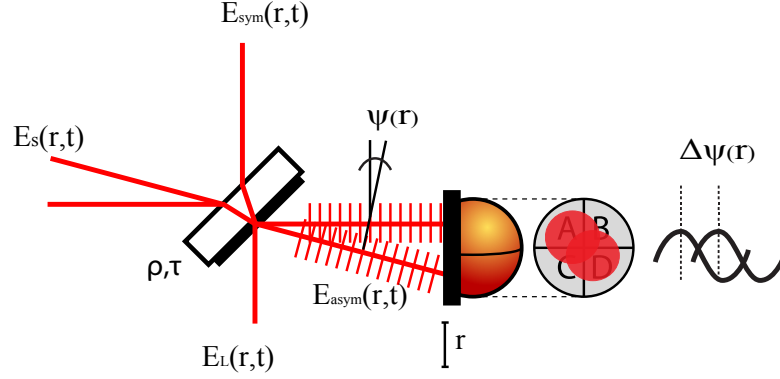


Figure 67: Heterodyne receiver of two interfering laser beams with slightly different wavefronts angles.

where $E_{\text{sym}}(t)$ and $E_{\text{asym}}(t)$ are the symmetric and asymmetric optical fields at the output of the beam splitter respectively. ϵ is the amplitude transmittance $0 < \epsilon < 1$, and ρ is the amplitude reflectivity $0 < \rho < 1$.

The optical power received $P(t)$ at the PD is proportional to the integral of the optical fields over the active surface area of the PD. Thus, the incident optical power can be written in the form

$$P(t) = \int_{\text{pd}} |E_{\text{asym}}(r, t)|^2 dA = \int_{\text{pd}} |\rho E_s(r, t) + i\epsilon E_{\text{LO}}(r, t)|^2 dA, \quad (\text{A.3})$$

and therefore can be rearranged as

$$P(t) = \underbrace{\rho^2 P_s + \epsilon^2 P_{\text{LO}}}_{\text{DC}} + \underbrace{2\rho\epsilon \int_{\text{pd}} |E_s(r)E_{\text{LO}}(r)| \cdot \cos[(\omega_{\text{het}}t + \Delta\psi(r) - \Delta\varphi)] dA}_{\text{AC}}, \quad (\text{A.4})$$

$$\text{with } P_s = \int_{\text{pd}} |E_s(r)|^2 dA, \text{ and } P_{\text{LO}} = \int_{\text{pd}} |E_{\text{LO}}(r)|^2 dA,$$

where $\omega_{\text{het}} = \omega_s - \omega_{\text{LO}}$ is the angular heterodyne frequency which corresponds to the difference between optical frequencies. $\Delta\psi(r) = \psi_s(r) - \psi_{\text{LO}}(r)$ is the phase difference between the signal and local wavefronts. $\Delta\varphi$ is the relative phase between laser beams, which is proportional to the relative optical pathlength changes ΔL

$$\Delta\varphi = \frac{2\pi\Delta L}{\lambda}, \quad (\text{A.5})$$

where λ is the average laser wavelength. The equation A.4 can be sorted by trigonometry as a function of in-phase I and quadrature Q components to:

$$P(t) = \rho^2 P_s + \epsilon^2 P_l + 2\rho\epsilon [Q \cdot \cos(\omega_{\text{het}}t - \Delta\varphi) - I \cdot \sin(\omega_{\text{het}}t - \Delta\varphi)], \quad (\text{A.6})$$

where

$$Q = \int_{\text{pd}} |E_s(r) \cdot E_{\text{LO}}(r)| \cdot \sin(\Delta\psi(r)) \, dA, \quad (\text{A.7})$$

$$I = \int_{\text{pd}} |E_s(r) \cdot E_{\text{LO}}(r)| \cdot \cos(\Delta\psi(r)) \, dA,$$

I and Q depend on the angle mismatch $\Delta\psi$ between the laser wavefronts, yielding to amplitude and phase change in the beat note

$$P(t) = \rho^2 P_s + \epsilon^2 P_{\text{LO}} + 2\rho\epsilon \sqrt{Q^2 + I^2} \cdot \cos(\omega_{\text{het}}t - \Delta\varphi - \beta(I, Q)), \quad (\text{A.8})$$

and where $\beta(I, Q)$ is a phase shift

$$\beta(I, Q) = \begin{cases} \tan^{-1}(I/Q), & \text{if } Q \geq 0 \\ \tan^{-1}(I/Q) + \pi, & \text{if } Q < 0 \end{cases} \quad (\text{A.9})$$

This equation can be rearrange as

$$P(t) = \rho^2 P_s + \epsilon^2 P_{\text{LO}} + 2\rho\epsilon \sqrt{P_s P_{\text{LO}} \gamma} \cdot \cos(\omega_{\text{het}}t - \Delta\varphi - \beta(I, Q)) \quad (\text{A.10})$$

where γ is the heterodyne efficiency, being a measure of quality for the coherent receiver. It denotes the overlapping between the received and the local beams at the photodiode.

$$\gamma = \frac{\left[\int_{\text{pd}} |E_s(r) E_{\text{LO}}^*(r)| \, dA \right]^2}{\int_{\text{pd}} |E_s(r)|^2 \, dA \int_{\text{pd}} |E_{\text{LO}}(r)|^2 \, dA} = \frac{Q^2 + I^2}{P_s P_{\text{LO}}} \quad (\text{A.11})$$

Throughout this thesis, a beam splitter with a 50:50 coating is used, unless otherwise mentioned. In this way $\rho = \epsilon = 1/\sqrt{2}$ such that equation A.10 is reduced to

$$P(t) = \frac{P_s}{2} + \frac{P_{LO}}{2} + \sqrt{P_s P_{LO}} \gamma \cdot \cos(\omega_{\text{het}} t - \underbrace{\Delta\varphi - \beta(I, Q)}_{\phi}) \quad (\text{A.12})$$

In a photoreceiver, the photocurrent is proportional to the impinging power on the photodetector according to

$$i(t) = \xi \frac{q_e \lambda}{hc} P(t) = \eta P(t) = \eta \cdot \left[\frac{P_s}{2} + \frac{P_{LO}}{2} + \sqrt{P_s P_{LO}} \gamma \cdot \cos(\omega_{\text{het}} t + \phi) \right] \quad (\text{A.13})$$

where η is the responsivity of the photodiode. ξ is the photodiode efficiency. q_e is the electronic charge (1.602×10^{-19} C). h is the Planck constant (6.626×10^{-34} J · s). c is the speed of light ($\approx 3 \times 10^8$ m/s). The maximum theoretical responsivity of a photodiode with 100% of conversion efficiency ($\epsilon = 1$) at the 1064 nm wavelength is ≈ 0.85 A/W. The quantum efficiency for a InGaAs photodiode, as used in LISA, is $\epsilon \approx 0.8$, resulting in a responsivity of typically about $\eta = 0.7$ A/W.

The optical benches of the science and test-mass interferometers are being designed to include quadrant photodetector (QPD) for angular measurements ($\Delta\psi(r)$) via Differential Wavefront Sensing (DWS). The optical power for a single quadrant segment is given by

$$I_{\text{seg}}(t) = \eta \left[\frac{P_s}{2N} + \frac{P_{LO}}{2N} + \frac{1}{N} \sqrt{P_s P_{LO}} \gamma \cdot \cos(\omega_{\text{het}} t + \phi) \right] \quad (\text{A.14})$$

with $N = 4$ segments for a QPD

APPENDIX B

B.1 CONVERSION OF PHOTOCURRENT NOISE INTO PHASE NOISE IN THE PHASEME- TER

As described in appendix A.1, the photocurrent on each segment of a QPD is proportional to the total incident optical power according to

$$I_{\text{seg}}(t) = \eta \left[\frac{P_{\text{LO}}}{2N} + \frac{P_s}{2N} + \frac{1}{N} \sqrt{P_{\text{LO}}P_s\gamma} \cdot \sin(\omega_{\text{het}}t + \phi) \right], \quad [\text{A}] \quad (\text{B.1})$$

where P_s and P_{LO} are the signal optical power and local oscillator power respectively, as shown in figure 68. η is the responsivity of the photoreceiver. γ is the heterodyne efficiency. N is the number of segments in a QPD. We now examine the noise in the phase measurement that originates from the a photocurrent noise. By using trigonometry ¹, the beat note can be written as

$$I_{\text{seg}}^{\text{AC}}(t) = \frac{\eta}{N} \sqrt{P_{\text{LO}}P_s\gamma} \cdot [\cos(\omega_{\text{het}}t) \cdot \sin \phi + \sin(\omega_{\text{het}}t) \cdot \cos \phi], \quad [\text{A}] \quad (\text{B.2})$$

For small phase changes $\phi \approx 0$, the component $\sin \phi \approx \phi$ can be approximated by the phase itself and the term $\cos \phi \approx 1$ by its normalized amplitude. By mixing the signal of equation B.2 with an electrical local oscillator ($2 \cos \hat{\omega}_{\text{het}}t$) at the same heterodyne frequency ² ($\omega_{\text{het}} - \hat{\omega}_{\text{het}} \approx 0$), and after low-pass filtering to suppress the high harmonic components, the phase of the beat note can be computed, being proportional to the beat note amplitude

$$v = \frac{\eta}{N} \sqrt{P_{\text{LO}}P_s\gamma} \cdot \phi, \quad [\text{A} \cdot \text{rad}] \quad (\text{B.3})$$

The phase error corresponding to small amplitude fluctuations can be computed as

$$\frac{\partial \phi}{\partial v} = \frac{N}{\eta \sqrt{P_{\text{LO}}P_s\gamma}}, \quad [\text{rad}/\text{A}] \quad (\text{B.4})$$

¹ Trigonometrical identity: $\sin(A + B) = \cos A \cdot \sin B + \sin A \cdot \cos B$

² Trigonometrical identity: $\cos^2(A) = \frac{1}{2} \cdot (1 + \cos 2A)$, on the other hand, $\sin A \cdot \cos A = \frac{\sin 2A}{2}$,

On the other hand, and as shown in figure 68, the phase detector output for a band-limited white noise is given by

$$\tilde{v}_{\text{seg}} = \sqrt{2} \cdot \tilde{i}_{\text{seg}}(f), \quad [\text{A}/\sqrt{\text{Hz}}] \quad (\text{B.5})$$

where $\tilde{i}_{\text{seg}}(f)$ is the single-sided linear spectral noise density (LSD) of the photocurrent. The LSD of the phase noise is then given by

$$\tilde{\vartheta}_{\text{seg}}(f) = \tilde{v}_{\text{seg}} \cdot \frac{\partial \phi}{\partial v} = \frac{\sqrt{2} \cdot \tilde{i}_{\text{seg}}(f) \cdot N}{\eta \sqrt{P_{\text{LO}} P_s} \gamma} = \frac{\tilde{i}_{\text{seg}}(f)}{I_{\text{seg,rms}}^{\text{AC}}}, \quad [\text{rad}/\sqrt{\text{Hz}}] \quad (\text{B.6})$$

with

$$I_{\text{seg,rms}}^{\text{AC}}(t) = \frac{\eta}{N} \sqrt{P_{\text{LO}} P_s} \gamma \cdot \frac{1}{\sqrt{2}}$$

where $I_{\text{seg,rms}}^{\text{AC}}$ denotes the root mean square (RMS) amplitude of the input signal. From equation B.6, one may realize that the LSD of the phase noise can be expressed in terms of the carrier to noise power density ratio (c/n_0) as follows

$$\tilde{\vartheta}_{\text{seg}}(f) = \frac{\overbrace{\tilde{i}_{\text{seg}}(f)}^{\text{LSD}}}{I_{\text{seg,rms}}^{\text{AC}}} = \frac{1}{\underbrace{\sqrt{c/n_0}}_{\text{PSD}}}, \quad [\text{rad}/\sqrt{\text{Hz}}]$$

such that c/n_0 has units of power spectral density (PSD) (B.7)

$$c/n_0 = \left(\frac{I_{\text{seg,rms}}^{\text{AC}}}{\tilde{i}_{\text{seg}}(f)} \right)^2, \quad [\text{ratio} - \text{Hz}]$$

$$C/N_0 = 10 \cdot \log_{10}(c/n_0), \quad [\text{dB} - \text{Hz}]$$

This spectral analysis is formulated as a density, and therefore the ratio between signal and noise is bandwidth-independent, i.e., normalized to a bandwidth of 1 Hz.

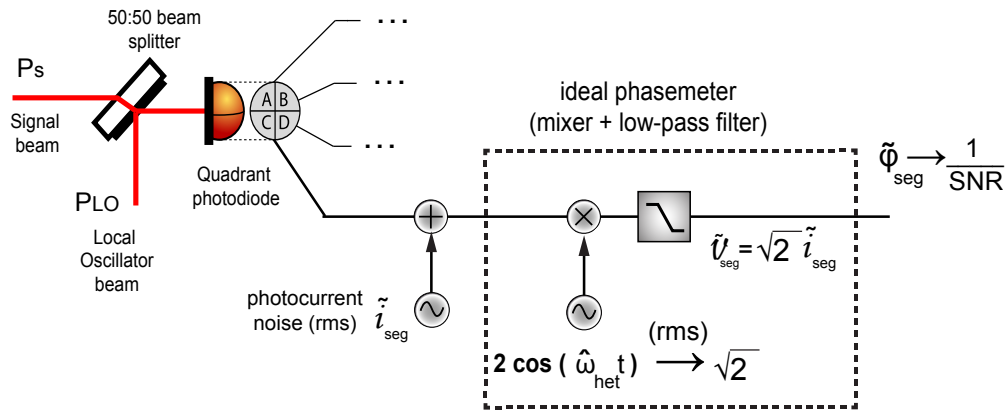


Figure 68: Schematics of the photocurrent noise model for a single segment in a quadrant photodetector.

Alternatively, this ratio can be referred to the equivalent noise bandwidth (ENBW). This way, the c/n_0 can be expressed as a function of the signal-to-noise ratio (SNR)

$$c/n_0 = \text{snr} \times \text{ENBW}, \quad [\text{ratio} - \text{Hz}]$$

$$\text{SNR} = 10 \log_{10}(\text{snr}), \quad [\text{dB}] \tag{B.8}$$

Considering the ENBW, the phase noise can be computed in terms of standard deviation with a rms value of

$$\sigma_{\text{seg}} = \frac{1}{\sqrt{\text{snr}}}, \quad [\text{rad}] \tag{B.9}$$

APPENDIX C

C.1 ELECTRONICS NOISE AND ITS CONTRIBUTIONS

A noise model of the photoreceiver is shown in figure 69. The two limiting noise sources are

- The Johnson noise \tilde{i}_{jn} in the transimpedance resistor, given by

$$\tilde{i}_{jn} = \sqrt{\frac{4k_B T}{R_f}}, \quad [\text{A}/\sqrt{\text{Hz}}] \quad (\text{C.1})$$

where k_B denotes the Boltzmann constant. T is the temperature in Kelvin. R_f is the feedback resistor of the TIA.

- The equivalent input current \tilde{i}_n and voltage \tilde{e}_n noise density contributions of the amplifier. The TIA photocurrent input noise is then given by

$$\tilde{i}_{\text{TIA}}(f) = \sqrt{\tilde{i}_n^2 + \left| \frac{1}{Z_{fb}} + \frac{1}{Z_{pd}} + \frac{1}{Z_{in}} \right|^2 \tilde{e}_n^2}, \quad [\text{A}/\sqrt{\text{Hz}}] \quad (\text{C.2})$$

where $Z_{fb} = R_f + 1/(j\omega C_f)$ denotes the feedback network impedance, $Z_{pd} = 1/(j\omega C_d)$ is the photodiode impedance model, and Z_{in} is the input impedance of the amplifier.

The total equivalent input current noise is

$$\tilde{i}_{en}(f) = \sqrt{\tilde{i}_{jn}^2 + \tilde{i}_{\text{TIA}}^2(f)}, \quad [\text{A}/\sqrt{\text{Hz}}] \quad (\text{C.3})$$

Figure 70 shows individual current noise contributions in the beat note measurement band for typical parameters of LISA-like photoreceivers. Assuming a LO optical power of 3.4 mW (nominal P_{LO} in accordance with the LISA optical bench project), and photodiode responsivity 0.7 A/W, the resulting shot noise (equation 3.3) is 9.7 pA/ $\sqrt{\text{Hz}}$ for each segment. As already mentioned, the current noise goal for the TIA must be preferably less than 2 pA/ $\sqrt{\text{Hz}}$. This implies that the quadratic sum of the current noise of individual segments is 4 pA/ $\sqrt{\text{Hz}}$.

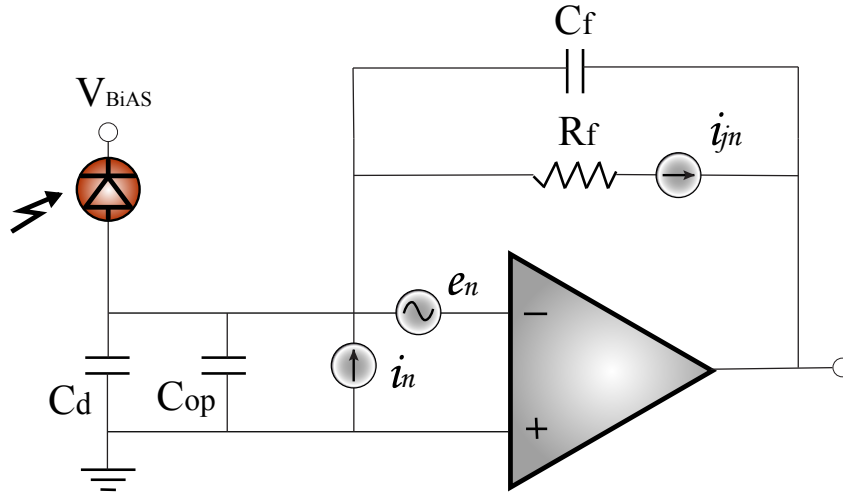


Figure 69: Noise model of the photoreceiver.

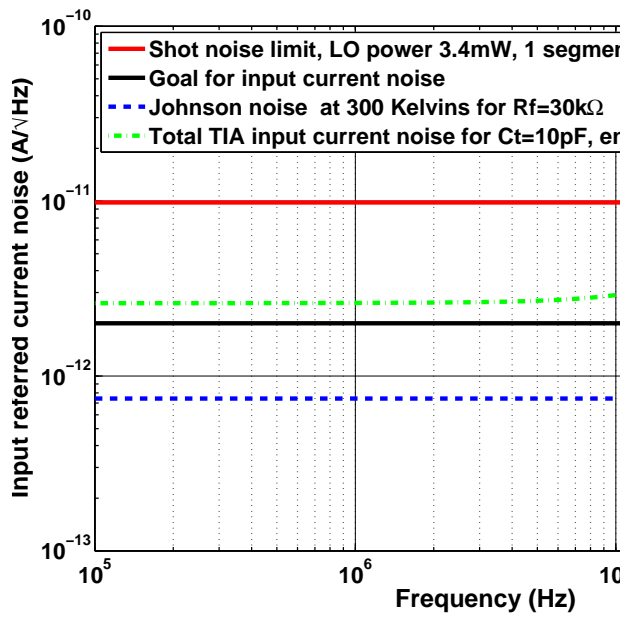


Figure 70: Estimated input current noise for a typical LISA-like photoreceiver using an LMH6624 op-amp in a standard circuit.

A TIA model for the actual photoreceiver parameters is shown in the dashed curve and the following parameters were assumed: a total circuit capacitance of $C_T = 10$ pF, being dominated by the photodiode capacitance C_d and a op-amp common-mode input capacitance C_f , an input impedance of 1 M Ω , a TIA resistance of 30 k Ω , an amplifier voltage noise of 4 nV/Hz, and an op-amp current noise of 2.5 pA/Hz. The model shows an increasing voltage noise contribution at high frequencies due to the capacitance. Thus the challenge for the photodiode design is the development of a low-capacitance per segment while maintaining a high responsivity. Besides, the design of the TIA electronic requires a low-noise op-amp (e.g. LMH6624) within the beat note frequency range. The bandwidth of the photoreceiver is given by

$$BW_{pr} \approx \sqrt{\frac{GBW}{2\pi R_f C_T}}, \quad [\text{Hz}] \quad (\text{C.4})$$

where GBW is the gain bandwidth product of the op-amp [83], typically of a few GHz. Thus, R_f and C_T also impact in the expected photoreceiver bandwidth, being designed to provide a bandwidth of about 30 MHz. An alternative design is investigated at AEI [69] which uses discrete npn RF transistors instead on an op-amp and has shown promising results so far.

APPENDIX D

D.1 QUANTIFICATION NOISE

An analog-to-digital converter (ADC) maps a continuous-time, continuous-amplitude signal to a sequences of discrete values with a resolution of B bits at a sampling rate of f_{sampl} . The digital value $x[n]$ of an analog signal $x(t)$ is given by a finite bit-length numbers from 0 to 2^B . Each quantization step q represents a fraction of 2^B of the full analog input range V_{max} of the ADC [63]. This defines the quantization step of the a digitized signal

$$V_{\text{LSB}} = q = \frac{V_{\text{max}}}{2^B} \quad [\text{V}] , \quad (\text{D.1})$$

Assuming an uniform probability distribution at the output of the quantizer given by

$$f_n(e) = \begin{cases} \frac{1}{q}, & -\frac{q}{2} < e < \frac{q}{2} \\ 0 & \text{elsewhere,} \end{cases} \quad (\text{D.2})$$

the power of the quantization noise equals the square of its variance σ_e^2 such that

$$\sigma_e^2 = E\{e^2\} = \frac{1}{q} \int_{-q/2}^{q/2} f_n^2(e) de = \frac{q^2}{12} \quad [\text{V}^2], \quad (\text{D.3})$$

In order to compute the power spectral density of the quantification noise, the Shannon's criterion is taking into account. Assuming an input signal limited to the frequency interval between 0 to $f_{\text{sampl}}/2$, the spectral density of the quantification noise power is

$$|\tilde{V}_{\text{adc}}(f)|^2 = \frac{\sigma_e^2}{\frac{f_{\text{sampl}}}{2}} \quad [\text{V}^2/\text{Hz}], \quad (\text{D.4})$$

and consequently for the linear spectral density of the quantization noise

$$\tilde{V}_{\text{adc}}(f) = \frac{V_{\text{max}}}{2^B \sqrt{6 \cdot f_{\text{sampl}}}} \quad [\text{V}/\sqrt{\text{Hz}}], \quad (\text{D.5})$$

APPENDIX E

E.1 ELECTRONICS

The next pages contain the schematic electronic circuits of the devices that were used in the optical experiment.

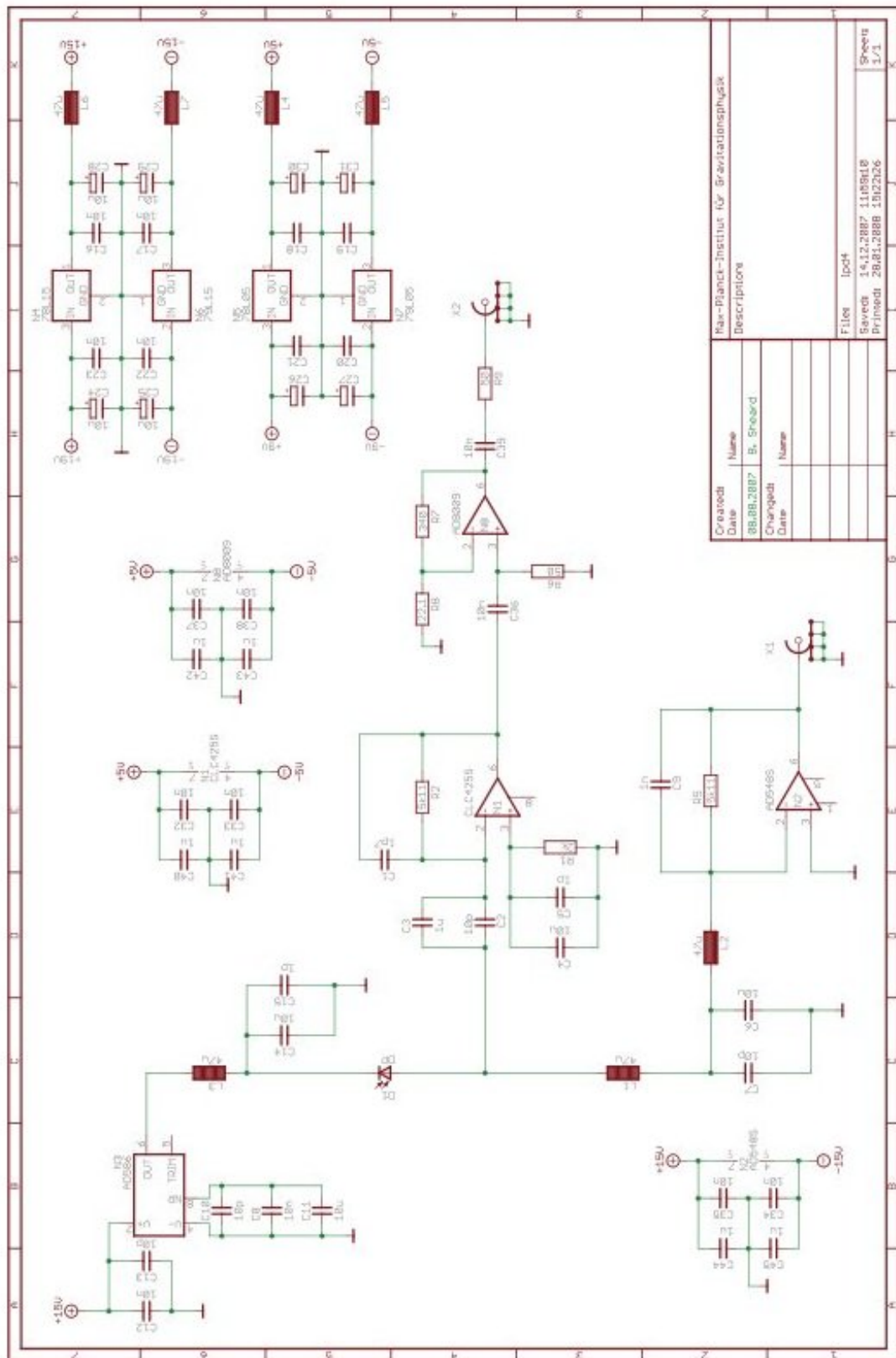


Figure 71: Photodetector circuit.

APPENDIX F

F.1 FPGA PROGRAMMING USING MATLAB®

This appendix aims to help new users for programming an Actel FPGA using a Matlab/Simulink® environment. Actel® [84] provides a toolset for FPGA prototyping called Libero® Integrated Design Environment (IDE) [85]. In addition the vendor provides another software package called Symphony® Model Compiler AE [86] for high level FPGA programming, which installs a set of Simulink blockset into Matlab [87]. A Simulink model generated with Symphony can be integrated with an existing VHDL Libero project. To explain the process, a low-pass Filter is designed in a Matlab environment and imported as an entity into a VHDL template. For this example, a VHDL template only defines the input and output of the front-end electronic of digital breadboard described in section 4.7. In this example, the Simulink program takes the digital signal sampled from an input register at 16 bit resolution, and after its filtering the resulting signal is transmitted to one of the available DAC output channels.

The generation of hybrid code (high level Simulink code and low-level VHDL code) is useful since

- Speed-up FPGA development and enables easy code simulation.

A graphical environment enables a comprehensive design and analysis of the actual design. In addition, Matlab provides a wide range of functions and blocks that can be very useful for stimulus generation and code analysis.

- It enables FPGA programming for users without experience in VHDL languages

This feasibility of integration allows that a group of templates can be used to place Matlab entities. A VHDL template can provide the functionality of specific hardware embedded into our current breadboard. For example, data readout through the parallel port, built-in ADC/DAC ports or additional block previously programmed. To this end, an inexperienced user can use the FPGA breadboard for other purposes without deep knowledge of physical breadboard routing (pin allocation) or VHDL language.

- Working with useful tools already provided with Matlab

Symphony Model implements a set of blockset which are quite complex to implement using pure VHDL code. For example, CORDIC algorithms which can process the imaginary and the real part to obtain the phase and the magnitude of a signal.

F.2 REQUIRED SOFTWARE

The main processor unit of the digital breadboard is an Actel FPGA (ProAsic3E A3PE3000 or ProAsic3E A3PE1500). Libero IDE can program all Actel FPGAs, and the software can be downloaded from the Actel's website with one year free-license. On the other hand Synphony Model requires the installation of Matlab/Simulink.

After Synphony Model installation, a set of additional toolboxes are added to the Simulink library browser. The blocksets generate valid and debugged code for the FPGA. To run this program correctly extra toolboxes in Matlab are required.

- Communications Blockset.
- Communications Toolbox.
- Filter Design HDL Coder.
- Filter Design Toolbox.
- Fixed-Point Toolbox.
- Signal Processing Blockset.
- Signal Processing Toolbox.
- Simulink Fixed Point.
- Simulink HDL Coder.
- EDA Simulator Link MQ.

Figure 75 shows a diagram of design flow. After model design, Simulink creates an encrypted RTL code that can be processed by Synphony Model. In order to translate from the encrypted RTL to EDN netlist, Synplify PRO [88] compiles the RTL code. The EDN netlist is converted to VHDL code using a command `edn2vhdl` in the Matlab prompt. The VHDL code generate can be imported into Libero IDE project manage and the definition of the entity given in the Matlab can be used as interface by simply adding a call function between the entity and the root project.

F.3 HIGH-LEVEL PROGRAM DESCRIPTION

This section describes the design of a digital FIR filter using Matlab environment. The I/O selected for the model reads 16 bit with 1 MHz sampling rate. The Filter is a Low pass FIR filter with cutoff frequency at 50 kHz and 80 dB rejection in stop-band.

F.3.1 *Matlab/Simulink/Synplify DSP*

Figure 76 shows the Simulink model designed and the current plots obtained in the simulation. The input of the design is the sum of two different sines at different frequencies (Sine_lFreq, Sine_hFreq). Only the blockset available in Synphony Model can produce valid RTL code and therefore loaded to the FPGA. For this model the valid blockset are: input port (`x_data`), the FIR block, and the output port (`y_data`). Here, additional Simulink blocksets from any Matlab library can be used in the design, however these blocks will not be programmed in the FPGA.

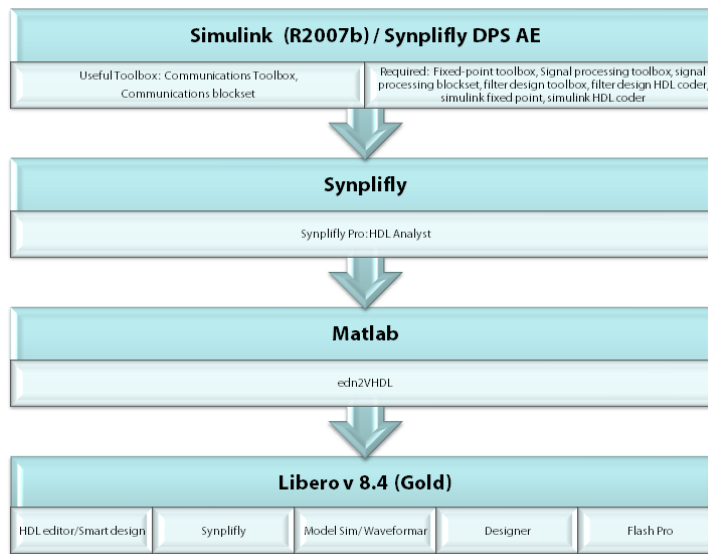


Figure 75: Flow diagram for programming the digital breadboard.

Nevertheless, they generate data vectors that can be imported as stimulus or RTL test bench into a Libero project. To stimulate the FIR filter and study the behavior of our design in Matlab, two sines at different frequencies provide the input of the filter. Scopes from the signal processing blockset are employed to view intermediate datapath points in the time domain and in the frequency domain.

The data format for the model is Fixed-point (FPGA can not process in floating point precision), and therefore quantification noise will affect the signal datapath. To determine the quantification noise introduced in the model, the “SynFixPtTool tool” is used. It allows an estimation of quantification noise due to the fixed precision given in the model. For this example we run the design with enough bit resolution to enable acceptable filtering rejection.

The I/O ports (x_data , y_data) define the boundaries of the design that will be loaded in the FPGA. The input port is intentionally downsampled from 1 MHz to 50 kHz, this reduces the timing requirements for the filtering. The selected parameters are:

I/O Port

- x_data input port:

Word length: 16 bit resolution without fractional part

Data type: signed

Sample time: $\frac{1}{1\text{MHz}}$ s

- y_ data output port:

Word length: 16 bit resolution without fractional part

Data type: signed

Sample time: $\frac{1}{1\text{MHz}}$ s

Input signal

- Sine_lFreq: Low frequency sine.

Amplitude 2^9

Frequency $2\pi \frac{1\text{MHz}}{2} 0.05$ rad/s $\rightarrow f = 25$ kHz

Phase 0 (rad)

Bias 0

- Sine_hFreq: High frequency sine

Amplitude 2^9

Frequency $2\pi \frac{1\text{MHz}}{2} 0.95$ rad/s $\rightarrow f = 475$ kHz

Phase 0 (rad)

Bias 0

For filtering design, the blocks FDATool and FIR are used. Figure 77 shows some relevant parameters and the magnitude shape of the filter designed. The frequency is normalized to $f_s/2 = 500$ kHz. The frequency specification are selected such as the pass-band corresponds with the 10% of the normalized frequency, so the cutoff frequency is $(1\text{MHz}/2) \cdot 0.1 = 50$ kHz. The magnitude in the pass-band is hardly flat around 1 dB. The stop-band is fixed at 80% of the normalized frequency and with a filter roll-off below 80 dB rejection. The design obtained is a stable filter of 51 coefficients computed by means of an equiripple method. The FIR blockset is selected such as the datapath enables low quantification noise (16 bits resolution in fractional part to compute the coefficients). The output word length is a 16 bit resolution without fractional part and with a signed data format.

To translate the Simulink model to an encrypted RTL model, a double-click in the FIR_DSP block will launch the Synphony tool, as shown in figure 78. In the implementation window the FPGA target is selected. Additionally, it is possible to generate a testbench or automatic generation in the RTL code of an asynchronous global reset implementation. The RTL resulting is created in a folder called FIR_matlab_impl_1. In this folder is present the project to be loaded in the Synphony in order to convert the RTL code to EDN netlist block.

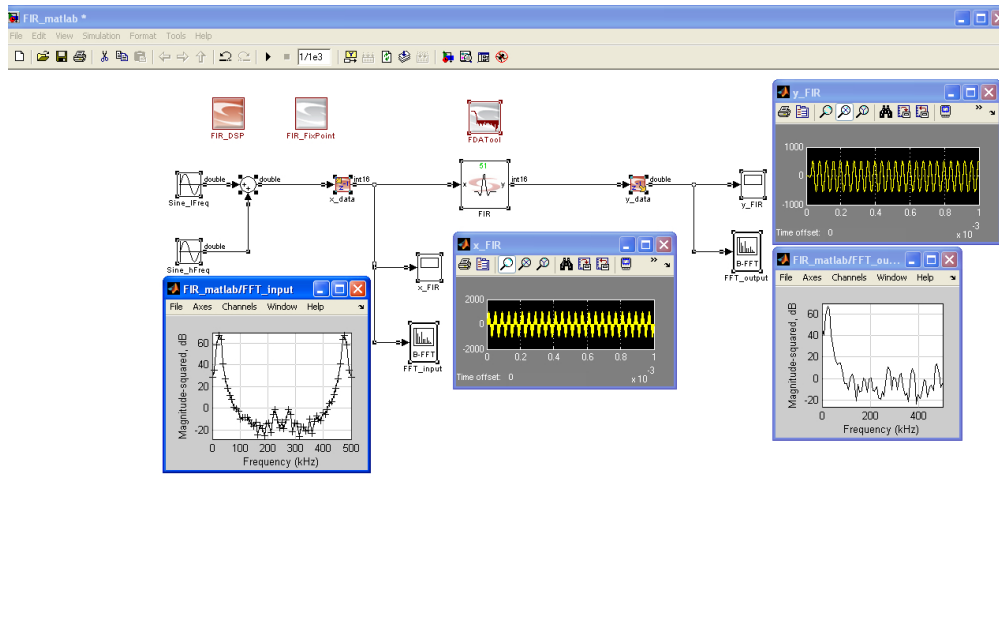


Figure 76: Simulink model with a sampling rate of 1 MHz. It simulates a low-pass FIR filter of 51 coefficient, cutoff frequency at 50 kHz, filter roll-off at 80 dB and a sinusoidal input composed for two sines at different frequencies (25 kHz and 475 kHz).

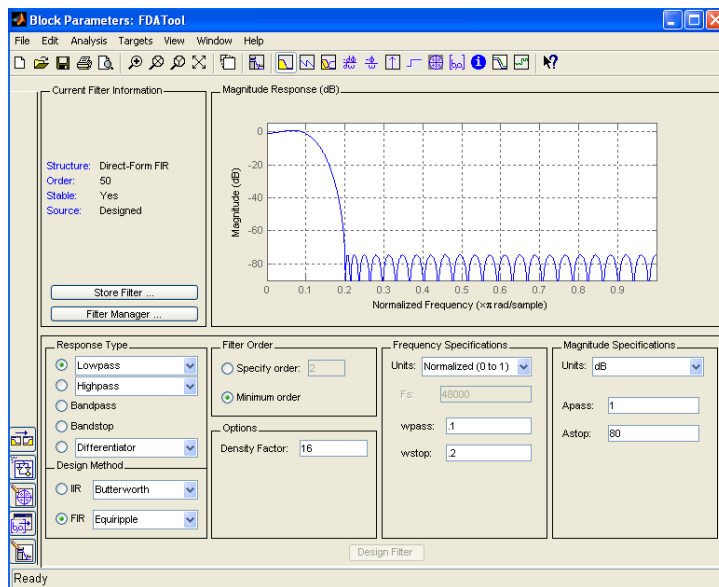


Figure 77: Parameters for the designed filter with minimum order and equiripple method. The magnitude response is normalized at $1 = f_s/2 = 500$ kHz

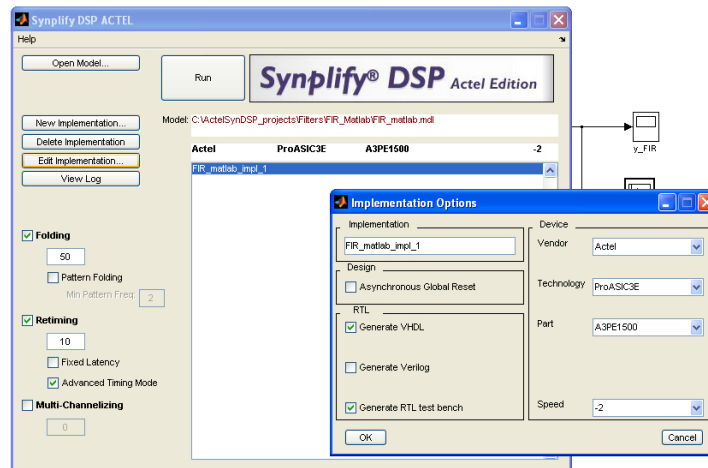


Figure 78: Synplify DSP converter from Simulink model to RTL code.

F.3.2 Synplify PRO

The encrypted RTL is not recognized by Libero IDE. It is required to run Synplify PRO outside Libero IDE to read the encrypted RTL and then generates an EDN netlist block.

The RTL generated by Synphony is encrypted in the sense that the software's vendor not allow to access to the VHDL code generated. In order to view your resulting design, Synplify PRO provides a tool called HDL Analyst which is only available with Synplify PRO version. After compiling the RTL code, the debugging of the design is possible. Synplify PRO enables additional tools for this purpose, allowing the study of datapaths and the navigation inside the HDL blocks until system gate level.

The implementation results are placed in the folder named "rev_1" in the current directory. The EDN netlist block is then converted to an HDL code block using the follow command in the Matlab prompt:

```
!edn2vhd FAM:ProASIC3E EDNIN:FIR_matlab.edn VHDOUT:FIR_matlab.vhd FIR_matlab
```

F.4 LOW-LEVEL PROGRAM DESCRIPTION

This section describes the Libero IDE environment in order to create hybrid projects.

1. The used Libero IDE VHDL template is:

```
library ieee;
use ieee.std_logic_1164.all;
```

– definition of I/O and signal clocks

```
entity Template is
port( ADC3_DCO : in std_logic;
DAC_clk, ADC3_DFS: out std_logic;
ADC3_DATA : in std_logic_vector(15 downto 0);
DAC1_DATA : out std_logic_vector(13 downto 0)
);
```

```
end Template;
```

– Component definition

```
architecture bhv of Template is
```

– Buffer

```
component B
port(PAD : in std_logic; Y : out std_logic) ;
end component;
```

– Register 16 bit

```
component Reg16
port( Data : in std_logic_vector(15 downto 0);Clock : in
std_logic; Q : out std_logic_vector(15 downto 0)) ;
end component;
```

– Additional variables used to components interconnection

```
signal ADC3_DCOX : std_logic;
```

```
signal DAC3_DATAX : std_logic_vector (15 downto 0);
```

```
begin
```

– clock setting

```
bufo : B
port map (PAD => ADC3_DCO, Y => ADC3_DCOX);
```

```
DAC_clk <= ADC3_DCOX;
```

– ADC setting

```
ADC3_DFS <= '1';
```

– Register 16 bit ADC

```
reg_ADC : Reg16
```

```
port map( Data => ADC3_DATA, Clock => ADC3_DCOX, Q => DAC3_DATAX);
```

```
DAC1_DATA <= DAC3_DATAX(15 downto 2);
```

```
end bhv;
```

2. Placing the VHDL source generated with Matlab into the current Libero Template project
Import or copy the content of the VHDL source generated with Matlab placed in the directory `FIR_matlab_impl_1/vhdl/rev_1/FIR_matlab.vhd` into the Libero project.
3. Connecting the entity

The Matlab VHDL source code has an entity with the same name “FIR_matlab” of your Simulink model. This entity can be copied and is the interface of the Matlab code. Matlab always generate a clock input, Global Enable, GlobalReset as well as the I/O ports defined in the model. For our implementation only two I/O have been used (`x_data` and `y_data`).

```
entity FIR_matlab is
```

```
port( clk : in std_logic;  
GlobalReset: in std_logic;  
x_data : in std_logic_vector(15 downto 0);  
y_data : out std_logic_vector(15 downto 0);  
GlobalEnable1 : in std_logic  
);
```

```
end FIR_matlab;
```

4. The entity must be copied in the VHDL source code of the template and assign the desired signal to this entity.

The Template yield as follow:

– Template.vhd

```
library ieee;
use ieee.std_logic_1164.all;

library proasic3e;
use proasic3e.all;

entity Template is

port( ADC3_DCO : in std_logic;
      ADC2_DCO : in std_logic;
      Rst : in std_logic;
      Enb : in std_logic;
      DAC_clk, ADC3_DFS: out std_logic;
      ADC3_DATA : in std_logic_vector(15 downto 0);
      DAC1_DATA : out std_logic_vector(13 downto 0)

);

end Template;

architecture bhv of Template is

-- definition buffer

component Buf is

port(PAD : in std_logic; Y : out std_logic) ;

end component ;

-- definition filter with Matlab

component FIR_matlab is

port( clk : in std_logic;
      GlobalReset : in std_logic;
      x_data : in std_logic_vector(15 downto 0);
      y_data : out std_logic_vector(15 downto 0);
      GlobalEnable1 : in std_logic);

end component;
```



```

signal DAC3_DATAX : std_logic_vector (15 downto 0);
signal DAC3_clk : std_logic;

```

```

begin

```

```

-- ADC setting

```

```

ADC3_DFS <= '1';

```

```

Buf1 : Buf

```

```

port map (PAD => ADC3_DCO, Y => DAC3_clk);

```

```

-- Filer with matlab

```

```

Fir51coef : FIR_matlab

```

```

port map ( clk => ADC2_DCO, GlobalReset => Rst , x_data => ADC3_DATA, y_data =>
DAC3_DATAX, GlobalEnable1 => Enb);

```

```

DAC_clk <= DAC3_clk;

```

```

DAC1_DATA <= DAC3_DATAX(15 downto 2);

```

```

end bhv;

```

5. After the integration of both codes, the process to finally program the FPGA is as usual

In order to test the correct behavior of the designed Filter, the program has been loaded in the PMS 2 and the transfer function measures with a Spectrum Analyzer.

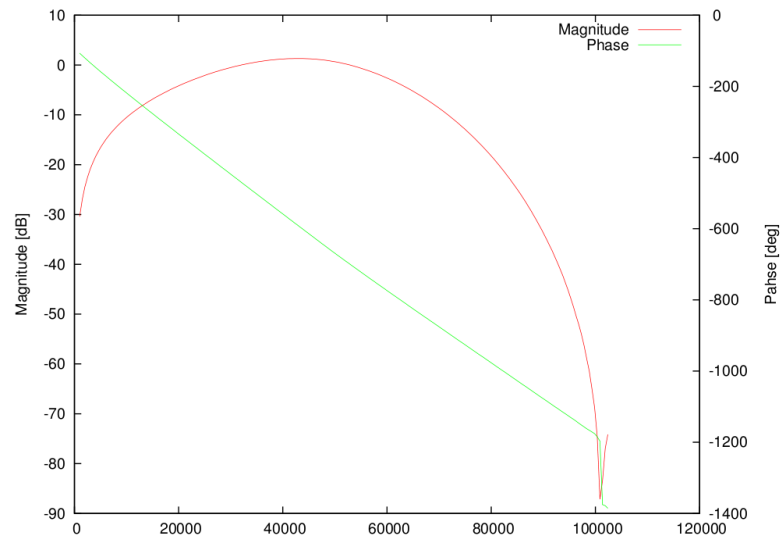


Figure 79: Transfer function of the filter designed.

F.5 CODE TESTING

The Picture 79 shows the resulting transfer function between two channel of PMS 2. To achieve this measurement an low frequency range Spectrum Analyzed has been used. The output signal of the Spectrum Analyzer is set as swept sine from 1 kHz to 120 kHz frequency range. A swept sine is generated and fed into the PMS 2 using one of the ADC input channel. As output channel a DAC has been connected to the Spectrum Analyzer.

The functionality of the filter has been verified. The transfer function show a increasing gain at low frequencies. It is caused due to the breadboard has implemented two additional filters, before and after the ADC conversion and DAC output respectively.

BIBLIOGRAPHY

- [1] R. E. Slusher.
Laser technology.
Reviews of Modern Physics, 71(2), 1999.
(Cited on page 1.)
- [2] Seung-Woo Kim.
Metrology: Combs rule.
Nature Photonics, (3):313–314, 2009.
(Cited on pages 1 and 12.)
- [3] I. Coddington, W. C. Swann, L. Nenadovic, and N. R. Newbury.
Rapid and precise absolute distance measurements at long range.
Nature Photonics, (3):351–356, 2009.
(Cited on pages 1 and 12.)
- [4] T. E. Bell.
Gravitational astronomy: Hearing the heavens.
Nature News, (452):18–21, 2008.
(Cited on pages 1 and 10.)
- [5] Robert Irion.
LIGO’s mission of gravity.
Science, 228(5465):420–423, 2000.
(Cited on page 1.)
- [6] Robert Irion.
LIGO’s laser-packing big sister LISA may hunt black holes from space.
Science, 288(5465):422, 2000.
(Cited on page 1.)
- [7] The LIGO Scientific Collaboration.
A gravitational wave observatory operating beyond the quantum shot-noise limit.
Nature Physics, (doi:10.1038/nphys2083):published on-line, 2011.
(Cited on page 1.)
- [8] J. O. Dickey et al.
Lunar laser ranging: A continuing legacy of the apollo program.
Science, 22(5171):482–490, 1994.
(Cited on page 2.)
- [9] James G. Williams, Slava G. Turyshev, and Dale H. Boggs.
Progress in lunar laser ranging tests of relativistic gravity.
Phys. Rev. Lett., 93(261101), 2004.
(Cited on page 2.)

- [10] Stephen M. Merkowitz.
Tests of gravity using lunar laser ranging.
Living Rev. Relativity, 13, 2010.
(Cited on page 2.)
- [11] John F. Cavanaugh et al.
The Mercury Laser Altimeter Instrument for the MESSENGER mission.
Space Science Reviews, 131(1-4):451–479.
(Cited on page 3.)
- [12] Renny Fields et al.
NFIRE-to-TerraSAR-X laser communication results: satellite pointing, disturbances and other attributes consistent with successful performance.
Proceedings of SPIE, the International Society for Optical Engineering, 2009.
(Cited on page 3.)
- [13] John R. Barry and Edward A. Lee.
Performance of coherent optical receivers.
Proc. IEEE, 78(8), 1990.
(Cited on pages 3, 12, and 80.)
- [14] D. Adam.
Gravity measurement: Amazing grace.
Nature, 416(6876):10–11, 2002.
(Cited on page 8.)
- [15] B.S. Sathyaprakash and Bernard F. Schutz.
Physics, astrophysics and cosmology with gravitational waves.
Living Rev. Relativity, 12(2), 2009.
(Cited on page 10.)
- [16] Matthew Pitkin, Stuart Reid, Sheila Rowan, and Jim Hough.
Gravitational wave detection by interferometry (ground and space).
Living Rev. Relativity, 14(5), 2011.
(Cited on page 10.)
- [17] LISA International Science Team (LIST).
LISA assessment study report: Yellow Book.
European Space Agency (ESA), 2011.
(Cited on pages 10, 17, 25, 30, 53, and 55.)
- [18] *Laser Interferometer Space Antenna: Sciencecraft Description*.
LISA-SC-DD-0001. NASA Goddard Space Flight Center, 2009.
(Cited on page 10.)
- [19] Eugenie Samuel Reich.
Europe makes do without NASA.
Nature, 471, 2011.
(Cited on page 11.)

- [20] Massimo T, Shaddock D, Sylvestre J, and Armstrong J.
Implementation of time-delay interferometry for LISA.
Phys. Rev. D, (67), 2003.
(Cited on pages 11 and 54.)
- [21] Glenn de Vine and Brent Ware et al.
Experimental demonstration of time-delay interferometry for LISA.
Phys. Rev. Letters, (104), 2010.
(Cited on pages 11, 54, 56, and 111.)
- [22] Heinzl G, Esteban J.J, Barke S, Otto M, Wang Y, Garcia Marin A.F, and Danzmann K.
Auxiliary functions of the LISA laser link: ranging, clock noise transfer and data communication.
Class. Quantum Grav, 28(9), 2011.
(Cited on pages 12, 13, 17, 58, and 111.)
- [23] Esteban J.J, Garcia A.F, Barke S, Peinado A.M, Guzman F, Bykov I, Heinzl G, and Danzmann K.
Experimental demonstration of weak-light laser ranging and data communication for LISA.
Opt Express, 19(17):15937–15946, 2011.
(Cited on pages 12 and 17.)
- [24] Andrew Sutton, Kirk McKenzie, Brent Ware, and Daniel Saddock.
Laser ranging and communication for LISA.
Opt Express, 18(20):20759, 2010.
(Cited on pages 12 and 17.)
- [25] Website of the LISA International Science Community (LISC).
<http://www.lisa-science.org/>.
(Cited on page 17.)
- [26] Website of the EADS Astrium.
<http://www.astrium.eads.net/>.
(Cited on page 17.)
- [27] LISA International Science Team (LIST).
Laser Interferometer Space Antenna for the Detection and Observation of Gravitational Waves: Pre-Phase A Report.
Max-Planck-Institute for Quantum Optics, 1996.
(Cited on page 17.)
- [28] LISA International Science Team (LIST).
Laser Interferometer Space Antenna for the Detection and Observation of Gravitational Waves: Pre-Phase A Report.
Max-Planck-Institute for Quantum Optics, 1998.
(Cited on page 17.)
- [29] LISA International Science Team (LIST).
System and Technology Study Report.

- European Space Agency (ESA), 2000.
(Cited on page 17.)
- [30] LISA International Science Team (LIST).
LISA assessment study report: Yellow Book.
European Space Agency (ESA).
To be published.
(Cited on page 17.)
- [31] Heinzl G.
Ranging with pseudo-random noise.
LISA International Science Team (LIST) meeting, 2002.
(Cited on pages 17 and 76.)
- [32] Tröbs M. et al.
Fiber modulators and fiber amplifiers for LISA.
J. Phys.: Conf. Series.
(Cited on page 17.)
- [33] Barke S, Troebs M, Sheard B, Heinzl G, and Danzmann K.
EOM sideband phase characteristics for the spaceborne gravitational wave detector LISA.
Appl Phys B, (98), 2010.
(Cited on pages 17 and 98.)
- [34] Jennrich O.
LISA technology and instrumentation.
Class. Quantum Grav, (26):153001, 2009.
(Cited on page 20.)
- [35] Fleddermann R. et al.
Measurement of the non-reciprocal phase noise of a polarization maintaining single-mode optical fiber.
J. Phys.: Conf. Series, (154), 2009.
(Cited on page 21.)
- [36] Optical bench development for LISA.
2008.
LISA-EST-SW-691.
(Cited on page 21.)
- [37] LISA metrology system.
2010.
LISA-EST-SOW-848.
(Cited on pages 22 and 66.)
- [38] E. Morrison, B. J. Meers, D. I. Robertson, and H. Ward.
Automatic alignment of optical interferometers.
Appl. Opt, 33(22):5041–5049, 1994.
(Cited on pages 26 and 70.)

- [39] E. Morrison, B. J. Meers, D. I. Robertson, and H. Ward.
Experimental demonstration of an automatic alignment system for optical interferometers and automatic alignment of optical interferometers.
Appl. Opt., 33(22):55037–5040, 1994.
(Cited on pages 26 and 70.)
- [40] Peter L Bender.
Wavefront distortion and beam pointing for LISA.
Class. Quantum Grav., 22(S339-S346), 2005.
(Cited on page 26.)
- [41] Fichter W, Gath P, Vitale S, and Bortoluzzi D.
LISA pathfinder drag-free control and system implications.
Class. Quantum Grav., 22(10,S139), 2005.
(Cited on page 26.)
- [42] Heinzl G, Braxmaier C, Caldwell M, and Danzmann K et al.
Successful testing of the LISA Technology Package (LTP) interferometer engineering model.
Class. Quantum Grav., 22(S149-S154), 2005.
(Cited on page 26.)
- [43] Frank Steier.
Interferometry techniques for spaceborne gravitational wave detectors.
Ph.D Thesis presented in Max-Planck-Institut fuer Gravitationsphysik und Leibniz Universitaet Hannover, 2008.
(Cited on page 28.)
- [44] B.J. Meers and K.A. Strain.
Modulation, signal and quantum noise in interferometers.
Phys. Rev. A.
(Cited on page 28.)
- [45] T.M. Niebauer, R. Schilling, K. Danzmann, A. RÄajdiger, and W. Winkler.
Nonstationary shot noise and its effect on the sensitivity of interferometers.
Phys. Rev. A.
(Cited on page 28.)
- [46] Website of Innolight GmbH.
<http://www.innolight.de/>.
(Cited on page 29.)
- [47] Optical bench design, opto-electronics and alternative beam compressors.
LOB-AEI-TN-008.1-08,2011.
(Cited on page 30.)
- [48] B.S Sheard, M.B Gray, D.A Shaddock, and D.E McClelland.
Laser frequency noise suppression by arm-locking in lisa: progress towards a bench-top demonstration.
Class. Quantum Grav., (22):S221–S226, 2005.
(Cited on page 35.)

- [49] Garcia Marín A.F et al.
Phase locking to a LISA arm: first results on a hardware model.
Class. Quantum Grav, (22):235–242, 2005.
(Cited on page 35.)
- [50] LISA frequency control study team.
ESA Report No. LISA-JPL-TN-823, 2009.
(Cited on pages 35, 53, and 54.)
- [51] Gerhard Heinzel.
Advanced optical techniques for laser-interferometric gravitational-wave detectors.
Ph.D Thesis presented in Max-Planck-Institut fuer Gravitationsphysik und Leibniz Univer-
sitaet Hannover, 1999.
(Cited on page 48.)
- [52] Ronald W. Hellings.
Elimination of clock jitter noise in spaceborne laser interferometers.
Phys. Rev. D, (64):0222002, 2001.
(Cited on page 54.)
- [53] William Klipstein, Peter G. Halverson, Robert Peters, Rachel Cruz, and Daniel Shaddock.
Clock noise removal in lisa.
AIP Conf Proc, (873):312–318, 2006.
(Cited on page 54.)
- [54] Shaddock D, Ware B, Halverson P, Spero R, and Vallisneri M.
Postprocessed time-delay interferometry for LISA.
Phys Rev D, (70), 2004.
(Cited on page 54.)
- [55] Tinto M, Estabrook F B, and Armstrong J W.
Time-delay interferometry for space-based gravitational wave searches.
Astrophys. Journal, (527):814 – 826, 1999.
(Cited on page 54.)
- [56] Heinzel G, Braxmaier C, Danzmann K, Gath P, and Hough J et al.
LISA interferometry: recent developments.
Class. Quantum Grav., 23, 2006.
(Cited on page 55.)
- [57] McNamara P.W.
Weak-light phase locking for LISA.
Class. Quantum Grav, (22):243–247, 2005.
(Cited on pages 55 and 68.)
- [58] Daniel A. Shaddock, Brent Ware, Robert E. Spero, and M Vallisneri.
Postprocessed time-delay interferometry for LISA.
Phys. Rev. D, (70(8)):081101, 2004.
(Cited on pages 58, 95, and 111.)

- [59] Misra P and Enge P.
Global positioning system, signals, measurements, and performance.
(Cited on page 58.)
- [60] Golomb, W. Solomon, and G. Guang.
Signal design for good correlation : for wireless communication, cryptography, and radar.
2005.
(Cited on pages 59 and 60.)
- [61] B. W. Parkinson and J.J Spilker.
Global positioning system: theory and applications.
1996.
(Cited on pages 59 and 84.)
- [62] G.Heinzel.
Private communication.
(Cited on page 60.)
- [63] Vinzend Wand.
Interferometry at low frequencies: Optical phase measurement for LISA and LISA pathfinder.
Ph.D Thesis presented in Max-Planck-Institut fuer Gravitationsphysik und Leibniz Universitaet Hannover, 2007.
(Cited on pages 66 and 129.)
- [64] Bykov I, Esteban J.J, Garcia Marin A.F, Heinzel G, and Danzmann K.
LISA phasemeter development: Advanced prototyping.
J. Phys.: Conf. Series, (154), 2009.
(Cited on page 66.)
- [65] Esteban J.J, Garcia Marin A.F, Johannes Eichholz, Antonio M. Peinado, Bykov I, Heinzel G, and Danzmann K.
Ranging and phase measurement for LISA.
J. Phys: Conf. Series, (228), 2010.
(Cited on page 66.)
- [66] Marcin M.R.
Digital receiver phase meter for LISA.
IEEE Trans. Instrum. Meas, 54(6), 2005.
(Cited on page 66.)
- [67] Ware B, Folkner W, and Shaddock D et al.
Phase measurement system for inter-spacecraft laser metrology.
Earth Science Technology Conference, 2006.
(Cited on page 66.)
- [68] Cruz J. R et al.
The LISA benchtop simulator at the University of Florida.
Class. Quantum Grav, (23):S751–S760, 2006.
(Cited on page 66.)

- [69] Diekmann C, Steier F, Sheard B, G.Heinzel, and Danzmann.
Analog phase lock between two lasers at LISA power levels.
J. Phys.: Conf. Series, (154), 2009.
(Cited on pages 68 and 127.)
- [70] G. J. Dick, Meirong Tu, D. Streakalov, K. Birnbaum, and Nan Yu.
Optimal phase lock at femtowatt power levels for coherent optical deep-space transponder.
IPN. progress report., (45):175, 2008.
(Cited on page 68.)
- [71] A. Torosyan and A.N Willson.
Exact analysis of dds spurs and snr due to phase truncation and arbitrary phase-to-amplitude errors.
Proceedings of the 2005 IEEE International Frequency control Symposium, 2005.
(Cited on page 71.)
- [72] H.T. Nicholas and H. Samueli.
An analysis of the output spectrum of direct digital frequency synthesizers in the presence of phase-accumulator truncation.
41st Annual Symposium on Frequency Control, 1987.
(Cited on page 71.)
- [73] D. Shaddock R. Spero P. Halverson I. Harris T. Rogstad B. Ware, W.M. Folkner.
Phase measurement system for inter-spacecraft laser metrology.
Earth science technology conference, 2006.
(Cited on page 71.)
- [74] R. E. Blahut.
Theory and Practice of Error-Control Codes.
1983.
(Cited on page 80.)
- [75] E.R.Berlekamp.
Algebraic Coding Theory.
1984.
(Cited on page 80.)
- [76] Chang Xiaojun, Guo Jun, and Li Zhihui.
RS encoder design based on FPGA.
2nd International conference on advanced computer control, 2010.
(Cited on page 80.)
- [77] Liu Tong and Zhang Chuan.
Optimization design of Reed-Solomon decoder based on FPGA.
International conference on Electronics, Communications and Control, 2011.
(Cited on page 80.)
- [78] Website of Jenoptik.
<http://www.jenoptik.com>.
(Cited on page 98.)

- [79] Simon Barke.
Inter-Spacecraft Clock Transfer Phase Stability for LISA.
Diploma Thesis presented in Max-Planck-Institut fuer Gravitationsphysik und Leibniz
Universitaet Hannover, 2008.
(Cited on page 98.)
- [80] Patrick Kwee.
Laser characterization and stabilization for precision interferometry.
Ph.D Thesis presented in Max-Planck-Institut fuer Gravitationsphysik und Leibniz Univer-
sitaet Hannover, 2010.
(Cited on page 100.)
- [81] P. Kwee and B. Willke.
Automatic laser beam characterization of monolithic Nd:YAG nonplanar ring lasers.
Appl. Opt., 47(32):6022–6032, 2008.
(Cited on page 100.)
- [82] Yan Wang, Gerhard Heinzel, and Karsten Danzmann.
Bridging the gap between the phasemeter raw data and TDI.
J. Phys: Conf. Series, To be published.
(Cited on page 111.)
- [83] Felipe Guzman et al.
Characterization of photoreceivers for LISA.
Class. Quantum Grav, 28, 2011.
(Cited on page 127.)
- [84] Website of Actel.
<http://www.actel.com/>.
(Cited on page 137.)
- [85] To download Libero IDE.
<http://www.actel.com/download/software/liberoide/>.
(Cited on page 137.)
- [86] To download Symphony Model Compiler AE.
<http://www.actel.com/download/software/dsp/>.
(Cited on page 137.)
- [87] Website of Matlab.
<http://www.mathworks.de>.
(Cited on page 137.)
- [88] To download Synplify Pro.
<http://www.actel.com/download/software/synplify/>.
(Cited on page 138.)

ACKNOWLEDGMENTS

I am deeply grateful to Prof. Dr. Karsten Danzmann for his continuous support and for the chance to contribute to such exciting project, LISA.

I am also deeply grateful to Prof. Dr. Antonio M. Peinado Herreros for his support and guidance during the past years. Thank you very much.

I am owing greatly to PD Dr. Gerhard Heinzl. This PhD. thesis is a result of his great ideas, his expertise and his assistance. Thank you for believing in me and for introducing me to a broad range of subjects including interferometry and laser ranging. It had been, and is a privilege to work with you in such an exciting science projects as carried out by the AEI. Thank you again for your support, guidance and friendship.

Special thanks go to my colleagues and supervisors Dr. Antonio F. Garcia, Dr. Felipe Guzman and Dr. Miquel Nofrarias who greatly contributed to this work. Thank you for your patient explanations, suggestions and corrections during all these years.

I want to express my gratitude to Dr. Oliver Jennrich, Dr. Allan Hornstrup, Dr. Søren Møller and Dr. Alberto Lobo for their essential support in this doctoral thesis, despite of their incredibly tight agendas.

Thank you Dr. Jeffrey Livas and Dr. Ira Thorpe for the short but fruitful stay at NASA Goddard Space Center.

I am indebted to Heather Audley, Gerhard, Felipe, Antonio and Markus Otto for proof-reading this thesis and making it much easier to read.

I thank my colleagues and friends of the Interferometry in Space Group at the AEI. In particular, Simon Barke, Oliver Geberding, Ingo Diepholz, Benjamin Sheard, Johanna Bogenstahl, Joachin Kullmann, Iouri Bykov, Yan Wang, Michael Tröbs, Marina Dehne, Christoph Mahrtdt, Vitali Müller and Philip Peterson.

Thanks to all (ex)members of the institute Johannes Eichholz, Frank Steier, Vinzenz Wand and Anneke Monsky for a friendly atmosphere, their contributions in this work and making fruitful discussions.

Thank you to my family, who has always shown me the correct path, supported and loved me. Thank you to my great love, my wife.

JUAN JOSÉ ESTEBAN DELGADO

PERSONAL INFORMATION

Born on January 18th, 1979 in Cádiz, Spain.
Nationality Spain.
Email juan.jose.esteban@aei.mpg.de

EDUCATION

Present **Ph.D. candidate as electro-optical engineer,**
Max-Planck Institute for Gravitational Physics, Hannover, Germany.
Area of study: Inter-satellite laser ranging and data communications.

Apr 2009 **M.Sc., Advanced Studies in Computer Techniques,**
Graduated with Distinction, University of Almeria, Spain.
Area of study: Codes and cryptography, real-time signal processing and control systems.

Jul 2006 **M.Sc., Telecommunication Engineering,**
European University of Madrid, Spain.
Master Thesis: Development of an audio encoder for real-time systems in digital signal processors. Master Thesis graded with Honours.
Area of study: Computer science, optics, electronics and telecommunication systems.

FELLOWSHIPS & AWARDS

Nov 2006 **Research grant,** Radio modem development for telemetry and
Oct 2007 telecontrol applications. Dept of Computer Architecture and Electronics,
University of Almeria, Spain.
Description: Electronic development of a radio-communication system for kilometer distance transmission.

Aug 2005 **Research grant,** Telemetry system for monitoring of environmental
Oct 2005 conditions in caves. Dept of Computer Architecture and Electronics, Uni-
versity of Almeria, Spain.
Description: Remote sensing, networking and telemetry to measure temperature, barometric pressure, carbon dioxide concentration, humidity and wind in hostile environments.

PUBLICATIONS

- **Esteban J.J, et al;** *Experimental demonstration of weak-light laser ranging and data communication for LISA*, *Optics Express*, Vol. 19, Issue 17, pp. 15937-15946 **2011**.
- **Heinzel G, Esteban J.J, et al;** *Auxiliary functions of the LISA laser link: ranging, clock noise transfer and data communication*, *Class. Quantum Grav*, 28 094008 **2011**.
- **Esteban J.J, et al;** *Optical ranging and data communication in space-based applications*, 7th Workshop on Positioning, Navigation and Communication, *IEEE Conf Proc*,(19-22), 978-1-4244-7158-4, **2010**.
- **Esteban J.J, et al;** *Ranging and phase measurement for LISA* 8th Edoardo Amaldi Conference on Gravitational Waves, *J. Phys.: Conf. Series*, (228) 012045, **2010**.
- **LISA frequency control study team;** *LISA frequency control white paper*, *ESA document LISA-JPL-TN-823*, **2009**.
- **Esteban J.J, et al;** *Free-space laser ranging and data communication* 6th Workshop on Positioning, Navigation and Communication, *IEEE Conf Proc*, 275-281, **2009**.
- **Esteban J.J, et al;** *Optical ranging and data transfer development for LISA*, 7th International LISA Symposium, *J. Phys.: Conf. Series*, (154) 012025, **2009**.
- **Bykov I, Esteban J.J, et al;** *LISA phasemeter development: Advanced prototyping*, 7th International LISA Symposium, *J. Phys.: Conf. Series*, (154) 012017, **2009**.

CONFERENCES

- Experimental demonstration of laser ranging and data communication at picowatt power levels for the LISA mission, 8th International LISA Symposium. Jun 28-Jul 2 2010, Stanford University, California (USA).
- Optical ranging and data communication in space-based applications, COSPAR 38th Scientific Assembly, 18-25 Jul 2010 Bremen (Germany).
- Optical ranging and data communication in space-based applications, 7th IEEE Workshop on Positioning, Navigation and Communication (WPNC'10), 11-12 Mar 2010 Dresden (Germany).
- LISA Phasemeter Development: ADC jitter correction, Deutsche Physikalische Gesellschaft, 8-12 Mar 2010 Hannover (Germany).
- Inter-spacecraft laser ranging and data communication for LISA, Deutsche Physikalische Gesellschaft, 8-12 Mar 2010 Hannover (Germany).
- Free-space laser ranging and data communication, 6th IEEE Workshop on Positioning, Navigation and Communication (WPNC'09), 19 Mar 2009 Hannover (Germany).
- Ranging and phase measurement for LISA, 8th Edoardo Amaldi Conference on Gravitational Waves, 21-26 Jun 2009 Columbia University, New York (USA).
- LISA onboard ranging and data communication capabilities, Deutsche Physikalische Gesellschaft, 9-13 Mar 2009 Munich (Germany).
- Optical ranging and data communication for LISA, Deutsche Physikalische Gesellschaft, 2-6 Mar 2009 Hamburg (Germany).
- Laser ranging and data communication in space-based applications, Deutsche Physikalische Gesellschaft, 2-6 Mar 2009 Hamburg (Germany).
- LISA Phasemeter Development: Digital Phase-Lock Loop (DPLL) analysis, Deutsche Physikalische Gesellschaft, 9-13 Mar 2009 Munich (Germany).
- Laser modulation for ranging and data communication In space-based applications, Second workshop Optische Technologien, 17 Nov 2008 Hannover (Germany).
- Optical ranging and data transfer development for LISA, 7th International LISA Symposium, 16-20 Jun 2008 Barcelona (Spain).
- LISA phasemeter development:Advanced prototyping, 7th International LISA Symposium, 16-20 Jun 2008 Barcelona (Spain).
- Interspacecraft laser ranging for LISA, Deutsche Physikalische Gesellschaft, 10-14 Mar 2008 Darmstadt (Germany).

- LISA: Laser interferometry for the spaceborne gravitational wave detection, Deutsche Physikalische Gesellschaft, 10-14 Mar 2008. Darmstadt (Germany).
- Sistemas de monitorización médica mediante sensores biomédicos e integración en redes inalámbricas heterogéneas, INFORSALUD 2007 6-8 Mar 2007 Madrid (Spain).
- PACS en Unidades de Endoscopia Digestiva, Jornadas Murciana, 7-9 Sept 2007 Murcia (Spain).